

**LIGHT ASSISTED COLLISIONS OF COLD ATOMS  
IN AN OPTICAL DIPOLE TRAP**

**NITHIWADEE THAICHAROEN**

**MASTER OF SCIENCE  
IN PHYSICS**

**THE GRADUATE SCHOOL**

**CHIANG MAI UNIVERSITY**

**MAY 2012**

**LIGHT ASSISTED COLLISIONS OF COLD ATOMS  
IN AN OPTICAL DIPOLE TRAP**

**NITHIWADEE THAICHAROEN**

**A THESIS SUBMITTED TO THE GRADUATE SCHOOL IN  
PARTIAL FULFILLMENT OF THE REQUIREMENTS  
FOR THE DEGREE OF  
MASTER OF SCIENCE  
IN PHYSICS**

**THE GRADUATE SCHOOL  
CHIANG MAI UNIVERSITY**

**MAY 2012**

**LIGHT ASSISTED COLLISIONS OF COLD ATOMS  
IN AN OPTICAL DIPOLE TRAP**

NITHIWADEE THAICHAROEN

THIS THESIS HAS BEEN APPROVED  
TO BE A PARTIAL FULFILLMENT OF THE REQUIREMENTS  
FOR THE DEGREE OF MASTER OF SCIENCE  
IN PHYSICS

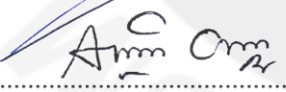
**EXAMINING COMMITTEE**

 CHAIRPERSON

Assoc. Prof. Dr. Somsorn Singkarat

 MEMBER

Asst. Prof. Sarayut Deachapunya

 MEMBER

Dr. Waranont Anukool

**THESIS ADVISOR**



Dr. Waranont Anukool

23 May 2012

© Copyright by Chiang Mai University

## ACKNOWLEDGEMENT

I would like to express my sincere gratitude to all those who gave me the possibility to complete this thesis.

In the first place I am gratefully acknowledge my supervisor Dr. Waranont Anukool for the supervision, encouragement, and stimulating suggestions all the time of research. He gave me his precious time sharing his experience and guidance to work in the future. His ways of thinking exceptionally inspire me.

I would like to record my gratitude to Prof. Dr. Thirapat Wilaithong for his continuous support and personal guidance as well as giving me extraordinary experiences. His truly scientist intuition enriches my growth as a researcher want to be.

I appreciatively acknowledge Assoc. Prof. Dr. Somsorn Singkarat for his strong will to support this research both in man power and infrastructures. I have furthermore to thank Assoc. Prof. Dr. Prayoon Songsiriritthigul for his kindness in supporting us a vacuum chamber and suggestions about the vacuum system. I would like to thank Asst. Prof. Sarayut Deachapunya in his suggestions for this research.

I convey special acknowledgement to Dr. Narupon Chattrapiban for his collaborations and invaluable supports. I learned from him a great deal of necessary skills and knowledge. Without him this work would not be possible.

I was extraordinarily fortunate in having T. Sriarunothai for supporting me in every possible ways. Moreover, I truly appreciate the warm atmosphere in the

Quantum-atom Optics Laboratory (QAO) from P. Sompet, A. Chayakul, C. Kamrapis, P. Chaiwongkot, T. Poomaradee, R. Kaewuam, and T. Staporn.

I would like to thank T. Chulapakorn, A. Wijaikham, and P. Thopan for giving me such a pleasant time when studying together. I also want to thank them for their support and valuable suggestions.

I wish to extend my warmest thanks to all those who have helped me in the Plasma and Beam Physics Research Facility (PBP) and department of Physics and Materials Science at Chiang Mai University. My special thanks also go to funding agencies including DPST, JSTP, and ThEP. I also would like to thank everybody who was important to the successful realization of this research, as well as expressing my apology that I could not mention personally one by one.

Finally, it is a pleasure to express my gratitude wholeheartedly to my mother, father, and grandmother, whose patient love enabled me to complete this work.

Nithiwadee Thaicharoen

<b>Thesis Title</b>	Light Assisted Collisions of Cold Atoms in an Optical Dipole Trap
<b>Author</b>	Ms. Nithiwadee Thaicharoen
<b>Degree</b>	Master of Science (Physics)
<b>Thesis Advisor</b>	Dr. Waranont Anukool

### ABSTRACT

The main purposes of this research are theoretical studies of light-assisted-collision (LAC) processes in cold neutral atoms and its experimental implementations in Rubidium-85 atoms. The studies were given to identify minimum number of processes necessary for a simplification of the LAC experiments. The highlight was based on the combination of the following: (1) the simplified magneto-optical trap, (2) the optical dipole trap and (3) the LAC lasers. The magneto-optical trap was constructed from four- beam configurations to overcome the spatial restriction of the optical alignment. The dipole trap was a far-red detuned laser focused to  $h \times 10.95$  MHz deep and  $4.7 \mu\text{m}$  wide to trap a small number of atoms and to increase coherence time. Lastly, the LAC lasers were tuned near the D1 line of Rubidium-85. All constituents mean to control two body cold collision and provide access to fluorescence imaging. The detail of the constructions was provided together with the discussion on accessibility and practicality of the experiment.

ชื่อเรื่องวิทยานิพนธ์	การชนแบบแสงช่วยของอะตอมเย็นในกับดักไดโพลเชิงทัศนศาสตร์
ผู้เขียน	นางสาวนิธิดา ไทยเจริญ
ปริญญา	วิทยาศาสตรมหาบัณฑิต (ฟิสิกส์)
อาจารย์ที่ปรึกษาวิทยานิพนธ์	ดร.วรานนท์ อนุกุล

### บทคัดย่อ

เป้าหมายหลักของงานวิจัยนี้คือการศึกษาทฤษฎีของการชนแบบแสงช่วยของอะตอมเย็นที่เป็นกลางทางไฟฟ้าและการทดลองที่เกี่ยวข้องสำหรับอะตอมรูบิเดียม-85 โดยในการศึกษานี้ต้องการระบุจำนวนขั้นตอนที่น้อยที่สุดและการทำการทดลองการชนแบบแสงช่วยให้ง่ายขึ้น ในส่วนของ การทดลองนั้นสิ่งที่สำคัญประกอบไปด้วย (1) กับดักแม่เหล็กเชิงทัศนศาสตร์ที่ง่ายขึ้น (2) กับดักไดโพลเชิงทัศนศาสตร์ และ (3) เลเซอร์เพื่อใช้ในการชนแบบแสงช่วย โดยกับดักแม่เหล็กเชิงทัศนศาสตร์ได้ถูกสร้างขึ้นโดยอาศัยการออกแบบแบบสี่ลำแสงเพื่อเอาชนะข้อจำกัดด้านการจัดตำแหน่งแสง สำหรับกับดักไดโพลนั้นสร้างมาจากเลเซอร์ซึ่งไกลก้ำทอนในทางสีแดงและถูกโฟกัสให้กับดักมีความลึก  $h \times 10.95$  เมกะเฮิร์ตซ์และความกว้าง 4.7 ไมครอนเพื่อกักอะตอมจำนวนน้อยๆ และเพิ่มเวลาพร้อมเพรียง ในท้ายที่สุด เลเซอร์เพื่อใช้ในการชนแบบแสงช่วยถูกปรับไปยังตำแหน่งใกล้เส้น D1 ของรูบิเดียม-85 สิ่งที่สร้างขึ้นทั้งหมดนี้เพื่อควบคุมการชนเย็นระหว่างสองอนุภาคและการเข้าถึงสภาพวาวแสง รายละเอียดของสิ่งที่สร้างขึ้นทั้งหมดได้ถูกนำเสนอพร้อมกับการวิจารณ์ถึงความสามารถเข้าถึงได้และการปฏิบัติการทดลอง

**TABLE OF CONTENTS**

	Page
<b>ACKNOWLEDGEMENT</b>	<b>iii</b>
<b>ABSTRACT ENGLISH</b>	<b>v</b>
<b>ABSTRACT THAI</b>	<b>vi</b>
<b>TABLE OF CONTENTS</b>	<b>vii</b>
<b>LIST OF TABLES</b>	<b>x</b>
<b>LIST OF FIGURES</b>	<b>xi</b>
<b>ABBREVIATIONS AND SYMBOLS</b>	<b>xv</b>
<b>CHAPTER 1 INTRODUCTION</b>	<b>1</b>
1.1 Motivation	1
1.2 Thesis Outline	2
<b>CHAPTER 2 THEORETICAL BACKGROUND</b>	<b>4</b>
2.1 Introduction	4
2.2 Laser Cooling and Trapping	4
2.3 Magneto-optical Trap	7
2.4 Optical Dipole Trap	11
2.5 Light Assisted Collisions between Cold Atoms	17

2.6 Imaging	19
<b>CHAPTER 3 EXPERIMENTAL SETUP AND INSTRUMENTATION</b>	<b>21</b>
3.1 Introduction	21
3.2 Lasers	21
3.3 Vacuum System	27
3.4 Magnetic Coils	34
3.5 Optical Alignment	36
3.6 Imaging System	40
<b>CHAPTER 4 RESULTS AND DISCUSSIONS</b>	<b>43</b>
4.1 Introduction	43
4.2 Magneto-optical Trap	43
4.3 Optical Dipole Trap	52
4.4 Light Assisted Collisions	55
<b>CHAPTER 5 CONCLUSIONS AND FUTURE PLANS</b>	<b>59</b>
5.1 Conclusions	59
5.2 Future Plan	60
<b>REFERENCES</b>	<b>61</b>
<b>APPENDICES</b>	<b>64</b>
<b>APPENDIX A RUBIDIUM-85 DATA</b>	<b>65</b>
A.1 Introduction	65

A.2 Rubidium-85 Energy Level	65
<b>APPENDIX B CIRCUIT DIAGRAM</b>	<b>69</b>
B.1 Introduction	69
B.2 Laser Driver	70
B.3 Temperature Controller	73
B.4 Triangular Wave Generator	76
B.5 Servolock	78
B.6 Fast Shutter Driver	81
<b>APPENDIX C MECHANICAL DRAWING</b>	<b>83</b>
C.1 Laser Base Plate and Laser Box	83
C.2 Vacuum Chamber	89
C.3 High NA Lens Mount	97
C.4 MOT Lens Mount	100
<b>APPENDIX D CALCULATION AND PROGRAMMING</b>	<b>102</b>
D.1 Background Subtraction Program (MATLAB)	102
D.2 Magnetic Field Gradient (MATLAB)	103
D.3 Magnetic Field along Z Axis (MATLAB)	104
D.4 Approximate Magnetic Field Line (MATHEMATICA)	105
<b>CURRICULUM VITAE</b>	<b>106</b>

## LIST OF TABLES

Table	Page
3.1 Details of components used to construct the ECDL.	23
3.2 Details of vacuum apparatuses used in this experiment.	31
4.1 The measured variables for the trap depth calculation of $^{85}\text{Rb}$ .	53
A.1 Fundamental physical constants.	66
A.2 $^{85}\text{Rb}$ physical properties.	66
A.3 $^{85}\text{Rb}$ D2( $5^2\text{S}_{1/2} \rightarrow 5^2\text{P}_{3/2}$ ) transition optical properties.	66
A.4 $^{85}\text{Rb}$ D1( $5^2\text{S}_{1/2} \rightarrow 5^2\text{P}_{1/2}$ ) transition optical properties.	66
A.5 $^{85}\text{Rb}$ reduced matrix elements.	67
A.6 $^{85}\text{Rb}$ dipole matrix elements for the D2 $\pi$ transitions ( $F=3, m_F \rightarrow F', m'_F = m_F$ ) expressed as multiples of $\langle J=1/2 \  \mathbf{d} \  J'=3/2 \rangle$ .	67
A.7 $^{85}\text{Rb}$ dipole matrix elements for the D2 $\pi$ transitions ( $F=2, m_F \rightarrow F', m'_F = m_F$ ) expressed as multiples of $\langle J=1/2 \  \mathbf{d} \  J'=3/2 \rangle$ .	67
A.8 $^{85}\text{Rb}$ dipole matrix elements for the D1 $\pi$ transitions ( $F=3, m_F \rightarrow F', m'_F = m_F$ ) expressed as multiples of $\langle J=1/2 \  \mathbf{d} \  J'=1/2 \rangle$ .	68
A.9 $^{85}\text{Rb}$ dipole matrix elements for the D1 $\pi$ transitions ( $F=2, m_F \rightarrow F', m'_F = m_F$ ) expressed as multiples of $\langle J=1/2 \  \mathbf{d} \  J'=1/2 \rangle$ .	68

## LIST OF FIGURES

Figure	Page
2.1 A stationary atom obtains the energy and momentum transfer from a photon.	5
2.2 Absorption and emission processes of a moving atom.	6
2.3 Schematic diagram of the magneto optical trap.	7
2.4 Shows hyperfine excitation of atoms in one dimension MOT.	8
2.5 Optical alignment for the four-beam MOT.	10
2.6 The schematic of an optical dipole trap [11].	11
2.7 Direction of the dipole force constructed by red-detuned laser beam.	13
2.8 Dressed-atom energy diagram.	15
2.9 The separation of energy between each manifold when a Gaussian laser beam is applied to an atom. Reproduced from ref. [12].	16
2.10 The results of collisions between two atoms in the ground state.	17
2.11 The schematic of electronic energy levels of Rubidium atoms.	18
2.12 The schematic of electronic energy levels of Rubidium atoms.	19
3.1 ECDL in the Littrow configuration.	22
3.2 The schematic diagram of the optical alignment.	25
3.3 Schematic diagram of (a) the collisions and probe laser (b) the LAC repumping laser.	27
3.4 Schematic of the science chamber used for cooling and trapping Rb atoms.	28
3.5 Rubidium dispenser assembly.	29

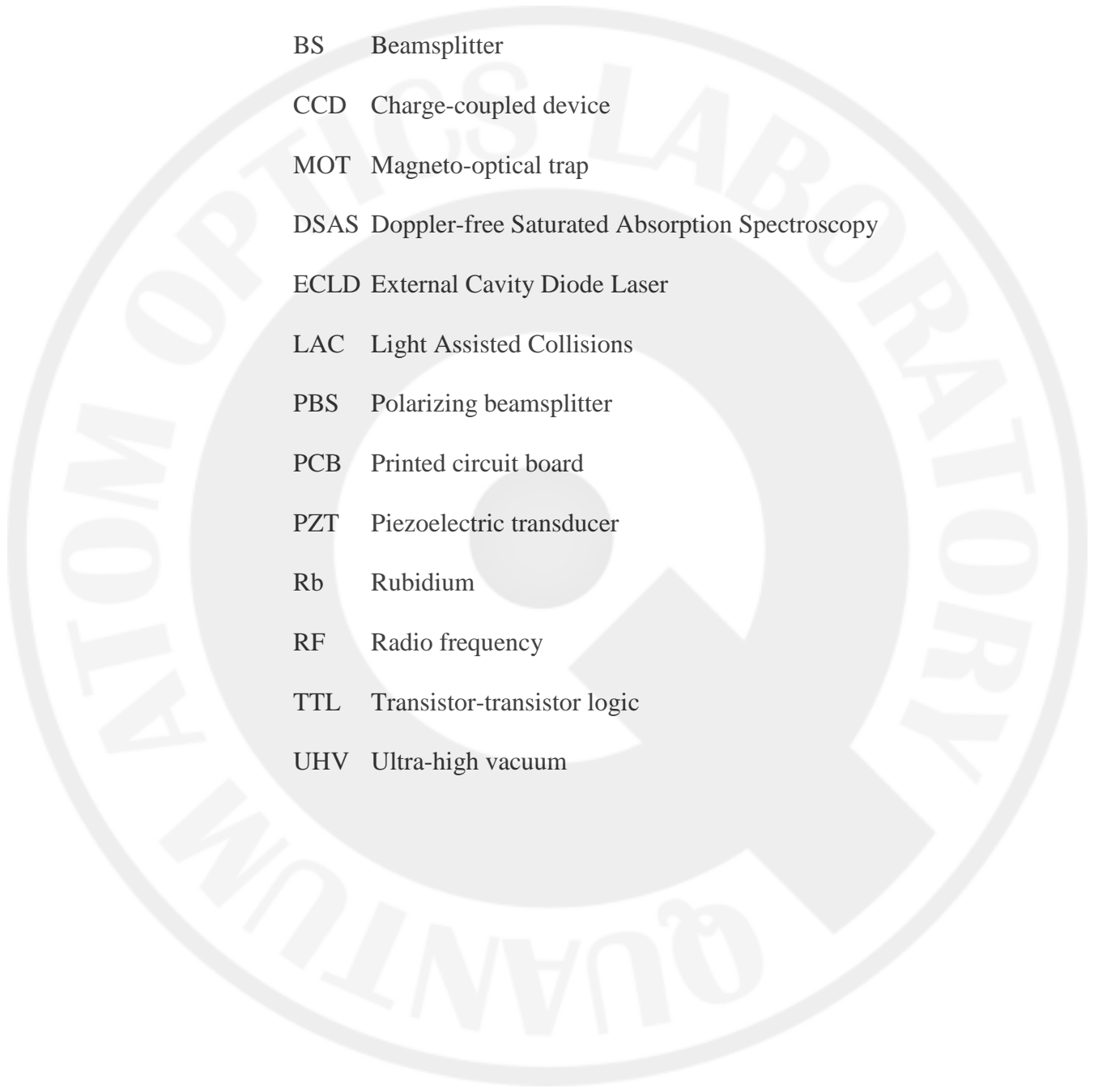
3.6	Alignment of a vacuum system.	30
3.7	Two fiberglass heating tapes wrapped around 2 $\frac{3}{4}$ " and 8" viewports.	33
3.8	The chamber was covered with aluminium foil before baking process.	33
3.9	The magnetic coils in anti-Helmholtz configuration.	35
3.10	Magnetic fields measurement.	35
3.11	A homemade aluminium tube for clamping a high NA lens.	36
3.12	The lens tube was clamped with two diagonal rods inside the chamber.	37
3.13	A homemade aluminium base for clamping a plano convex lens.	38
3.14	The picture of the mounted lens for constructing four-beam MOT.	39
3.15	The optical alignment in the science chamber.	40
3.16	Time line of cooling, loading atoms into the dipole trap, LAC, and imaging.	41
4.1	MOT and repump laser beam profiles after the background subtraction process.	44
4.2	Saturated absorption signal for D2 line transition of $^{85}\text{Rb}$ and $^{87}\text{Rb}$ .	45
4.3	Saturated absorption signal.	46
4.4	Shows the magnetic field computer simulated for the anti-Helmholtz configuration.	47
4.5	Magnetic field along z axis (see Figure 4.4).	47
4.6	Shows the TBT setup.	48
4.7	FBT setup.	50
4.8	The compensation coil (bare coil).	51
4.9	The dipole laser beam profile after the background subtraction process.	52

4.10	The dipole laser wavelength. The maximum intensity is at 827.1 nm.	53
4.11	Light shifts of the energy levels of $^{85}\text{Rb}$ in the dipole trap.	54
4.12	LAC and repump laser beam profiles after the background subtraction.	56
4.13	Saturated absorption signal for D1 line transition of $^{85}\text{Rb}$ and $^{87}\text{Rb}$ .	57
4.14	Saturated absorption signal for (left) F=2 to F' transition.	57
A.1	Energy levels of $^{85}\text{Rb}$ (not to scale).	65
B.1	PCB assembly top of a laser driver circuit.	71
B.2	PCB layout of a laser driver circuit.	71
B.3	Schematic diagram of a laser driver circuit.	72
B.4	PCB assembly top of a temperature controller circuit.	74
B.5	PCB layout of a temperature controller circuit.	74
B.6	Schematic diagram of a temperature controller circuit.	75
B.7	PCB assembly top of a triangular wave generator circuit.	76
B.8	PCB layout of a triangular wave generator circuit.	76
B.9	Schematic diagram of a triangular wave generator circuit.	77
B.10	PCB assembly top of a servolock circuit.	78
B.11	PCB layout of a servolock circuit.	79
B.12	Schematic diagram of a servolock circuit.	80
B.13	PCB assembly top of a fast shutter driver circuit.	81
B.14	PCB layout of a fast shutter driver circuit.	81
B.15	Schematic diagram of a fast shutter driver circuit.	82
C.1	A laser base plate which was improved from [22].	83
C.2	A laser base plate design from [22].	84

C.3	The aluminium block used as a heat sink for stabilizing the laser temperature.	85
C.4	The kinematic mount (U100-P) and its adapter (UPA-PA1) from Newport modified to mount the collimation tube.	86
C.5	An aluminium piece with a 45 degree cut.	87
C.6	A mirror mount providing a fix output laser direction.	88
C.7	Chamber outline showing all optical access through eight 2 $\frac{3}{4}$ " side flanges and two 8" front flanges.	89
C.8	Chamber body is the main body where all experimental events happen.	90
C.9	8" inner flange.	91
C.10	Tube for 2 $\frac{3}{4}$ " flange.	92
C.11	2 $\frac{3}{4}$ " blank flange.	93
C.12	8"blank flange.	94
C.13	Straight rods clamper used to fix four straight stainless steel rods (Figure C.14) in place.	95
C.14	A straight rod. The rod provides straight edge for positioning and mounting a high NA lens.	96
C.15	The High NA lens from Thorlabs.	97
C.16	The mechanical drawing of an aluminium base.	98
C.17	The mechanical drawing of an aluminium tube for a high NA lens.	99
C.18	An aluminium base for mounting the plano-convex lens.	100
C.19	An aluminium piece for locking lens to the aluminium base.	101
C.20	An aluminium piece for clamping the aluminium base to the straight rods.	101

## ABBREVIATIONS AND SYMBOLS

$\hbar$	Reduced Plank constant
$\Gamma$	Natural line width (FWHM), Decay rate
$\gamma$	Reduced natural line width ( $= \Gamma/2\pi$ )
$\tau$	Lifetime ( $1/\Gamma$ )
$\Delta$	Detuning
$\delta$	Reduced detuning ( $= \Delta/2\pi$ )
$\eta$	Index of refraction
$\Delta t$	Time increment
$\Psi$	Wave function
$\omega$	Angular frequency
$\omega_0$	Gaussian beam waist
$\lambda$	Wavelength
I	Intensity
k	Wave number
$k_B$	Boltzmann constant
R	Photon absorption rate
t	Time
T	Temperature
2D	Two dimensions
3D	Three dimensions
AOM	Acousto-optic modulator



ADC	Analog to digital converter
BEC	Bose-Einstein condensate/condensation
BS	Beamsplitter
CCD	Charge-coupled device
MOT	Magneto-optical trap
DSAS	Doppler-free Saturated Absorption Spectroscopy
ECLD	External Cavity Diode Laser
LAC	Light Assisted Collisions
PBS	Polarizing beamsplitter
PCB	Printed circuit board
PZT	Piezoelectric transducer
Rb	Rubidium
RF	Radio frequency
TTL	Transistor-transistor logic
UHV	Ultra-high vacuum

## CHAPTER 1

### INTRODUCTION

#### 1.1 Motivation

An individual addressable neutral atom is a potential candidate on developing a qubit, the building block for quantum computing. Once isolated single atom can be prepared, crafting how to manipulate it would lead to the dynamical control over a system of atoms serving to function essential quantum gates. Because of this, the deterministic separation of a single atom from a cold cloud has been an active research topic and been challenging physicists for more than a couple decades.

To approach the goal, comprehensiveness of the atomic hyperfine structure and the dynamics of cold gases are necessary such that appropriate quantum mechanical processes can be implemented to selectively collect particular number of atoms. In the past year, the technique called “light assisted collision” has caught interest because the recent result using blue-detuned light has shown the single-atom loading efficiency up to 83% [1].

Knocking an atom off a trap predominantly correlates to the two-body collision. However such impact is not likely to occur at the atomic separation defined by the low density of a cold gas that was initially prepared in the magneto-optical trap. Considering a system consisting of two atoms in the hyperfine ground state, an incident photon precisely tuned to a few MHz away from the resonance frequency would drive one atom into a pre-assigned excited state. This process increases the scattering length and therefore induces collisions between the atoms. Consequently

atoms gain kinetic energy from either elastic or inelastic collisions and the large enough kinetic energy would cause one or two atoms to escape the trap [2]. By repeating induced collisions using a laser beam with appropriate frequency, intensity, and duration of exposing, we can lessen the number of atoms in the optical dipole trap until it reaches desirable value.

In this thesis, we constructed a system for preparing a small number of  $^{85}\text{Rb}$  atoms in a far off-resonance optical dipole trap. Laser systems, magnetic system, vacuum system relevant to the experiments are described in this thesis.

## 1.2 Thesis Outline

In Chapter 2 we provide necessary theories related to the experiment. This chapter starts with a review of laser cooling and trapping. Next, theories about a magneto-optical trap, an optical dipole trap, and collisions of cold atoms are explained.

Chapter 3 describes the detail of experimental setup and apparatus including lasers, vacuum system, and imaging system. The circuit schematics and mechanical drawing related to this chapter are provided in Appendix B and Appendix C, respectively.

In Chapter 4 we present results and discussions of the experiments. The beam profile and saturated absorption spectroscopy for each laser is provided. Calculations of magnetic field and magnetic field gradients are provided comparing with an experimental result. The result of MOT is described. We also explain results of dipole trap depth and trap width.

Chapter 5 involves conclusions and future plans of this research.

Finally, the relevant information about the properties of rubidium-85 is shown in Appendix A. Calculations and programming related to this thesis are provided in Appendix D.



## CHAPTER 2

### THEORETICAL BACKGROUND

#### 2.1 Introduction

In this chapter, the methods for cooling and trapping atoms are described. First, a sample of cold atoms are prepared in a magneto-optical trap (MOT). Then, a small fraction of the sample are transferred to an optical dipole trap where the spatial dimension of confinement is reduced. After that, a light assisted collision (LAC) technique is introduced to deliberately reduce the number of atoms in the dipole trap. Finally, the imaging technics for analyzing the MOT and counting atoms in the dipole trap are explained.

#### 2.2 Laser Cooling and Trapping

Consider a stationary atom which has two energy levels and a transition resonance frequency  $\omega_0$ . This atom can absorb a photon which carries energy  $\hbar\omega_0$ , momentum  $\hbar k$ , and angular momentum  $\hbar$ . Upon receiving a photon, the atom undergo a transition to the excited state, recoil in the direction opposite to the photon's propagation and returns to the ground state by emitting a photon into a random direction [3]. The schematic of these processes is shown in Figure 2.1.

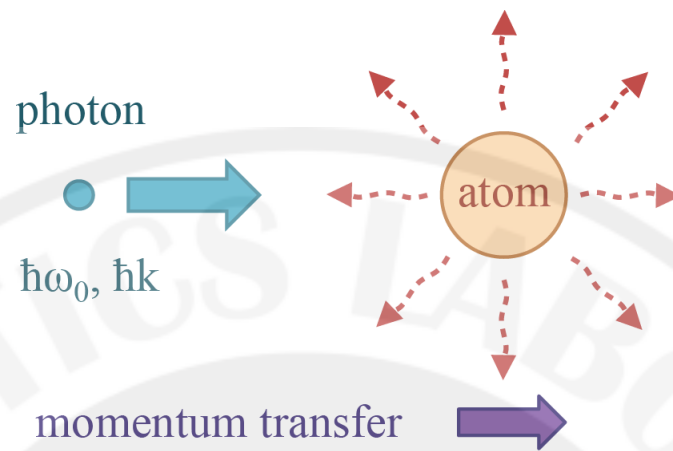


Figure 2.1: A stationary atom obtains the energy and momentum transfer from a photon. Then, it emits a photon in a random direction, indicated by the dash lines.

If an atom with velocity  $\mathbf{v}$  travels opposing the laser beam with a wave vector  $\mathbf{k}$  that is red-detuned by the amount of  $\delta$  from the transition resonance frequency, the atom experiences a Doppler shift by the amount of  $\mathbf{k}\mathbf{v}$  toward the resonance frequency in the atomic frame. The photon absorption rate increases when  $\mathbf{k}\mathbf{v}$  approaches  $\delta$ . After several absorptions and spontaneous emissions, photons are emitted in random directions with a symmetric average distribution. Consequently, the transfers of momentum from absorptions makes the atom slowed down and the momentum from emissions average to zero [4]. The schematic of these processes is shown in Figure 2.2.

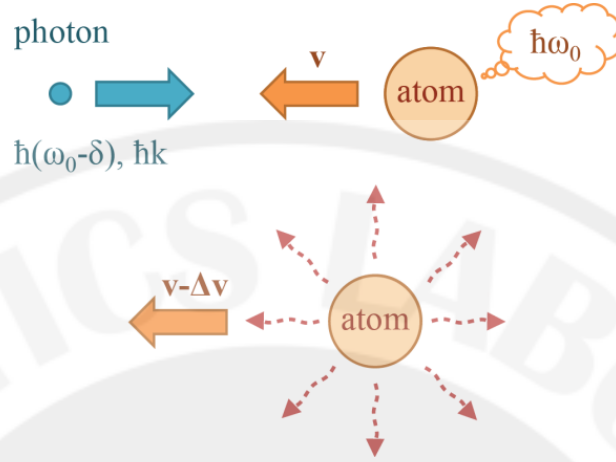


Figure 2.2: Absorption and emission processes of a moving atom. (up) Due to the Doppler shift, a moving atom can absorb photons in a red-detuned laser beam. (down) After several absorptions and spontaneous emissions, the transfers of momentum from absorptions make the atom slowed down.

When we apply three pairs of laser beams along three mutually orthogonal axes in three dimensions to the cloud of atoms in free space, the atomic cloud is slow down within the overlapping volume where the beams intersected. This essentially produces velocity-dependent damping force analogous to when a particle travels in sugar molasses and thus the name “optical molasses [5].”

The competition between laser cooling and spontaneous emission heating also leads to the limit on the lowest possible temperature called Doppler limit  $T_D$  [6] given by

$$k_B T_D = \frac{\hbar \Gamma}{2}, \quad (2.1)$$

where  $\Gamma$  is the natural width of the excited state of the atom.

### 2.3 Magneto-optical Trap

A magneto-optical trap (MOT) has become a standard process for preparing cold atoms in a laboratory [7]. It consists of three counter-propagating laser beam pairs and a pair of anti-Helmholtz coils (Figure 2.3) for the Doppler cooling and a position dependent confinement.

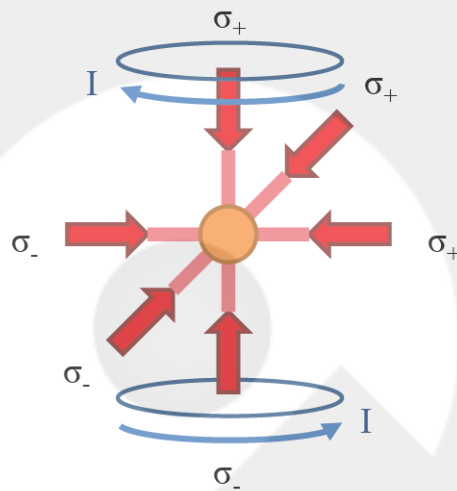


Figure 2.3: Schematic diagram of the magneto optical trap. The symbol  $\sigma_+$  ( $\sigma_-$ ) represents the right (left) handed polarization of a laser beam with respect to the local magnetic field.

The inhomogeneous magnetic field is required to perform a position dependent force for optical molasses trapping [6]. Let us suppose that the laser frequency is fixed to a value that has maximum probability to excite atoms from the ground state  $J=0$  to the hyperfine state  $J=1$  with the lowest Zeeman splitting energy, i.e.  $|J \ m_j\rangle = |1 \ 1\rangle$  for  $B < 0$  and  $|1 \ -1\rangle$  for  $B > 0$  as shown in Figure 2.4.

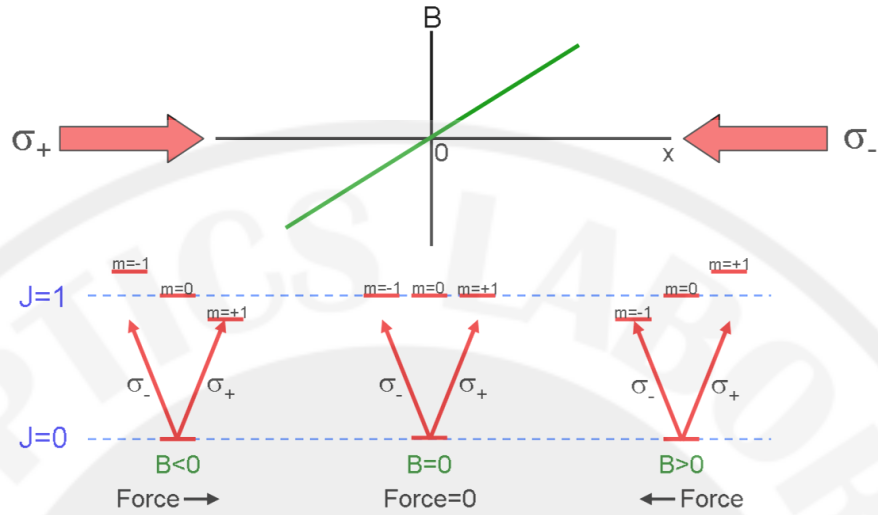


Figure 2.4: Shows hyperfine excitation of atoms in one dimension MOT. The ground state and first excited state are indicated by  $J=0$  and  $J=1$  respectively. Thick red arrows show the red-detuned incident beams with right-handed ( $\sigma_+$ ) or left-handed ( $\sigma_-$ ) polarizations. Allowed transitions are indicated by solid arrows.

Consider a transition of atoms from the ground state  $J=0$  to the excited state  $J=1$  with  $M=0, \pm 1$ , the Zeeman shift of the atomic transition frequencies leads to the state  $M=+1$  shift up and  $M=-1$  shift down for  $B > 0$  and vice versa. If one laser beam propagates to the right with the right-handed polarization  $\sigma_+$  and the counter-propagating one to the left with the left-handed polarization  $\sigma_-$ , the atoms with  $M=+1$  are excited when they move toward  $\sigma_+$  beam and vice versa. Atoms that return to the ground states are slowed down and driven toward the center of the trap where the magnetic field is zero [3].

The motion of atoms in a MOT could be considered from the radiative force. The total force on the atoms is given by  $\vec{F}_{\pm} = \vec{F}_+ + \vec{F}_-$ , where

$$\vec{F}_{\pm} = \pm \frac{\hbar \vec{k} \gamma}{2} \frac{s_0}{1 + s_0 + \left( \frac{2\delta_{\pm}}{\gamma} \right)^2}. \quad (2.2)$$

The detuning for each laser beam is given by

$$\delta_{\pm} = \delta \pm \omega_D \pm \omega_Z, \quad (2.3)$$

where the Doppler shift  $\omega_D = -\vec{k} \cdot \vec{v}$  and the Zeeman shift  $\omega_Z = \mu' B / \hbar$  both have opposite signs for opposite beams.

For the vacuum chamber used in this experiment (the drawing of this chamber is provided in the Appendix C), the conventional scheme of a MOT by using three counter-propagating laser beam pairs could not provide enough space for adding a high NA lens that is used in an optical dipole trap. Consequently, we constructed a four-beam MOT [8, 9] which is shown in Figure 2.5. Two counter-propagating laser beam pairs with opposite polarization handedness are used in this configuration. The first pair, the trapping beams, passes through two lenses with equal focal lengths in the presence of a quadrupole magnetic field and work as typical MOT lasers. An additional pair, molasses beams, is inserted perpendicularly to the direction of the focused beams to increase the capture rate of the trap.

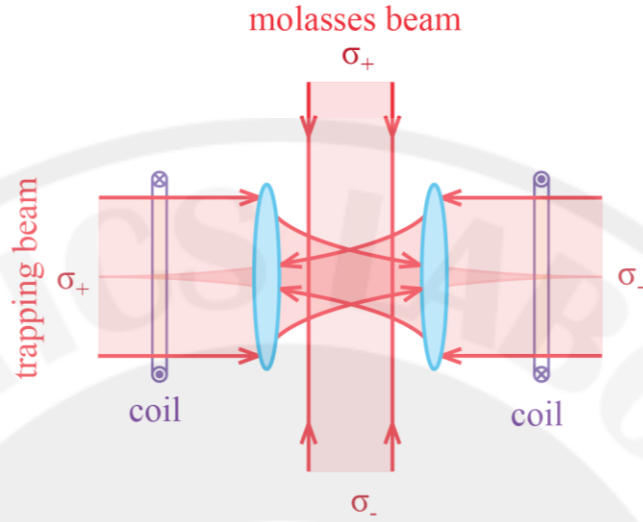


Figure 2.5: Optical alignment for the four-beam MOT. Two lenses with equal focal lengths are added at the center of the trap. The focal length is larger than the distance between the lenses.

Let the trapping beams and the molasses beams align in the  $z$  and  $y$  direction, respectively. Assume that the distance between the position of the minimum beam waist ( $y'$ ,  $z'$ ) is much larger than the Rayleigh length  $y_0 = z_0 = \pi\omega_0^2/\lambda$ . The total force on an atom is given by

$$\begin{aligned}\vec{F}_z(y=0, z, v_z) &= -k_z z - \gamma_z v_z \\ \vec{F}_y(y, v_y, z=0) &= -k_y y - \gamma_y v_y\end{aligned}\quad (2.4)$$

where

$$k_z = -\frac{\hbar k \Gamma \Omega_0^2}{(\delta^2 + \Gamma^2/4)} \left( \frac{z_0^2}{z^3} \right) \left( 1 + \frac{\mu_B b z' \delta / \hbar}{\delta^2 + \Gamma^2/4} \right),$$

$$\gamma_z = \frac{\hbar k^2 \Gamma |\delta| \Omega_0^2}{(\delta^2 + \Gamma^2/4)^2} \left( \frac{z_0}{z'} \right)^2,$$

$$k_y = \frac{\hbar k \Gamma \Omega_0^2}{2(\delta^2 + \Gamma^2/4)} \left( \frac{y_0^2}{y'^3} \right),$$

$$\gamma_{y'} = \frac{\hbar k^2 \Gamma |\delta| \Omega_0^2}{(\delta^2 + \Gamma^2/4)^2} \left( \frac{y_0^2}{y'^4} \right).$$

#### 2.4 Optical Dipole Trap

The optical dipole trap is a system that provides the dipole force in the direction of intensity gradient of the laser, demonstrated by focusing the laser beam which is far-detuned from atomic transition frequency. The electric field from the laser induces a dipole moment in the particle. Since the fields maximum occur at the beam waist, neutral atoms are attracted and confined in that region [10]. The schematic of an optical dipole trap is shown in Figure 2.6.

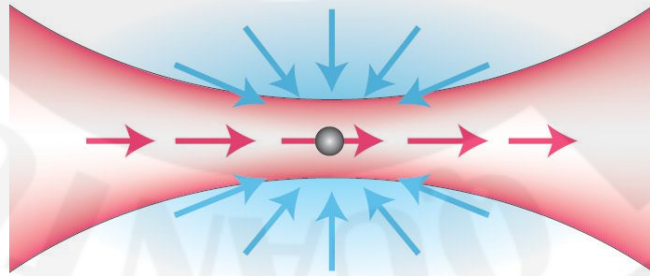


Figure 2.6: The schematic of an optical dipole trap [11]. The red arrows indicate the propagate direction of the atom and the blue arrows indicate directions of the dipole forces.

Unlike other kinds of trapping, the optical excitations are very low due to the fact that the far-off resonance laser is used. Moreover, the trapping mechanism is

independent of the particular sub-level of the electronic ground state and there are various trapping geometries. In this thesis, the descriptive detail of an optical dipole trap is presented by a classical picture using oscillator model and a quantum mechanical treatment using dressed states.

#### 2.4.1 Classical Picture: Oscillator Model

In this model, an atom is considering as a simple oscillator in the classical radiation field [10]. When an atom is subjected to a laser beam, an electric field  $\mathbf{E}$  induces an atomic dipole moment  $\mathbf{d}$  with the amplitude  $\tilde{d} = \alpha(\omega)\tilde{E}$  that oscillates at a driving frequency  $\omega$ . An interaction potential of the induced dipole moment in the driving field is given by

$$U_{dip}(\vec{r}) = -\frac{1}{2}\langle \mathbf{d} \cdot \bar{\mathbf{E}} \rangle = \frac{3\pi c^2}{2\omega_0^3} \frac{\Gamma}{\Delta} I(\vec{r}), \quad (2.5)$$

where  $\omega_0$  is an atomic resonance frequency,  $\Gamma$  is a damping rate,  $\Delta \equiv \omega - \omega_0$  is a detuning, and  $I(\vec{r})$  is intensity.

The sign of detuning illustrate the interaction between atoms and the light field.  $\Delta < 0$  means red detuning and the dipole potential is negative. In this case, atoms are attracted into the location where the field is maximum. While  $\Delta > 0$  means blue detuning and the dipole potential is positive. In this situation, atoms are repelled out of the field. Since the electric field is a conservative field, the dipole force results from the gradient of the interaction potential:

$$\vec{F}_{dip}(\vec{r}) = -\nabla U_{dip}(\vec{r}) = -\frac{3\pi c^2}{2\omega_0^3} \frac{\Gamma}{\Delta} \nabla I(\vec{r}). \quad (2.6)$$

It was found that the direction of the dipole force is proportional to the direction of an intensity gradient. If the Gaussian red-detuned laser beam is used, the dipole force direction could be demonstrated in Figure 2.7.

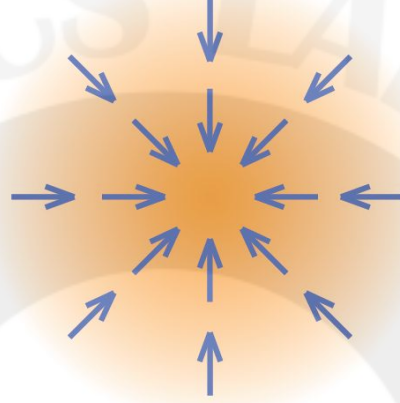


Figure 2.7: Direction of the dipole force constructed by red-detuned laser beam

#### 2.4.2 Quantum Mechanical Treatment: Dressed States

Consider a two-level atom with atomic ground level  $|g\rangle$ , excited level  $|e\rangle$ , and the atomic resonance frequency  $\omega_0$ . If this atom is subjected in the radiation field with photons energy  $\hbar\omega_L$ , the total Hamiltonian is

$$H = H_A + H_L + H_{AL}, \quad (2.7)$$

where  $H_A$  is the atomic Hamiltonian,  $H_L$  is the field Hamiltonian, and  $H_{AL}$  is the atom-field coupling Hamiltonian. The expression of each term is given by

$$H_A = \frac{p^2}{2m} + \hbar\omega_0|e\rangle\langle e|, \quad (2.8)$$

$$H_L = \hbar\omega_L \left( a^+ a^- + \frac{1}{2} \right), \quad (2.9)$$

$$H_{AL} = -\mathbf{d} \cdot \mathbf{E}(r) = -\mathbf{d} \cdot [ |e\rangle\langle g| \mathbf{E}^+(\mathbf{R}) + |g\rangle\langle e| \mathbf{E}^-(\mathbf{R}) ], \quad (2.10)$$

where  $a^+$  and  $a^-$  are the creation and annihilation operator for photons in the laser mode.

In the uncoupled state  $H = H_A + H_L$ , the manifolds  $\varepsilon_n$  are formed and separated by the energy  $\hbar\omega_L$  (Figure 2.8 (left)). Each manifold consist of the state  $|g, n+1\rangle$  which is an atom in the state  $|g\rangle$  in the presence of  $n+1$  photons, and the state  $|e, n\rangle$  which is an atom in the state  $|e\rangle$  in the presence of  $n$  photons. These two states are spaced by the energy  $\hbar\delta$ , where the detuning  $\delta$  between the laser and the atomic frequencies is given by  $\delta = \omega_L - \omega_0 \ll \omega_L, \omega_0$ . The absorption of one photon causes a transition from  $|g, n+1\rangle$  to  $|e, n\rangle$ .

If we take the coupling term  $H_{AL}$  into account, the separation between two states in the manifold is  $\hbar\Omega'(\vec{r}) = \hbar\sqrt{\delta^2 + \Omega(\vec{r})^2}$ , where  $\Omega(\vec{r})$  is the Rabi frequency (Figure 2.8 (right)). These two new eigenstates  $|1, n, \vec{r}\rangle$  and  $|2, n, \vec{r}\rangle$  are called dressed states,

$$|1, n, \vec{r}\rangle = \sin\theta(\vec{r})|g, n+1\rangle + \cos\theta(\vec{r})|e, n\rangle, \quad (2.11)$$

$$|2, n, \vec{r}\rangle = \cos\theta(\vec{r})|g, n+1\rangle - \sin\theta(\vec{r})|e, n\rangle, \quad (2.12)$$

where  $\cos 2\theta(\vec{r}) = -\delta/\Omega'(\vec{r})$  and  $\sin 2\theta(\vec{r}) = \Omega(\vec{r})/\Omega'(\vec{r})$ .

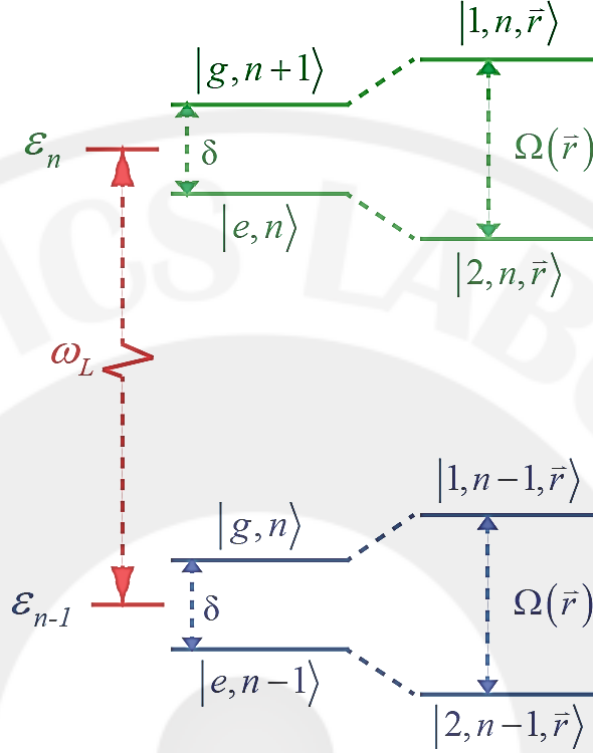


Figure 2.8: Dressed-atom energy diagram. (left) In the uncoupled state, the manifolds are form and separate with  $\hbar\omega_L$ . The separation between two states in the manifold is  $\hbar\delta$ . (right) In the coupled state, the separation between two states in the manifold is changed into  $\hbar\Omega'(\vec{r})$ . Reproduced from ref. [12].

If the Gaussian laser beam is applied to the atom, the separation of energy between each manifold is shown in Figure 2.9. The shift in energy after using Taylor-series expansion to the first order [13] is given by

$$\delta E = \frac{\hbar\Omega' - \hbar\delta}{2} \approx \frac{\hbar\Omega^2}{4\delta}. \quad (2.13)$$

This energy shift can be obtained in terms of the intensity  $I$  and the spontaneous decay rate  $\Gamma$  as:

$$\delta E = \frac{3\pi c^2 \Gamma}{2\omega_0^3 \delta} I. \quad (2.14)$$

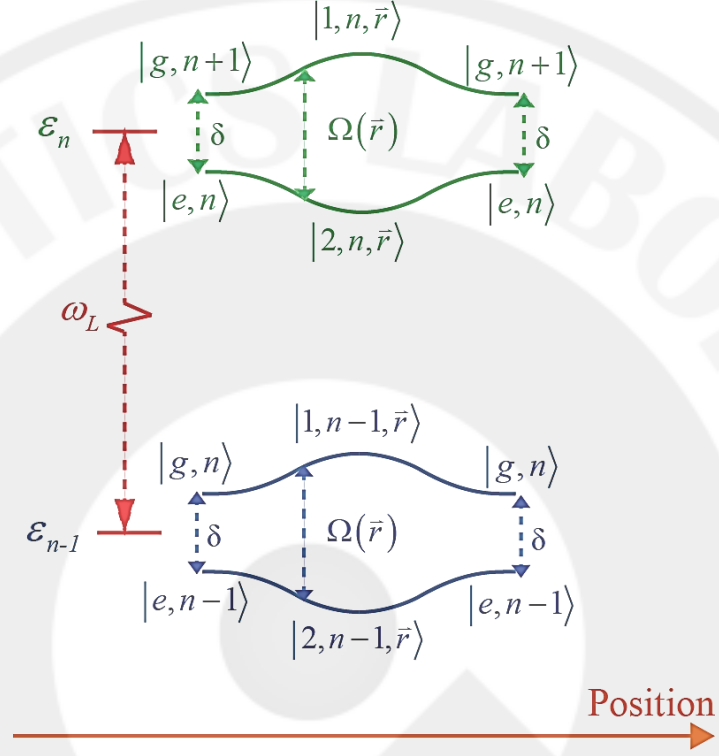


Figure 2.9: The separation of energy between each manifold when a Gaussian laser beam is applied to an atom (reproduced from ref. [12]).

### 2.4.3 Trap Depth Calculation

From Equation (2.10) and Equation (2.14), the spontaneous decay rate  $\Gamma$  is expressed as

$$\Gamma = \frac{\omega_0^3}{3\pi\epsilon_0\hbar c^3} |\langle e | \mathbf{d} | g \rangle|^2. \quad (2.15)$$

For a multilevel atom, the dipole matrix elements can be written as [14]

$$\begin{aligned} \langle e_i | \mathbf{d} | g_i \rangle &= \langle J \| \mathbf{d} \| J' \rangle \\ &\times \left[ \langle F, m_F | F', 1, m'_F, q \rangle (-1)^{F'+J+I_N+1} \sqrt{(2F'+1)(2J+1)} \begin{Bmatrix} J & J' & 1 \\ F & F' & I_N \end{Bmatrix}_{6j} \right]. \end{aligned} \quad (2.16)$$

The  $^{85}\text{Rb}$  dipole matrix elements was calculated in Ref.[15] and are included in Appendix A.

## 2.5 Light Assisted Collisions between Cold Atoms

A Collision between two atoms in the ground state (S-S collision) can be characterized into two processes as shown in Figure 2.10. Atoms can enter repulsive or attractive potential which result in either a pair separation or a molecular formation, respectively.

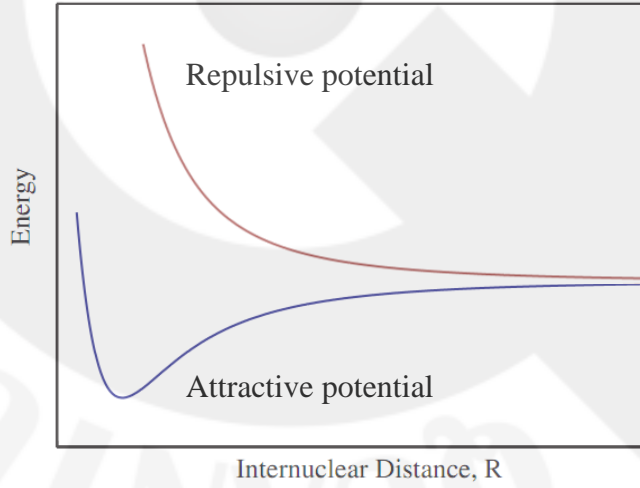


Figure 2.10: The results of collisions between two atoms in the ground state

In a dipole trap, the colliding atom pair can be excited (S-P collision) via thermal energy or under the light near atomic resonance frequency. The collision dynamics is more complicate due to the light shift in fine-structures and the mechanisms may be

largely altered from typical S-S collisions. The potential between atoms is a dipole-dipole interaction and has much larger effective range than the ground state molecular potential. At the atomic separation defined by the density of the cold gas in the dipole trap (indicated with  $R_c$  in Figure 2.12), the ground state potential can be treated as a flat line [1].

The red-detuned light induces the atom pair to an attractive potential to form a molecules. Accordingly, two possible events separately occurred. The first is the normal radiative escape process (RE). The second is the fine-structure changing collision (FS). In both cases, atoms gain large amount of kinetic energy leading to two-atoms lost. The schematic of electronic energy levels of Na atoms with red-detuned light assisted collisions is shown in Figure 2.11.

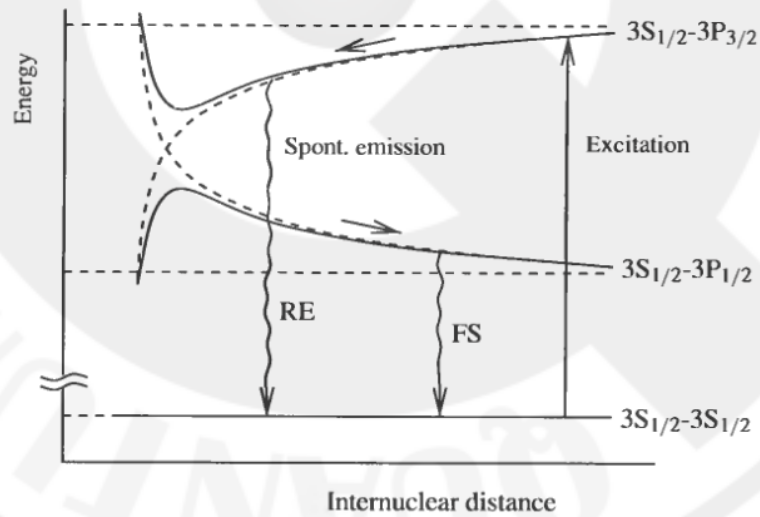


Figure 2.11: The schematic of electronic energy levels of Na atoms with red-detuned light to excite the colliding pair from the ground state  $3S_{1/2}-3S_{1/2}$  to the excited state  $3S_{1/2}-3P_{3/2}$ . Spontaneous emissions occur in both radiative escape process (RE) and the fine-structure changing collision (FS). The two intercepting dash lines show a guideline for the level crossover [3].

In contrast, the blue-detuned light induces atom pair to a repulsive potential. The FS collision is not allowed and the RE could only provide the maximal kinetic energy  $h\delta$ ; which is approximately equal to the trap depth, and leads to one atom loss [1]. The schematic of electronic energy levels of Rubidium atoms with light assisted collisions is shown in Figure 2.12.

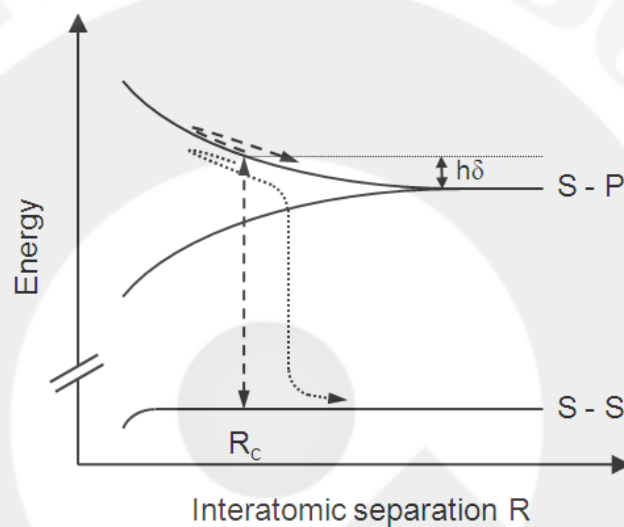


Figure 2.12: The schematic of electronic energy levels of Rubidium atoms. Dash line: energy level change due to the absorption of the blue detuned light at the Condon point ( $R_c$ ). Dot line: the spontaneous emission [1]

## 2.6 Imaging

The fluorescence imaging is used due to the simplicity and suitability to equipment our lab may provide. Taking pictures will be performed in two parts of the experiment; one for analyzing the MOT, the other is to count atoms in the optical dipole trap.

In the optical dipole trap, atoms are exposed to a probing beam, which is a standing wave of light that is small detuned from resonance [16]. In this research

project, the same laser used for collision beam is also employed as a probe beam. A weak proportion is doubly frequency shifted after propagating back and forth through the AOM. This light beam also reflects back to the beamsplitter and combines with the repump beam before enters the vacuum chamber.

According to Figure 3.15 in CHAPTER 3 , the high NA lens is not only used for trapping, but also performs as an objective lens for imaging. The camera for capturing the image of atoms is either the electron-multiplying charge couple device (EMCCD) or the avalanche photo diode (APD). The noise from integrated fluorescence counts is removed using a Fourier transform to filter the unwanted frequency.

## CHAPTER 3

### EXPERIMENTAL SETUP AND INSTRUMENTATION

#### 3.1 Introduction

In this chapter, we describe our experimental setup for light assisted collision (LAC) experiments. We start by describing our setups for the parts where the main experiments takes place: the lasers, vacuum system, and optical alignment. Next, imaging system and data acquisition and software are described.

#### 3.2 Lasers

Lasers are the main apparatuses for trapping and imaging cold atoms. In this experiment, five external cavity diode lasers (ECDLs) in the Littrow configuration with fixed direction output beam were exploited. We used one commercial laser and four homemade lasers. Each homemade laser was based on a design from the University of Melbourne [16]. The schematic of the ECDL used in this work is shown in Figure 3.1 and the details of the components used to construct the ECDL are provided in Table 3.1.

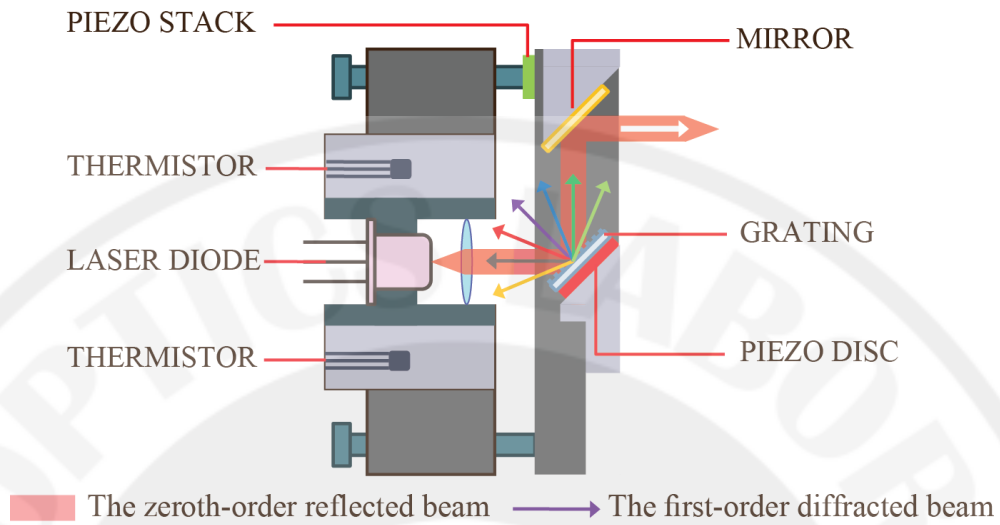


Figure 3.1: ECDL in the Littrow configuration. An output frequency is selected by a feedback from the first-order diffracted beam from a grating. An angle of diffraction is controlled using a higher adjustment screw together with a piezo stack. An external cavity existed between the grating and the back mirror of a laser diode is tuned using a piezo disc. In addition to the standard configuration, a mirror is added after the grating to fix the direction of an output beam regardless of the diffraction angle [16].

The controller and the stabilizer circuits were reproduced from Wieman et al. [17]. The precise measurement of the hyperfine transitions of the  $^{85}\text{Rb}$  atoms was obtained from the Doppler-free saturated absorption spectroscopy (DSAS) using servolock circuits [17]. The circuit schematics and mechanical drawing related to the ECDL are provided in Appendix B and Appendix C, respectively. Details of the lasers used in this research are described below.

Table 3.1: Details of components used to construct the ECDL

Type	Part Number	Company	Details
Laser diode	L785P100	Thorlabs	785 nm, 90 mW CW (220 mW Pulsed), Ø5.6 mm , A Pin Code
	HL8338MG	Thorlabs	830 nm, 50 mW, Ø5.6 mm, C Pin Code
	EYP-RWE-0840-06010-1500-SOT02-0000	Eagleyard	810 nm GaAs Semiconductor Laser Diode
Grating	33001FL02-330H	Newport	15×15×3.2 mm 1800 Groove 500 nm Holographic Grating
Collimation tube	LT110P-B	Thorlabs	5.6 mm and 9 mm Laser Package, Collimation Tube with Optic, 0.85" Package Length
Mirror mount	U100-P	Newport	Precision Platform Mirror Mount, 2.0 x 2.0 in., No Actuators, 8-32 (M4) CLR
Knob	AJS100-0.5K	Newport	High Precision Large Knob Adjustment Screw, 12.7 mm

### 3.2.1 MOT Laser

An ECDL from MOGLabs model ECD-003 with a laser diode DL-780AP150 (typical lasing wavelength 785 nm) was used for the cooling and trapping of  $^{85}\text{Rb}$  atoms. It was driven by a laser controller and stabilizer from MOGLabs model DLC-202. The temperature of the laser was set at 20.04 °C and it was detuned  $\sim 15\text{MHz}$  to the red of the D2 line,  $(F=3)5_2S^{1/2} \rightarrow (F'=4)5_2P^{3/2}$  transition. The output from the MOT laser was 80 mW. A  $\lambda/2$  waveplate and a polarizing beam splitter (PBS) divided  $\sim 1\text{ mW}$  of power from the laser to a DSAS setup. The remaining 78 mW of the laser beam was combined with the repump laser using a PBS. The schematic diagram of the MOT laser alignment can be seen in Figure 3.2(a).

### 3.2.2 Repump Laser

There exists a possibility that the MOT laser excites some atoms to the state  $(F'=3)5_2P^{3/2}$  and the atoms make a transition back to  $(F=2)5_2P^{3/2}$ , which was inaccessible to the MOT laser. The repump laser is, therefore, necessary to pump the atoms back to  $(F=3)5_2P^{3/2}$ .

The repump laser was constructed from a homemade ECDL using a laser diode L785P100 from Thorlabs typically lasing at 785 nm. It was driven by a homemade driver and stabilizer, which tuned the laser to the D2 line,  $(F=3)5_2S^{1/2} \rightarrow (F'=3)5_2P^{3/2}$  transition. The output from the repump laser was 64 mW. A  $\lambda/2$  waveplate and a PBS divide  $\sim 1$  mW from the laser to a DSAS setup. The remaining 30 mW of the laser beam was combined with the MOT laser.

The size of the combined beam was expanded using two lenses with focal lengths of 25mm and 150mm, respectively. The diameter of the beam was increased from 3mm to 18mm. This beam was divided into four beams of equal power by  $\lambda/2$  waveplates and PBSs. Each beam was made circular polarized by a  $\lambda/4$  waveplate before entering the vacuum chamber. Two beams were used as trapping beams and two remaining beams were used as molasses beams. The schematic diagram of the repump laser and the alignment of the combined beams can be seen in Figure 3.2(b) and Figure 3.2(c), respectively.

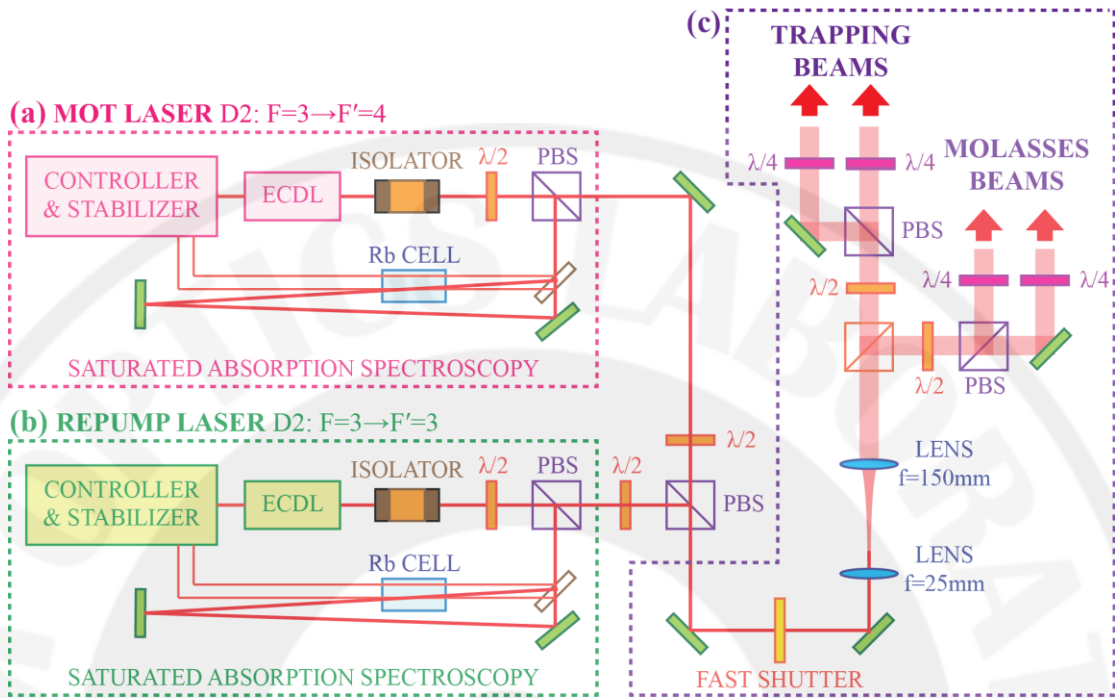


Figure 3.2: The schematic diagram of the optical alignment of (a) MOT laser, (b) repump laser, and (c) combined beam.

### 3.2.3 Optical Dipole Laser

The optical dipole laser was constructed from a homemade ECDL using a laser diode HL8338MG from Thorlabs typically lasing at 830 nm. It was driven by a homemade driver and stabilizer. The output power from the optical dipole laser was 35 mW and the output wavelength was 827 nm. This laser was aligned to a high NA lens in the science chamber. The laser power before enter the chamber is 25.8 mW.

### 3.2.4 Collisions and Probe Laser

A collisions and probe laser is constructed from one homemade ECDL using a laser diode EYP-RWE-0840-06010-1500-SOT02-0000 from Eagleyard with a typical

lasing wavelength of 810 nm. It was driven by a homemade driver and stabilizer. The laser was tuned near the D1 line,  $(F=2)5_2S^{1/2} \rightarrow (F'=3)5_2P^{1/2}$  transition. The output from this laser was 33 mW. A  $\lambda/2$  waveplate and a PBS divide 1 mW from the laser to a DSAS setup. The remaining 22 mW is set to have a horizontal polarization using a  $\lambda/2$  waveplate before transmitting through a PBS. This beam then passed through an acousto-optic modulator (AOM) model 1206C from ISOMET using the double pass configuration. This AOM is modulated by a 630C-110 variable frequency driver from ISOMET at 246MHz for assisted collisions, and then at 170MHz for imaging. The laser beam reflects back to the PBS and combines with the LAC repumping laser (described below). The schematic diagram of the collisions and probe laser can be seen in Figure 3.3(a).

### 3.2.5 LAC repumping laser

The repumping laser for LAC was constructed from a homemade ECDL using a laser diode EYP-RWE-0840-06010-1500-SOT02-0000 from Eagleyard GmbH with a typical lasing wavelength of 810 nm. It was driven and stabilized by a homemade driver and stabilizer. The laser was tuned to the D1 line,  $(F=3)5_2S^{1/2} \rightarrow (F'=3)5_2P^{1/2}$  transition. The output from the LAC repumping laser is 33 mW. A  $\lambda/2$  waveplate and a PBS seeded 1 mW from the laser to a DSAS setup. The remaining 22 mW of the laser beam was combined with the collisions and probe laser using a  $\lambda/2$  waveplate and a PBS. A fast shutter was placed before the beam enters the vacuum chamber to gate the laser on and off according to the time sequences related to the LAC processes as described in section 3.6.2 and Figure 3.16. The schematic diagram of the collisions

and probe laser can be seen in Figure 3.3(b). The circuit schematic of the fast shutter is provided in Appendix B.

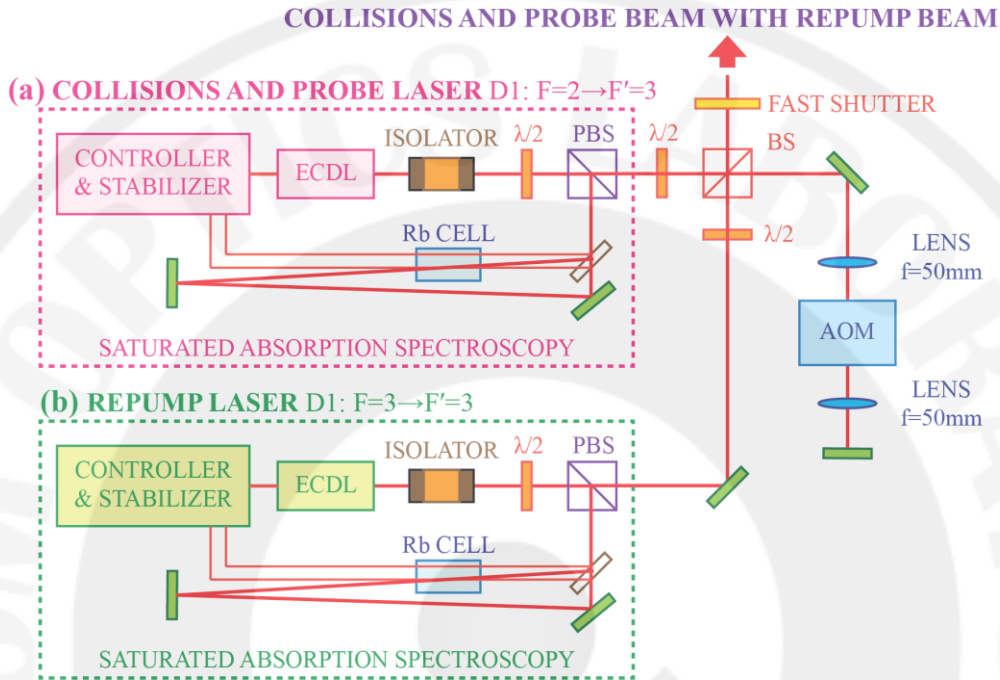


Figure 3.3: Schematic diagram of (a) the collisions and probe laser (b) the LAC repumping laser. All these beams were combined using a PBS and controlled by a fast shutter.

### 3.3 Vacuum System

#### 3.3.1 Chamber Design

A science chamber used in this experiment was SLRI-SW-CMU-540089 from the Synchrotron Light Research Institute. This chamber was designed to have four straight rods mounting inside across the chamber for clamping optical components. The mechanical drawing of this chamber was provided in Appendix C. The schematic of this chamber is shown in Figure 3.4.

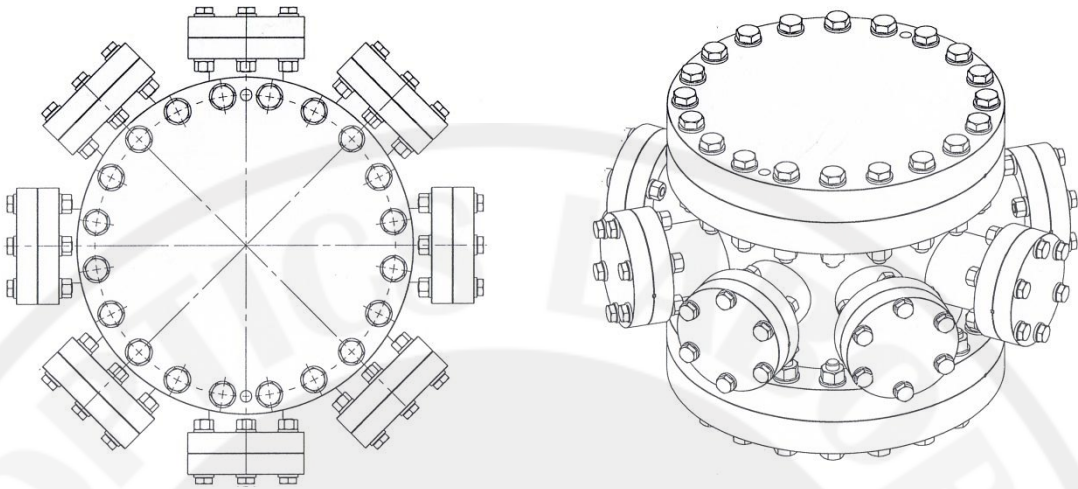


Figure 3.4: Schematic of the science chamber used for cooling and trapping Rb atoms. This stainless steel chamber had a diameter of 280mm and a height of 190mm. Eight ports were standard  $2\frac{3}{4}$  ConFlat (CF) flanges. The other two ports were 8" CF flanges. (left) Top view. (right) 3D view.

The viewports used with this chamber are from MDC. The large flanges were fitted with 8" zero profile viewports (Part No.: 450008) without coating, together with 8" copper gaskets (Part No.: 191017). The remaining small flanges were  $2\frac{3}{4}$ " in diameter. Six of them were fitted with  $2\frac{3}{4}$ " zero profile viewports (Part No.: 450002) with anti-reflection coated at 780-830nm. The remaining two ports were connected with a Rb dispenser assembly and a vacuum system, respectively. All  $2\frac{3}{4}$ " flanges were used with  $2\frac{3}{4}$ " copper gaskets (Part No.: 191004).

The rubidium dispenser assembly contains an electrical feedthrough (Part No.: 9452014) from MDC and three Rb getters (RB/NF/3.4/12 FT10+10) from SAES. Each getter had an active length of 12 mm and contains 4.5mg of Rb. The getters were locked with the feedthrough pins using copper rings as shown in Figure 3.5. A current source for the Getters was a power supply 7.5V 300A (TCR 7.5S300) from Electronic Measurement Inc.

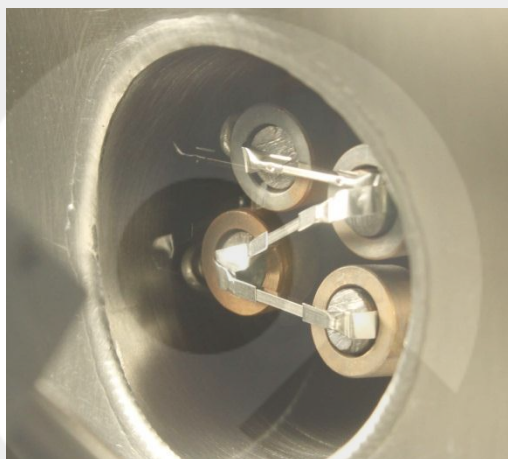


Figure 3.5: Rubidium dispenser assembly. Three Rubidium getters were attached to the feedthrough pins in an N shape using copper rings. This alignment provided more space for a high current clamping outside the vacuum chamber.

The alignment of the vacuum system attached to the science chamber is shown in Figure 3.6.

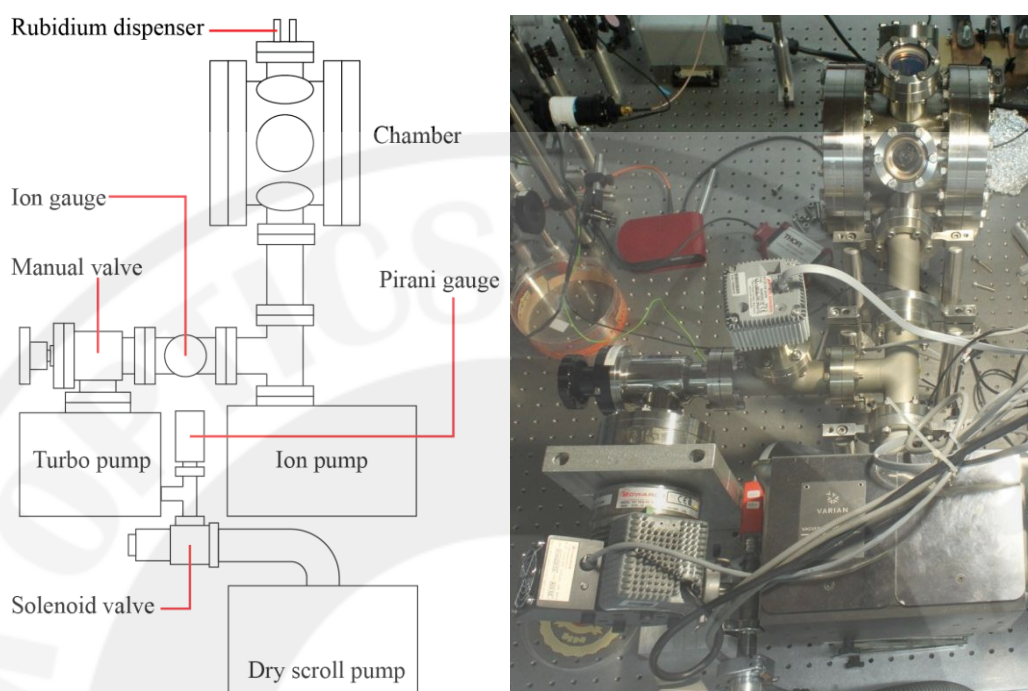


Figure 3.6: Alignment of a vacuum system. The vacuum chamber was connected with pumps, gauges and valves. (left) Schematic diagram of alignment. (right) Picture of the real system.

The chamber was attached with an ion pump and an ion gauge which was connected to a manual valve. These assemblies were joined using  $2\frac{3}{4}$ " CF flanges. After that, the valve was attached to a turbo pump using a 4.5" CF flange. The turbo pump was joined to a pirani gauge using a NW16 flange and to a solenoid valve using a NW26 flange. Lastly, the solenoid valve was connected to a dry scroll pump via a vacuum bellow. Details of these apparatuses are provided in Table 3.2.

Table 3.2: Details of vacuum apparatuses used in this experiment.

Type	Part Number	Company	Details
Pump	MC-INV-10-11-0118	Varian	Ion Pump Valcon Plus 40 Diode with additional 2 3/4" CFF port P/N. 919 1213
	A72401903	Edwards	XDS5 Dry Scroll Pump
	B72242000	Edwards	EXT75DX Compound Turbomolecular Vacuum Pump
	B58053075	Edwards	ACX75 Air Cooler (Attached with Turbo Pump)
Controller	D39721000	Edwards	TIC Turbo & Instrument Controller
	9290290	Varian	MiniVac Ion Pump Controller
Gauge	D04852000	Provac	AIGX-S-DN40CF S/S Active Ion Gauge
	D02601000	Edwards	APG100 Active Pirani Vacuum Gauge
Valve	C41752000	Edwards	LCPV25EKA Solenoid Operation Isolation Valves
	SA0150 MVCF	Kurt J. Lesker	Manual Bellows Sealed SS Angle Valves (CF flanged)
Gasket and Ring	191004	MDC	CopperGaskets, 2.75"
	191009	MDC	CopperGasket, 4.5"Flange
	710000	MDC	CenteringRing, NW16, Viton, SS
	710001	MDC	CenteringRing, NW25, Viton, SS

### 3.3.2 Chamber Construction

First of all, we had to clean all components inside the chamber, consist of (1) two aluminium bases for clamping plano-convex lenses (2) an aluminium tube for clamping a high NA lens and (3) four straight stainless steel rods for mounting the aluminium bases and tube to the science chamber. They were cleaned in detergent, ethanol 99.8%, and acetone, respectively. After that, we baked them under the temperature of 60°C for 30 minutes before aligning them in the chamber (See section 3.5 for more detail).

After the entire vacuum system had been assembled, we loosen the manual valve and started pumping the chamber by

- (1) Turned on the dry scroll pump and the solenoid valve.
- (2) Turned on the TIC Turbo & Instrument Controller to activate a pirani gauge.
- (3) When the pressure was below  $10^{-1}$  torr, turned on the turbo pump.
- (4) Waited for the turbo pump to run to the full speed. Then, turned on an ion gauge. The pressure should be read at  $10^{-6}$  torr. Checked for leaks by spraying a small amount of ethanol on all flanges. If there was a leak, the pressure would change when the ethanol was applied.
- (5) Started baking processes (See section 3.3.3) with the turbo pump for 12 hours.
- (6) Turned on an ion pump. The pressure of chamber should be at  $10^{-8}$  torr. When the pump ran at lowest current, turned off the solenoid valve, the turbo pump, and the dry scroll pump.

### **3.3.3 Chamber Bake out**

The bake out process at high temperatures is necessary for removing contaminants to reach high vacuum pressures. Before baking process, we checked the availability of Rb by applying 6A current to the getters, which could be seen from fluorescence. After that, we wrapped the stainless parts of the chamber using two fiberglass heating tapes with resistances  $40.5 \Omega$  and  $41.5 \Omega$  as shown in Figure 3.7. The tape should not overlap itself for prevent overheating. Then, we covered a whole chamber using aluminium foil as shown in Figure 3.8.



Figure 3.7: Two fiberglass heating tapes wrapped around 2 $\frac{3}{4}$ " and 8" viewports.



Figure 3.8: The chamber was covered with aluminium foil before baking process.

To bake the chamber, we started with applying a 0.2 A current to the heating tapes using a power supply SD-12 from Stendal. The average temperature of the chamber would be  $\sim 50$  °C in an hour. Then, we applied more current to increase the temperature of the chamber in an order of 50°C per hour or slower. Note that the different temperature between the coldest part and the hottest part should not more than 30°C to avoid damaging the viewports. We heated the entire chamber until reaching 200°C. During the baking processes, a 3A current was continuously applied to the getters to prevent contamination and to degas the getters.

### **3.4 Magnetic Coils**

Two coils in the anti-Helmholtz configuration were constructed from a copper wire of diameter 2.00 mm (SWG#14). The wire was wound into two 102-turn coils (wound 3 rows, each row has 34 turns) with an inner diameter of 210 mm and an outer diameter of 222 mm. The coils were placed in the vertical plane, covered the 8" viewports as shown in Figure 3.9.

The distance between the two coils was about 10 cm. A DC current of 7.25V 9A was supplied to the coils by a power supply 7.5V 300A (TCR 7.5S300) from Electronic Measurement Inc. Magnetic fields between these two coils were measured using a Hall probe and a teslameter from PHYWE as shown in Figure 3.10.

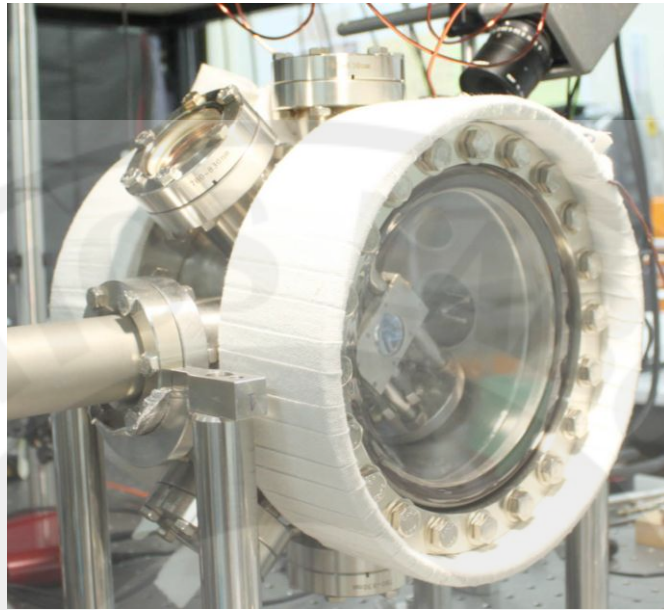


Figure 3.9: The magnetic coils in anti-Helmholtz configuration after clamping. They covered the 8" viewports with an equal distance from the center to provide a zero magnetic field at the center of a chamber.

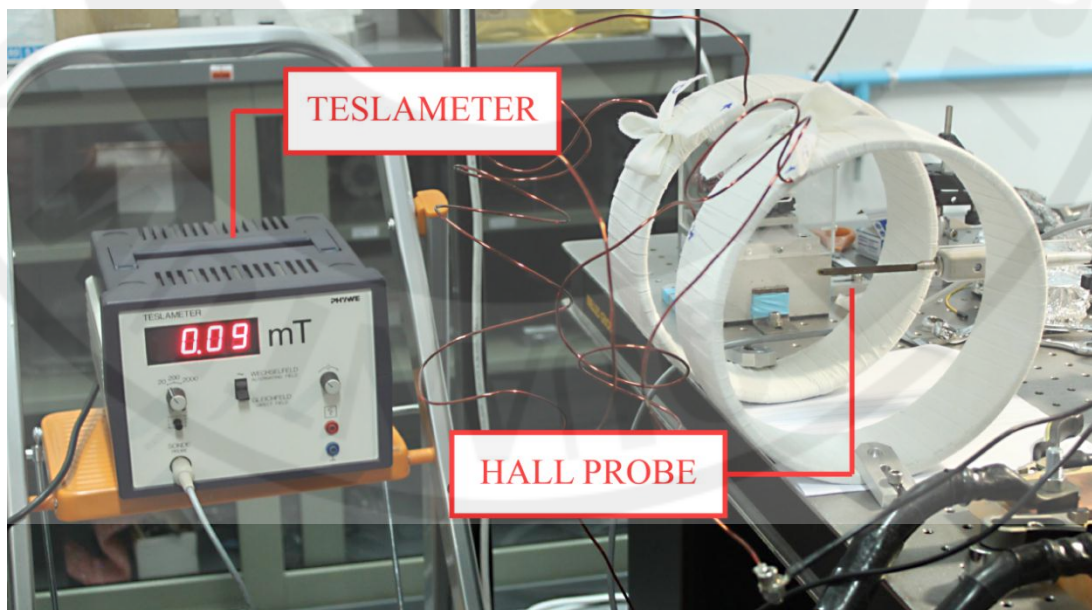


Figure 3.10: Magnetic fields measurement. The Hall probe was set between two coils and moved horizontally.

### 3.5 Optical Alignment

When all components were cleaned, we start the alignment by mounting the straight rods inside the chamber. These rods were aligned 45 degree from the plane. Then, we aligned the dipole laser with a High NA lens. After that, the MOT and repump laser was aligned to pass a pair of plano-convex lenses. Finally, the collisions and probe laser with repump laser were set using retroreflection configuration.

#### 3.5.1 Dipole laser

To construct an optical dipole trap, the dipole laser must be focused at center of the MOT using a high NA lens. In this experiment, we used the high NA lens (C240TME-B) from Thorlabs. This lens was mounted with a homemade aluminium tube as shown in Figure 3.11. The mechanical drawing of the aluminium tube was provided in Appendix C.



Figure 3.11: A homemade aluminium tube for clamping a high NA lens.

After that, we clamped the lens tube with two diagonal rods inside the chamber as shown in Figure 3.12. The distance between the flat surface of the lens to the center of chamber was  $\sim 5\text{mm}$ . We could check this by applying the dipole beam into the chamber. The beam waist should be in the same plane with the centering mark of four rods.

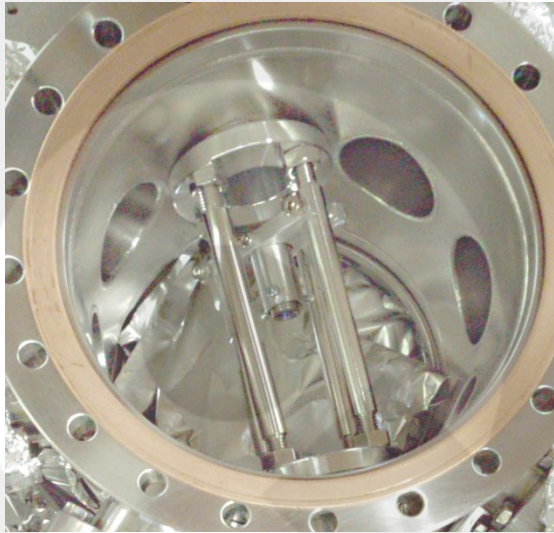


Figure 3.12: The lens tube was clamped with two diagonal rods inside the chamber.

### 3.5.2 MOT and Repump laser

In the four-beam trap configuration, one counter-propagating laser beam pair, called trapping beams, passed through two lenses with equal focal lengths. Another pair, called molasses beams, was inserted perpendicularly to the direction of the focused beams. To construct this configuration, we mounted two plano-convex lenses (PCX0302) from CASIX with two homemade aluminium bases as shown in Figure 3.13. The mechanical drawing of the aluminium base is provided in Appendix C.

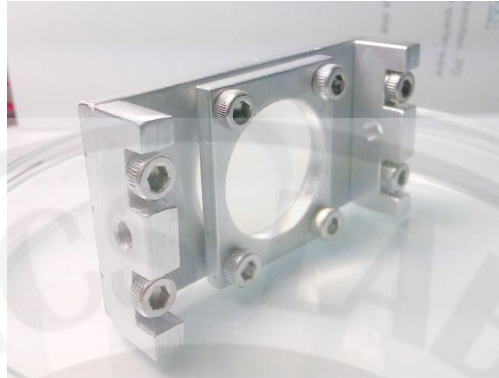


Figure 3.13: A homemade aluminium base for clamping a plano convex lens.

Before clamping the lens base inside the chamber, we had to align the trapping beams to perfectly intersect each other. Note that the beam waist of the dipole laser must be positioned at the center of the trapping beam. Then, we clamped one lens base with two diagonal rods inside the chamber. The base was arranged in the position that the focal point of the beam was located at the center of another beam. Next, we clamped another lens base and check the position of its waist to be centered of another beam. The picture of the mounted lens is shown in Figure 3.14.

When finished aligning the trapping beams, the molasses beams were applied perpendicularly to the dipole beam and intersected with the trapping beams. The beneficial from alignment the molasses beams in this direction was that they were not blocked by the high NA lens.

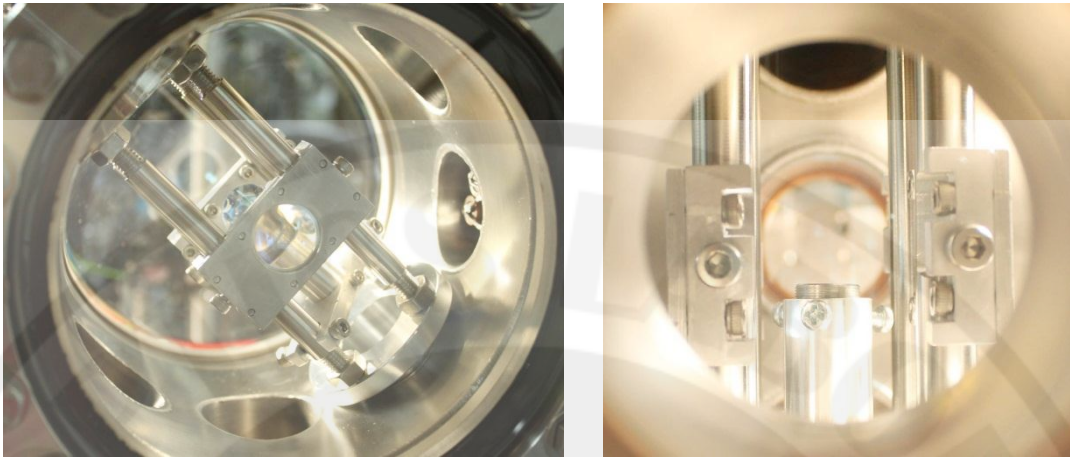


Figure 3.14: The picture of the mounted lens for constructing four-beam MOT. (left) Front view from 8" viewport. (right) Side view from 2 $\frac{3}{4}$ " viewport.

### 3.5.3 Collisions and Probe laser with Repump laser

The collisions and probe beam together with the repump beam were aligned in the vertical direction. They passed through a plano-convex lens with focal length 150mm before entered the chamber from the upper 2 $\frac{3}{4}$ " viewport. The beams waist must be aligned to intersect with the waist of the dipole laser. Then we used the retroreflection configuration by adding a plano-convex lens with the same focal length and a broadband dielectric mirror at the opposite viewport.

In conclusion, the optical alignment in the science chamber is shown in Figure 3.15.

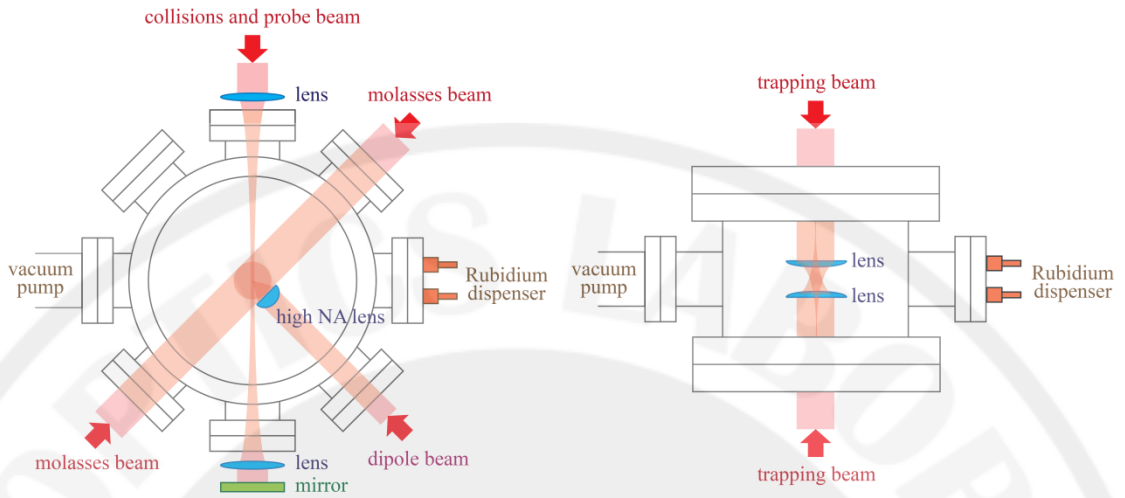


Figure 3.15: The optical alignment in the science chamber. (left) Collisions and probe beams, molasses beams, a dipole beam and lenses alignment from front view. (right) Trapping beams and lens alignment from top view.

### 3.6 Imaging System

#### 3.6.1 MOT Imaging

A CCD camera is used to detect the fluorescence from  $^{85}\text{Rb}$  atoms in the science chamber. The camera is located at the only available viewport left (see Figure 3.15). The camera is turned on in the video mode to capture every processes occur in the MOT experiment.

#### 3.6.2 Optical Dipole Trap and LAC Imaging

In our experiment, we reduced the processes used in the original LAC setups that are carefully designed to achieve a deterministic single atom trap as described in Ref. [1]. We remained only seven steps necessary to trap a hundred atoms or below in order to demonstrate the essence of the LAC technique. Together with a new

configuration of MOT, our setup created the simplest design to demonstrate the LAC in an ensemble below hundred atoms. Our simplified controlling sequences are shown in Figure 3.16.

TYPE	TARGET	OUTPUT	TIMELINE												
TTL	MOSFET	Quadrupole Coils	MOT												
TTL	Fast shutter	MOT and Repump lasers	MOT												
TTL	Fast shutter	Dipole laser		Dipole Loading											
ANALOG	AOM +246 MHz	Collisions and Repump Lasers			LAC										
TTL	Fast shutter														
ANALOG	AOM +170MHz	Probe and Repump Lasers													
TTL	Fast shutter														
TTL	Camera	Camera													
Interval time (ms)			500	150	30	5	10	20	10	20	10	20			

Figure 3.16: Time line of cooling, loading atoms into the dipole trap, LAC, and imaging. The interval time of LAC could be changed to optimize the number of atoms in the dipole trap.

The controlling systems could be divided into two sections. The first section included programming in Python for communication between computers and microcontrollers. The second section was using PIC microcontroller for triggering and

controlling optical and mechanical components. This part was contributed by N. Chattrapiban, P. Chaiwonkot, and C. Kamrapis.

Python was the main language used for communication between computers and PIC microcontrollers. In this research, we constructed a program in Python to provide synchronized signals to PIC microcontrollers and camera shutter. Moreover, some variable parameters, i.e. interval time of LAC and camera exposure time, could be directly input via this program. The output signals were sent via a parallel port in the form of TTL.

PIC microcontroller was used to control optical and mechanical components. After receiving the trigger signal from the computer, PIC could export both TTL and analog signals to the target components. According to Figure 3.16, TTL signals were sent to quadrupole coils, lasers, and a camera. While analog signals were sent to AOM for frequency shifting between collisions and probing support

Although the data acquisition has already prepared for the experiment, we require a high quality EMCCD camera to observe few hundreds of rubidium atoms.

## CHAPTER 4

### RESULTS AND DISCUSSIONS

#### 4.1 Introduction

In this chapter, we present results of our experiments including the MOT, the optical dipole trap, and the LAC. The laser beam profiles and spectroscopy in each setup are disclosed. The magnetic field from the coils is calculated and measured. In addition, we also determined the optical dipole trap depth from the dipole laser beam profile. The programming reference code for background subtraction process is provided in Appendix D.

Without a high quality CCD camera and an avalanche photodiode, we observed the beam profiles and the saturated absorption signal using a CCD camera (DCU223C) from Thorlabs and modified USB web cameras.

#### 4.2 Magneto-optical Trap

##### 4.2.1 MOT and Repump Laser Beams Profiles

The profiles of the MOT and repump laser beams at the center of the science chamber were demonstrated outside the chamber by applying these laser beams through a 50mm lens (the same lens used inside the chamber). Pictures of the laser beams and a background (laser beams turned off) were captured using the CCD camera (DCU223C) from Thorlabs. After the background subtraction process, the true beam profiles are shown in Figure 4.1.

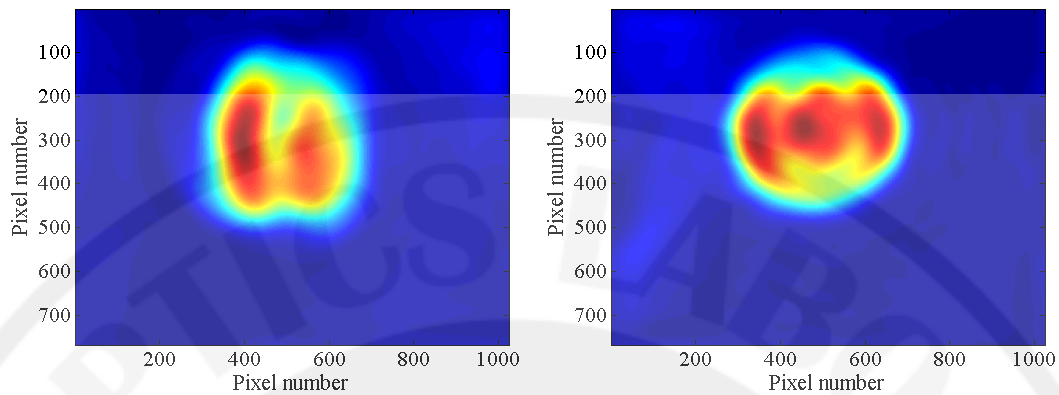


Figure 4.1: MOT and repump laser beam profiles after the background subtraction process. Deep red color represents maximum intensity while the beam edge is approximated by light blue color. (left) The MOT beam profile. (right) The repump beam profile.

The laser beams were not in the Gaussian shape and have fringes at the center of the beams. These fringes represent interferences of the laser from the laser diode aperture. The spatial shape may be improved by

- (1) cleaning the laser beams using a small pinhole and two lens. The beam profile will be in the Gaussian shape but the power will be dramatically decreased. This method can be used if we have a high power laser source, e.g. amplifying the laser power using a taper amplifier.
- (2) cleaning the laser beams using single mode optical fibers. Similar to (1) that the laser power will be decreased.
- (3) applying each laser beam through an anamorphic prism pair. This method transforms elliptical laser beams into nearly circular beams.

### 4.2.2 Doppler-free Saturated Absorption Spectroscopy

By observing the DSAS from our homemade lasers, the absorption profile for D2 line transition is shown in Figure 4.2. We locked the MOT beam at  $F=3 \rightarrow F'=4$  transition and the repump beam at  $F=2 \rightarrow F'=3$  transition as shown in Figure 4.3.

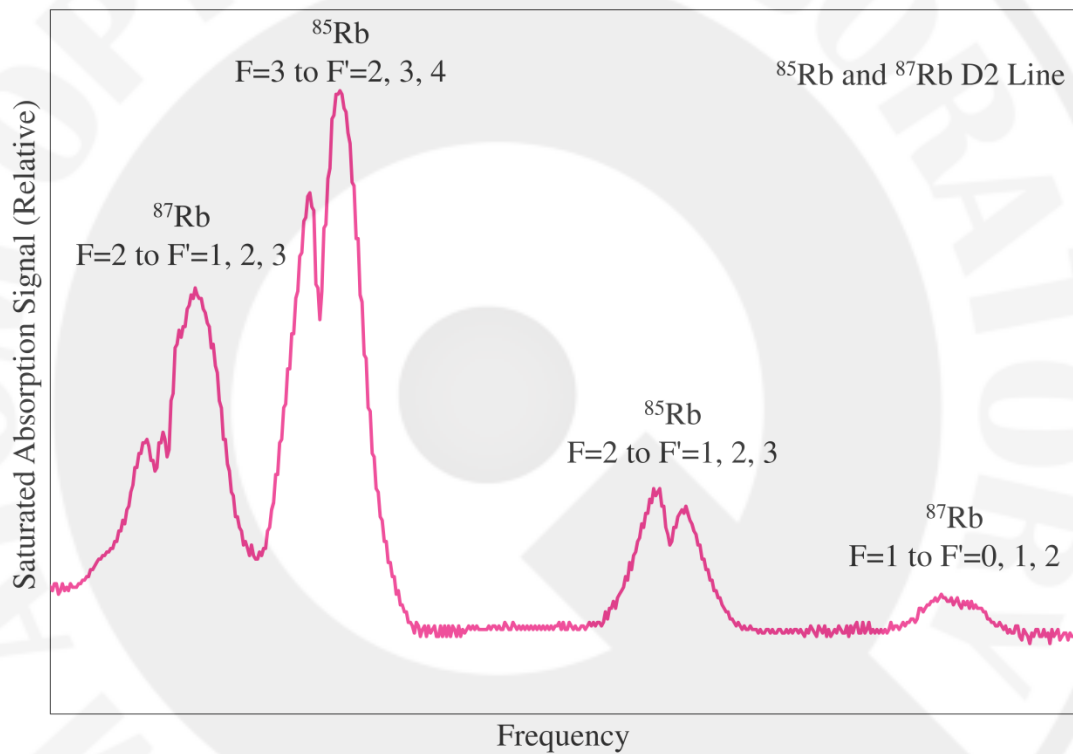


Figure 4.2: Saturated absorption signal for D2 line transition of  $^{85}\text{Rb}$  and  $^{87}\text{Rb}$ .

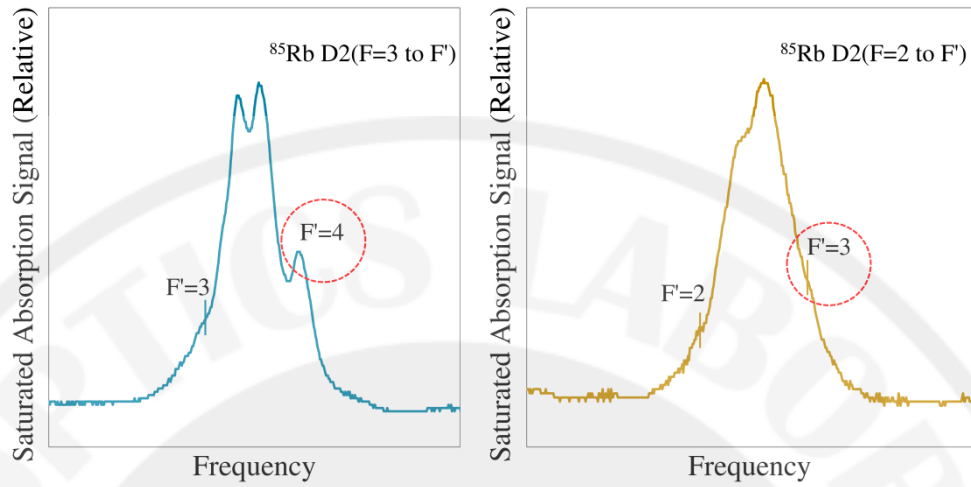


Figure 4.3: Saturated absorption signal for (left)  $F=3$  to  $F'$  transition. The dash circle indicates the frequency of the MOT beam, which was locked at ( $F=3 \rightarrow F'=4$ ) transition. (right)  $F=2$  to  $F'$  transition. The dash circle indicates the frequency of the repump beam, which was locked at ( $F=2 \rightarrow F'=3$ ) transition.

### 4.2.3 Magnetic Coils

The simulation magnetic field line of the coils is given in Figure 4.4 and Figure 4.5. The MOT was constructed at the center between two coils (origin of this picture) which had zero magnetic field.

The magnetic field gradient measured from the teslameter was  $\sim 8$  Gauss/cm at the center between two coils (origin of Figure 4.5), which corresponds to the calculation from MATLAB in Appendix D.

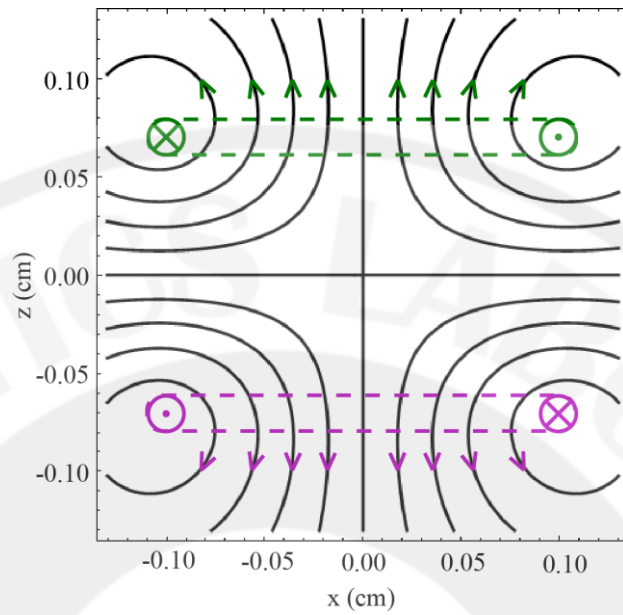


Figure 4.4: Shows the magnetic field computer simulated for the anti-Helmholtz configuration. Dash lines indicate position of coils. Dot and cross symbols represent the directions of current in the coils which provide the magnetic fields in the direction indicated by arrows.

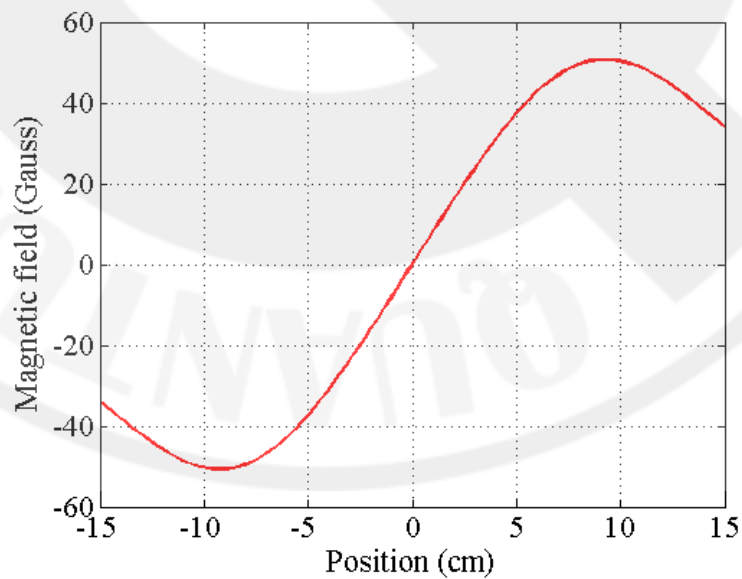


Figure 4.5: Magnetic field along z axis (see Figure 4.4).

#### 4.2.4 MOT Results and Discussions

In the first try of the TBT configuration (apply only two trapping beam and magnetic fields), we aligned all four straight rods by 45° degree from the vertical direction as seen in Figure 4.6 (left). The high NA lens and two 50 mm lenses were also placed obliquely along the rods. After we closed the chamber and turn on the vacuum system, we found a leakage at the flange joining the chamber to the pumps. To solve this, we balanced the chamber by adding small piece of aluminium foil at the chamber stands. At this point, the pressure inside the chamber reduced to a steady state at  $8 \times 10^{-9}$  torr. However, several movements of the chamber displaced every lens from the original locations. The two counter propagating cooling beams were not wholly intersected as shown in Figure 4.6 (right).



Figure 4.6: Shows the TBT setup. (left) Four straight rods and lenses were aligned by 45° degree from the vertical direction. (right) Small displacement of 50 mm lenses changed the direction of propagation of the laser beams and the beams were not completely overlapped.

We applied the magnetic field and then observed fluorescence. We moved the magnetic coils and observed blinking faint fluorescence which demonstrated the collection of an atomic cloud. The setup was not yet optimized to overcome the loss rate of atoms escaping from the trap, our first attempt did not allow observing the MOT.

We decided to open the chamber and aligned the straight rods in the horizontal direction as seen in Figure 4.7 (left). Until the pressure was reduced to  $\sim 10^{-8}$  torr, we applied the TBT and still could not detect the MOT. Therefore, we applied other two molasses beams to construct the FBT as shown in Figure 4.7 (right). The beam size was reduced by passing the beams through a diaphragm for convenience in beam alignments. In working condition, we removed the diaphragm and the beam diameter was approximately 1.7 cm. We applied the magnetic fields and observed fluorescence again. Formation of an atomic cloud being collected was also detected. Moving the magnetic coils correspondingly displaced the cloud but the loading rate was still not adequate to realize the MOT.

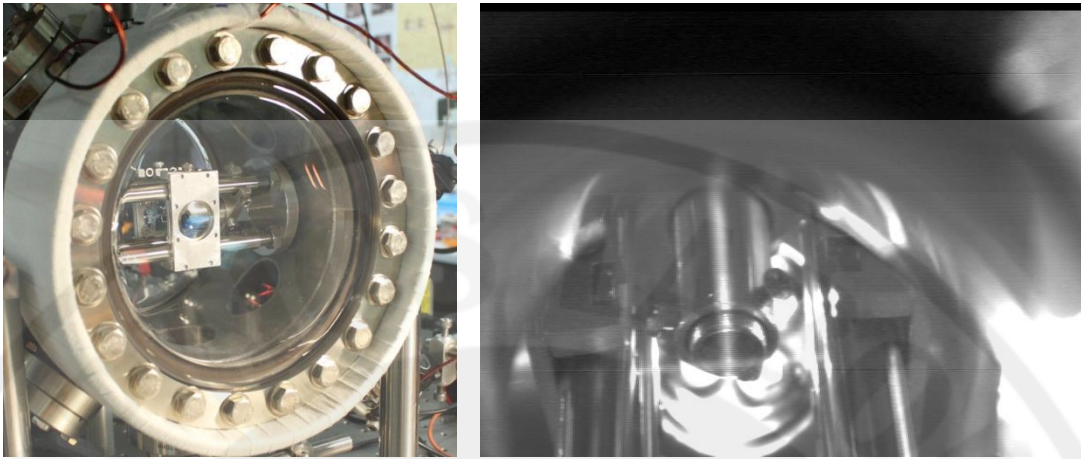


Figure 4.7: FBT setup. (left) The straight rods and lenses were aligned in the horizontal direction. (right) The cooling beams overlapped at the center of the chamber.

There are several reasons to explain why we could not detect the MOT in this experiment. The first reason is that the distance between the two 50 mm lenses was too long (35mm) comparing with the previous experiment in Ref. [8, 9] (25mm). This distance was restricted by the distance of the straight rods and could not be changed for our lens clampers. In this case, the overlapping region was reduced and only the small number of atoms was trapped. The second reason is that the zero magnetic field position was not located at the center of the chamber. Moving the magnetic coils by hand was a rough tuning and could not pinpoint the location of the field minima.

The possible solutions to improve the result contain:

- (1) Design a new lens mount instead of using the straight rods. We may construct a frame for mounting the 50 mm lenses and align them outside the chamber before put inside the chamber.

- (2) Construct a compensation coil (see Figure 4.8). This coil is larger than the quadrupole coils and locates near the chamber. Applying a DC current to this coil will finely adjust the location of the zero magnetic field along the coil axis.
- (3) Change the stainless chamber to a small glass cell. We can put all optical components outside the cell which are easier for alignments. This solution also allows us to optimize the distance between two 50 mm lenses.
- (4) Change the 50 mm lenses to the larger focal length lenses. This will enlarge the overlapping region which consequently increases the number of trapped atoms.

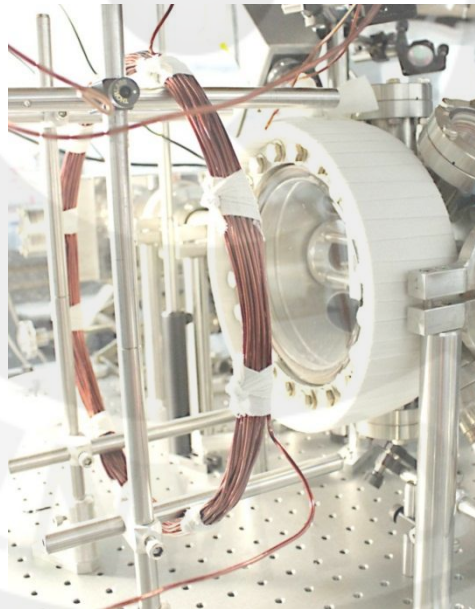


Figure 4.8: The compensation coil (bare coil) was placed near the chamber for fine adjusting the position of zero magnetic field.

### 4.3 Optical Dipole Trap

#### 4.3.1 Dipole Laser Beam Profiles

The dipole laser beam profile at the center of the MOT chamber could be demonstrated outside the chamber by applying this laser beams through an identical high NA lens (C240TME-B) as used inside the vacuum chamber. Pictures of the laser beam and a background were captured using a CCD camera (DCU223C) from Thorlabs. The result after the background subtraction process and the Gaussian fit of the laser intensity are shown in Figure 4.9 . By using the knife edge experiment, the beam waist and its divergence are  $4.7 \mu\text{m}$  and  $5.6 \times 10^{-2}$  rad, respectively.

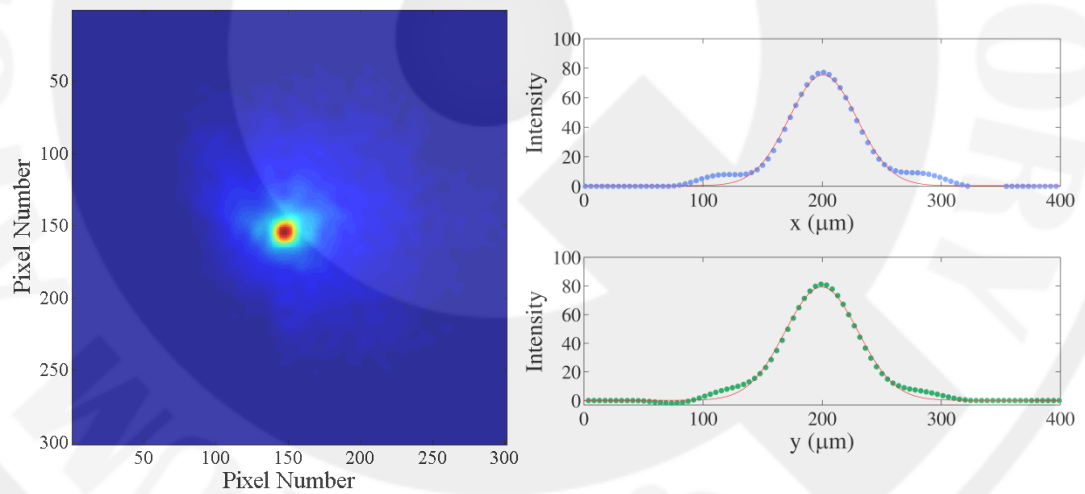


Figure 4.9: (left) The dipole laser beam profile after the background subtraction process. The maximum intensity is defined by deep red color. (right) Gaussian fit of the laser intensity in the x and y axis.

The dipole laser wavelength beam is shown in Figure 4.10.

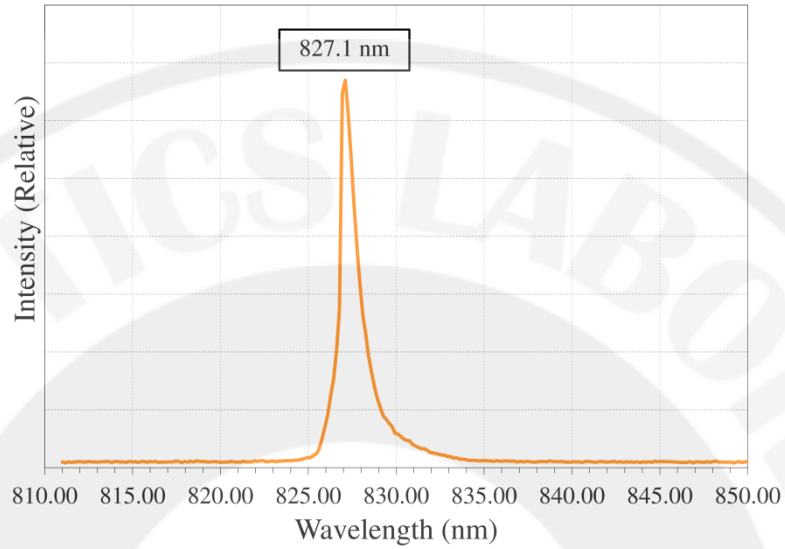


Figure 4.10: The dipole laser wavelength. The maximum intensity is at 827.1 nm.

### 4.3.2 Trap Depth Calculation

The measured variables from section 4.3.1 for the trap depth calculation of  $^{85}\text{Rb}$  are shown in Table 4.1. The calculated light shifts for the radial direction of the optical dipole trap can be seen in Figure 4.11. The programming code for this calculation obtained from A. Hilliard [18].

Table 4.1: The measured variables for the trap depth calculation of  $^{85}\text{Rb}$

Variables	Value
Power of the dipole laser	25.8 mW
Wavelength of the dipole laser	827.1 nm
Waist of the dipole laser	4.7 $\mu\text{m}$

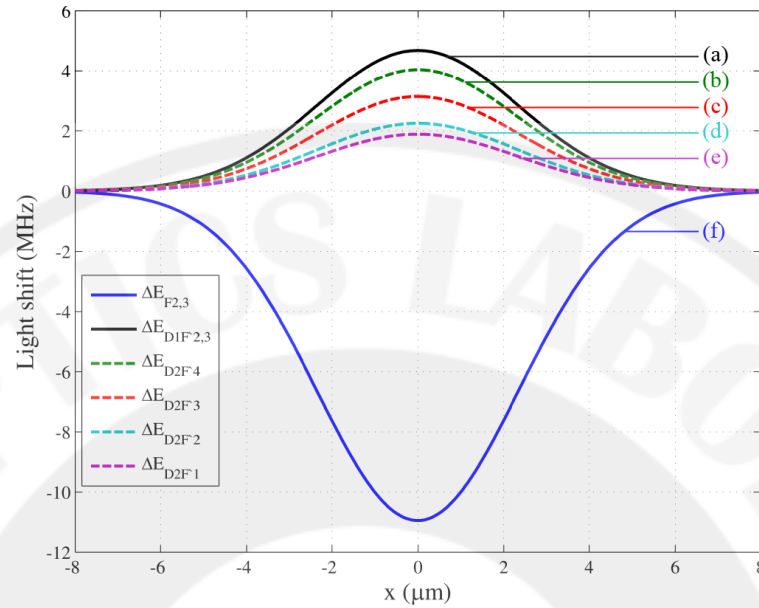


Figure 4.11: Light shifts of the energy levels of  $^{85}\text{Rb}$  in the dipole trap. The maximum shift of (a) the excited states  $5^2\text{P}_{1/2}$  (F=2 and F=3) were 4.68 MHz, indicated by a black solid line. (b) the excited state  $5^2\text{P}_{3/2}$  (F=4) was 4.03 MHz, indicated by a green dash line. (c) the excited state  $5^2\text{P}_{3/2}$  (F=3) was 3.14 MHz, indicated by a red dash line. (d) the excited state  $5^2\text{P}_{3/2}$  (F=2) was 2.24 MHz, indicated by a cyan dash line. (e) the excited state  $5^2\text{P}_{3/2}$  (F=1) was 1.88 MHz, indicated by a violet dash line. (f) the ground states  $5^2\text{S}_{1/2}$  (F=2 and F=3) were 10.95 MHz, indicated by a blue solid line.

### 4.3.3 Optical Dipole Trap Results and Discussions

In section 4.3.1 the beam profile in x and y axes were not equal and cause the difference trap width in each radial direction. Cleaning this beam using suggestions in section 4.2.4 would be help improving the beam profile.

In section 4.3.2 the dipole trap depth is very small (10.95 MHz) comparing with one in Ref. [14] (102 MHz). This is because the dipole laser power is low and the

beam waist is large. In this case, an atom in the bottom of the trap require at least  $h \times 10.95$  MHz of kinetic energy, which is very small, to escape the trap. To improve the trap depth, we may use a higher power laser diode.

The loading of the optical dipole trap in the chamber could not be constructed because we could not detect the MOT. The dipole trap may be directly loaded with cold atomic cloud (without manifest MOT), however it requires a high quality EMCCD camera to observe few hundreds of rubidium atoms.

#### **4.4 Light Assisted Collisions**

##### **4.4.1 LAC and Repump Laser Beams Profiles**

The LAC and repump laser beams profiles at the center of the science chamber could be demonstrated outside the chamber by applying these laser beams through the 100 mm lens (the same lens used for the LAC experiment). Pictures of the laser beams and a background (all laser beams turned off) were captured using a CCD camera (DCU223C) from Thorlabs. Pictures of the LAC beam and the repump beam after the background subtraction process are shown in Figure 4.12.

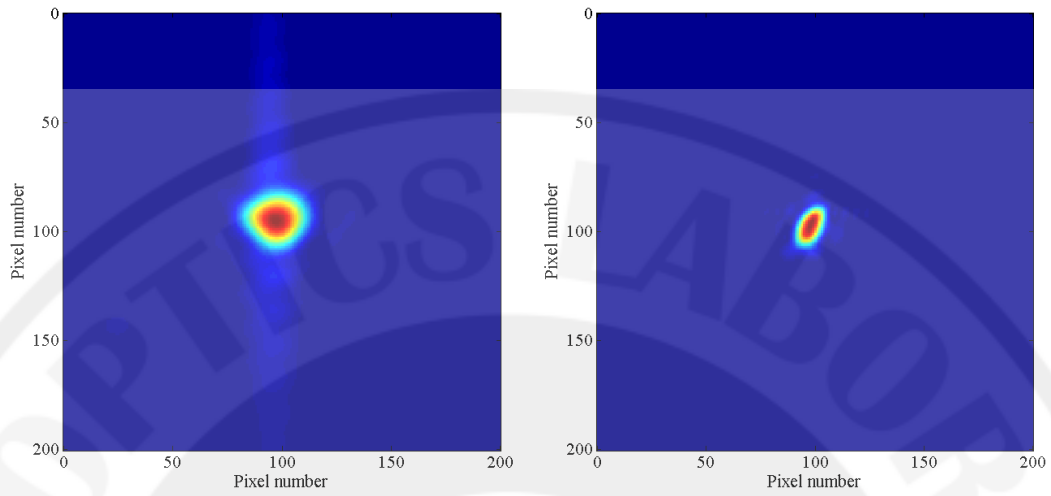


Figure 4.12: LAC and repump laser beam profiles after the background subtraction. The maximum intensity is defined by a deep red color. (left) The LAC laser beam profile. (right) The repump laser beam profile.

#### 4.4.2 Doppler-free Saturated Absorption Spectroscopy

By observing the DSAS from our homemade lasers, the absorption profile of  $^{85}\text{Rb}$  and  $^{87}\text{Rb}$  is shown in Figure 4.13. We locked the LAC beam at the D1 line, ( $F=2 \rightarrow F'=3$ ), and the repump beam at the D1 line, ( $F=3 \rightarrow F'=3$ ), as shown in Figure 4.14.

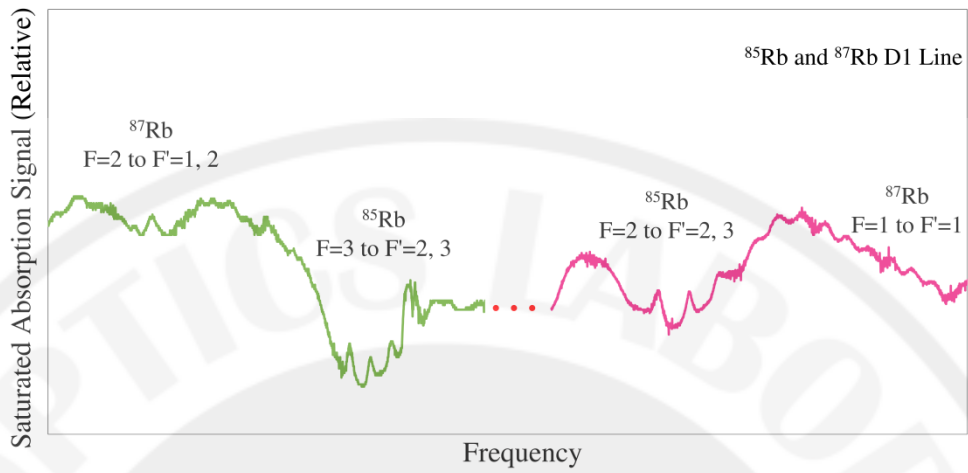


Figure 4.13: Saturated absorption signal for D1 line transition of  $^{85}\text{Rb}$  and  $^{87}\text{Rb}$ .

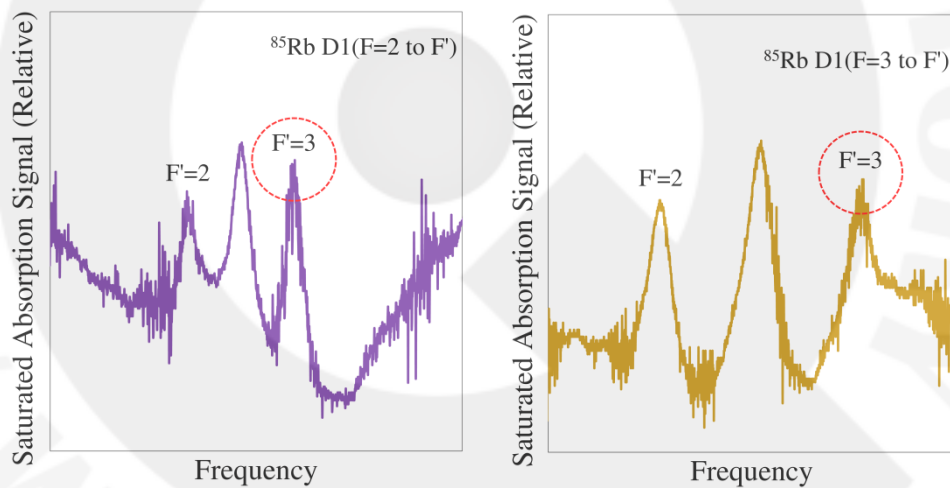


Figure 4.14: Saturated absorption signal for (left)  $F=2$  to  $F'$  transition. The dashed circle indicates the frequency of the LAC beam, which was locked at ( $F=2 \rightarrow F'=3$ ) transition. (right)  $F=3$  to  $F'$  transition. The dashed circle indicates the frequency of the repump beam, which was locked at ( $F=3 \rightarrow F'=3$ ) transition.

### 4.4.3 Light Assisted Collisions Results and Discussions

In section 4.4.1 the laser beams profiles were different for two different sources. The suggestions to improve the profiles are stated in section 4.2.4

In section 4.4.2 the absorption spectroscopy signals were fairly difficult to measure because the laser diode provides a very long range frequency (760 nm to 860 nm) and several laser modes were emitted at the same time. By tuning the laser current, laser temperature, and the external cavity, we observed the absorption spectroscopy signals as shown in Figure 4.13 and Figure 4.14. Now, we have an ability to lock the LAC beams at the specific frequency. However, not before can we load the dipole trap, the LAC experiment may progress.

## CHAPTER 5

### CONCLUSIONS AND FUTURE PLANS

#### 5.1 Conclusions

In the experiment, we constructed a system for preparing a small number of  $^{85}\text{Rb}$  atoms in a far off-resonance optical dipole trap. A total number of five highly-stable diode laser systems were built. Specifically, these lasers are designated to (1) MOT trapping, (2) MOT repumping, (3) LAC at D1 line, (4) LAC repumping and (5) dipole trapping. The spatial mode structures of all the lasers at the interaction plane, which define the interaction region uniquely, were characterized by a CCD camera. The saturated absorption spectroscopy for all the lasers, except for the last one, was studied.

In order to prepare the MOT, the cooling laser and the repumping laser were locked at  $\text{D2}(F=3 \rightarrow F'=4)$  transition and  $\text{D2}(F=2 \rightarrow F'=3)$  transition, respectively. Two magnetic coils were constructed and the value of the magnetic field from these coils, positioned in the anti-Helmholtz configuration, was in agreement with a computer simulation. A high-vacuum system and rubidium dispensers were prepared to support the overall experiments. We observed atomic rubidium being collected to form a faint atomic cloud that filled in the MOT overlapping region at the center of the chamber. The cloud was forced to move in correspondence with detuning of the cooling laser beams and the position of the field minima in the MOT experiment.

Without frequency locking, the optical dipole trap operated stably around the wavelength of 827 nm with a well-defined trap depth of  $h \times 10.95$  MHz and trap width of 4.7  $\mu\text{m}$ . At this wavelength, the variation of  $\pm 0.5$  nm contributes to approximately 2% change in the trap depth. The LAC laser and the LAC repumping laser respectively centering at  $D1(F=2 \rightarrow F'=3)$  transition and  $D1(F=3 \rightarrow F'=3)$  transition, were successfully assembled and readily led up to the study of the dynamics of cold collision.

## 5.2 Future Plan

The basic system for trapping small number of cold atoms in the optical dipole trap was prepared in this research. The components therein are important for producing an ensemble of cold atoms, which can be used in various experiment related to atomic, molecular and optical physics. Particularly, it could provide a single atom source, which plays an important role in a neutral atom based quantum logic devices and quantum memory. This preliminary work provides comprehensive assemblage that would allow efficiently trapping single rubidium atom in the near future.

## REFERENCES

1. T. Gr̃unzweig, et al., *Near-deterministic preparation of a single atom in an optical microtrap*. Nature Phys., 2010. **6**.
2. D. Hoffmann, S. Bali, and T. Walker, *Trap-depth measurements using ultracold collisions*. Phys. Rev. A, 1996. **54**(2).
3. Harold J. Metcalf and P. van der Straten, *Laser Cooling and Trapping* 1999: Springer.
4. Phillips, W.D., *Nobel Lecture: Laser cooling and trapping of neutral atoms*. Reviews of Modern Physics, 1998. **70**(3): p. 721-741.
5. Chu, S., et al., *Three-dimensional viscous confinement and cooling of atoms by resonance radiation pressure*. Physical Review Letters, 1985. **55**(1): p. 48-51.
6. Dalibard, J. and C. Cohen-Tannoudji, *Laser cooling below the Doppler limit by polarization gradients: simple theoretical models*. J. Opt. Soc. Am. B, 1989. **6**(11): p. 2023-2045.
7. Raab, E.L., et al., *Trapping of Neutral Sodium Atoms with Radiation Pressure*. Physical Review Letters, 1987. **59**(23): p. 2631-2634.
8. Tabosa, J.R., S.S. Vianna, and C.A. Benevides, *Loading mechanism in a two-beam magneto-optical trap*. Optics Communications, 1995. **116**(1-3): p. 77-80.
9. Chesman, C., et al., *Two- and four-beam magneto-optical trapping of neutral atoms*. Opt. Lett., 1994. **19**(16): p. 1237-1239.

10. Grimm, R., M. Weidemüller, and Y.B. Ovchinnikov, *Optical Dipole Traps for Neutral Atoms*, in *Advances In Atomic, Molecular, and Optical Physics*, B. Benjamin and W. Herbert, Editors. 2000, Academic Press. p. 95-170.
11. Nieminen, T.A., *Optical manipulation: Trapping ions*. Nature Photon., 2010. **4**: p. 737-738.
12. Dalibard, J. and C. Cohen-Tannoudji, *Dressed-atom approach to atomic motion in laser light: the dipole force revisited*. J. Opt. Soc. Am. B, 1985. **2**(11): p. 1707-1720.
13. Schulz, M., *Tightly confined atoms in optical dipole traps*. Ph.D. thesis, University of Innsbruck, 2002.
14. McGovern, M., *Isolating and Manipulating Single Atoms*. Ph.D. thesis, University of Otago, 2011.
15. Daniel A. Steck, "*Rubidium 85 D line Data*". available online at <http://steck.us/alkalidata> (revision 2.1.4, 23 December 2010).
16. C. J. Hawthorn, K.P. Weber, and R.E. Scholten, *Littrow configuration tunable external cavity diode laser with fixed direction output beam*. Rev. Sci. Instrum., 2001. **72**(12): p. 4477-4479.
17. Macadam, K.B., A. Steinback, and C. Wieman, *A narrow-band tunable diode laser system with grating feedback, and a saturated absorption spectrometer for Cs and Rb*. Am. J. Phys., 1992. **60**(12): p. 1098-1111.
18. This programming code is obtained from a private communication with A. Hilliard via the collaboration with the Jack Dodd Centre (JDC) for Quantum Technology, University of Otago.
19. Optics Group, School of Physics, the University of Melbourne, Diode laser electronics for atom optics: <http://optics.ph.unimelb.edu.au/atomopt/electronics/index.html>.
20. Horowitz, P., *The art of electronics / Paul Horowitz*, Winfield Hill, ed. W. Hill 1989, Cambridge [England] :: Cambridge University Press.

21. Scholten, R.E., *Enhanced laser shutter using a hard disk drive rotary voice-coil actuator*. Review of Scientific Instruments, 2007. **78**(2): p. 026101-026101-2.
22. Optics Group, School of Physics, the University of Melbourne, Engineering drawing: <http://optics.ph.unimelb.edu.au/atomopt/diodes.html>.
23. The drawing of C240TME-B from Thorlabs website: <http://www.thorlabs.com/Thorcat/13700/13707-E0W.pdf>.
24. "Magnetic Field of a Current Loop" from the Wolfram Demonstrations Project <http://demonstrations.wolfram.com/MagneticFieldOfACurrentLoop/>  
Contributed by: S. M. Blinder.



**APPENDICES**

## APPENDIX A

### RUBIDIUM-85 DATA

#### A.1 Introduction

This chapter includes the properties of Rubidium-85 used in this thesis. The energy levels and transition properties are reproduced from Daniel Steck [15].

#### A.2 Rubidium-85 Energy Level

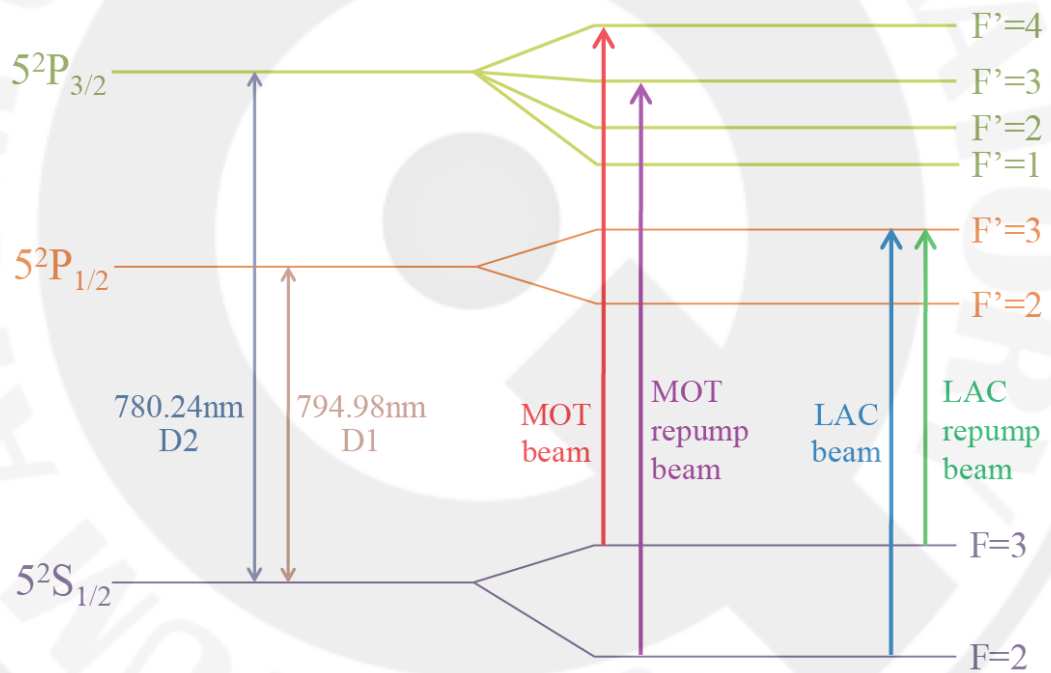


Figure A.1: Energy levels of  $^{85}\text{Rb}$  (not to scale). The MOT beam, MOT repump beam, LAC beam, and LAC repump beam are indicated by the arrows.

Table A.1: Fundamental physical constants

Speed of light	$c$	$2.997\,924\,58 \times 10^8$ m/s
Permittivity of vacuum	$\epsilon_0$	$8.854\,187\,817 \dots \times 10^{-12}$ F/m
Planck's constant	$h$	$6.626\,068\,96(33) \times 10^{-34}$ J·s
Reduced Planck's constant	$\hbar$	$1.054\,571\,628(53) \times 10^{-34}$ J·s
Elementary charge	$e$	$1.602\,176\,487(40) \times 10^{-19}$ C
Boltzmann's constant	$k_B$	$1.380\,6504(24) \times 10^{-23}$ J/K

Table A.2:  $^{85}\text{Rb}$  physical properties.

Atomic Number	$Z$	37
Total Nucleons	$Z + N$	85
Atomic Mass	$m$	$1.409\,993\,199(70) \times 10^{-25}$ kg
Nuclear Spin	$I_N$	5/2

Table A.3:  $^{85}\text{Rb}$  D2( $5^2\text{S}_{1/2} \rightarrow 5^2\text{P}_{3/2}$ ) transition optical properties.

Frequency	$\omega_0$	$2\pi \times 384.230406373(14)$ THz
Wavelength (Vacuum)	$\lambda$	780.241368271(27) nm
Lifetime	$\tau$	26.2348(77) ns
Decay Rate/ Natural Line Width (FWHM)	$\Gamma$	$2\pi \times 6.0666(18)$ MHz
Doppler Temperature	$T_D$	145.57 $\mu\text{K}$

Table A.4:  $^{85}\text{Rb}$  D1( $5^2\text{S}_{1/2} \rightarrow 5^2\text{P}_{1/2}$ ) transition optical properties.

Frequency	$\omega_0$	$2\pi \times 377.107385690(46)$ THz
Wavelength (Vacuum)	$\lambda$	794.979014933(96) nm
Lifetime	$\tau$	27.679(27) ns
Decay Rate/ Natural Line Width (FWHM)	$\Gamma$	$2\pi \times 5.7500(56)$ MHz

Table A.5:  $^{85}\text{Rb}$  reduced matrix elements

D2( $5^2\text{S}_{1/2} \rightarrow 5^2\text{P}_{3/2}$ ) Transition dipole matrix elements	$\langle J=1/2 \  \mathbf{d} \  J'=3/2 \rangle$	$3.58425(74) \times 10^{29} \text{ Cm}$
D1( $5^2\text{S}_{1/2} \rightarrow 5^2\text{P}_{1/2}$ ) Transition dipole matrix elements	$\langle J=1/2 \  \mathbf{d} \  J'=3/2 \rangle$	$2.5377(17) \times 10^{29} \text{ Cm}$

Table A.6:  $^{85}\text{Rb}$  dipole matrix elements for the D2  $\pi$  transitions

( $F=3, m_F \rightarrow F', m'_F = m_F$ ) expressed as multiples of  $\langle J=1/2 \| \mathbf{d} \| J'=3/2 \rangle$ .

	$m_F = -3$	$m_F = -2$	$m_F = -1$	$m_F = 0$	$m_F = 1$	$m_F = 2$	$m_F = 3$
$F'=4$	$-\sqrt{\frac{1}{8}}$	$-\sqrt{\frac{3}{14}}$	$-\sqrt{\frac{15}{56}}$	$-\sqrt{\frac{2}{7}}$	$-\sqrt{\frac{15}{56}}$	$-\sqrt{\frac{3}{14}}$	$-\sqrt{\frac{1}{8}}$
$F'=3$	$-\sqrt{\frac{5}{24}}$	$-\sqrt{\frac{5}{54}}$	$-\sqrt{\frac{5}{216}}$	0	$\sqrt{\frac{5}{216}}$	$\sqrt{\frac{5}{54}}$	$\sqrt{\frac{5}{24}}$
$F'=2$		$\sqrt{\frac{5}{189}}$	$\sqrt{\frac{5}{189}}$	$\sqrt{\frac{1}{21}}$	$\sqrt{\frac{5}{189}}$	$\sqrt{\frac{5}{189}}$	

Table A.7:  $^{85}\text{Rb}$  dipole matrix elements for the D2  $\pi$  transitions

( $F=2, m_F \rightarrow F', m'_F = m_F$ ) expressed as multiples of  $\langle J=1/2 \| \mathbf{d} \| J'=3/2 \rangle$ .

	$m_F = -2$	$m_F = -1$	$m_F = 0$	$m_F = 1$	$m_F = 2$
$F'=3$	$-\sqrt{\frac{2}{27}}$	$-\sqrt{\frac{16}{135}}$	$-\sqrt{\frac{2}{15}}$	$-\sqrt{\frac{16}{135}}$	$-\sqrt{\frac{2}{27}}$
$F'=2$	$-\sqrt{\frac{7}{27}}$	$-\sqrt{\frac{7}{108}}$	0	$\sqrt{\frac{7}{108}}$	$\sqrt{\frac{7}{27}}$
$F'=1$		$\sqrt{\frac{3}{20}}$	$\sqrt{\frac{1}{5}}$	$\sqrt{\frac{3}{20}}$	

Table A.8:  $^{85}\text{Rb}$  dipole matrix elements for the D1  $\pi$  transitions

( $F=3, m_F \rightarrow F', m'_F = m_F$ ) expressed as multiples of  $\langle J=1/2 \| \mathbf{d} \| J'=1/2 \rangle$ .

	$m_F = -3$	$m_F = -2$	$m_F = -1$	$m_F = 0$	$m_F = 1$	$m_F = 2$	$m_F = 3$
$F'=3$	$-\sqrt{\frac{1}{3}}$	$-\sqrt{\frac{4}{27}}$	$-\sqrt{\frac{1}{27}}$	0	$\sqrt{\frac{1}{27}}$	$\sqrt{\frac{4}{27}}$	$\sqrt{\frac{1}{3}}$
$F'=2$		$\sqrt{\frac{5}{27}}$	$\sqrt{\frac{8}{27}}$	$\sqrt{\frac{1}{3}}$	$\sqrt{\frac{8}{27}}$	$\sqrt{\frac{5}{27}}$	

Table A.9:  $^{85}\text{Rb}$  dipole matrix elements for the D1  $\pi$  transitions

( $F=2, m_F \rightarrow F', m'_F = m_F$ ) expressed as multiples of  $\langle J=1/2 \| \mathbf{d} \| J'=1/2 \rangle$ .

	$m_F = -2$	$m_F = -1$	$m_F = 0$	$m_F = 1$	$m_F = 2$
$F'=3$	$\sqrt{\frac{5}{27}}$	$\sqrt{\frac{8}{27}}$	$\sqrt{\frac{1}{3}}$	$\sqrt{\frac{8}{27}}$	$\sqrt{\frac{5}{27}}$
$F'=2$	$\sqrt{\frac{4}{27}}$	$\sqrt{\frac{1}{27}}$	0	$-\sqrt{\frac{1}{27}}$	$-\sqrt{\frac{4}{27}}$

## **APPENDIX B**

### **CIRCUIT DIAGRAM**

#### **B.1 Introduction**

In this chapter, we presented PCB layouts and schematic diagrams of (1) a laser driver, (2) a temperature controller, (3) a triangular wave generator and (4) a servolock circuit. These circuits were mainly reproduced from Ref. [17] and employed to drive and stabilize four laser systems. Along with these laser systems, we presented and described laser shutters, their driver circuits and a homemade digital delay generator (hDDG) that were employed to orchestrate the gating time (on/off) of all LAC processes (see section 3.6.2) and the detection system. At the heart of the hDDG, there rested a piece of a PIC Microcontroller that generates TTL pulses for all time gating sequences.

We improved the circuits from Ref. [17] by adding several test points made of brass eyelets for a convenience of circuit testing. A 0.1 $\mu$ F/50V ceramic capacitor was attached to each input pins of every IC to avoid voltage dips that could affect operations or damage circuits. The power supply for each circuit came from a homemade +/-15 power supply and a 0-30 V 3A regulator (FK809) from Future kit. The latter was applied to a piezo disc in order to tune the length of the external cavity of some lasers (see section 3.2).

Most electronics components were ordered from Electronics Source <http://www.es.co.th/> and Element14 <http://th.element14.com/>. The first company

offers general components with low prices while the second company provides specific and rare components with higher rates.

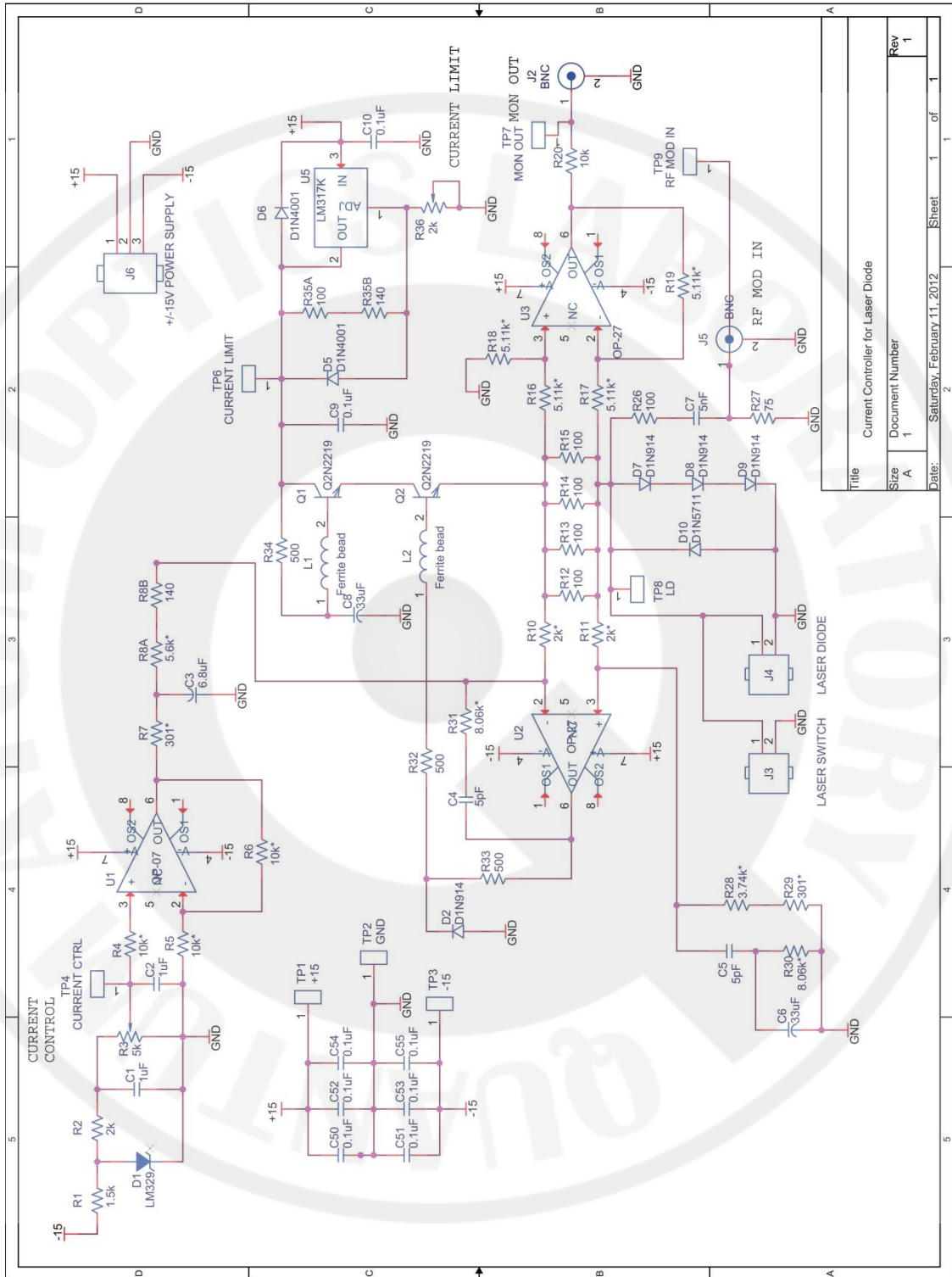
## **B.2 Laser Driver**

A laser driver is an important device designed to avoid any electrical transient that can damage the laser. A good laser driver should provide low current noise, excellent dc stability, and a capacity for high-speed modulation.

The laser drivers in our laboratory were reproduced from both Wieman's circuit and Melbourne's circuit. The circuit from Wieman [17] is not too complicated and works well. However, some parts were obsoleted and we need to replace them by alternative ones, e.g., LM399 and OP05 were substituted by LM329 and OP07, respectively. Even though the circuit from the University of Melbourne [19] is intricate, it offers additional protections and indicators. In this circuit, some components were quite expensive as compared to Wieman's circuit.

In this research, four laser drivers were reproduced from Wieman. An assembly top and a PCB layout are shown in Figure B.1 and Figure B.2. A schematic diagram of the circuit is shown in Figure B.3.





Title		Current Controller for Laser Diode	
Size	A	Document Number	1
Date:	Saturday, February 11, 2012	Sheet	1 of 1
Rev	1		

Figure B.3: Schematic diagram of a laser driver circuit

### B.3 Temperature Controller

A temperature controller is essential for the long term operation with a precise output frequency. The circuit was reproduced from Wieman with minor modification, i.e., a series of  $4.99\text{k}\Omega$  resistors were replaced with a  $50\text{k}\Omega$  variable resistor and the obsolete 2N6657 was replaced with IRF820 or IRF830.

In our controller, an 85 W thermoelectric cooler (TEC1-12710) from HB together with a block of aluminium heatsink were used to stabilize a laser diode temperature. Two  $50\text{k}\Omega$  thermistors (07C5002JF) from VISHAY were located near a collimation tube. One thermistor was used with the temperature controller circuit and another directly with the electric thermometer. An assembly top and a PCB layout are shown in Figure B.4 and Figure B.5. A schematic diagram of the circuit is shown in Figure B.6.

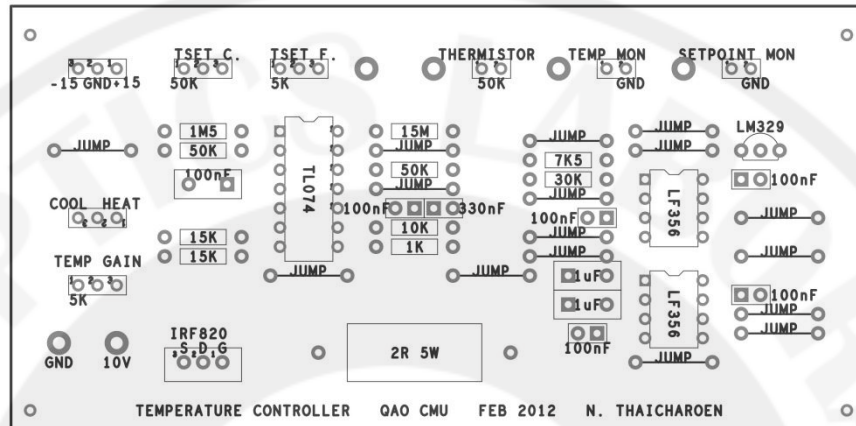


Figure B.4: PCB assembly top of a temperature controller circuit

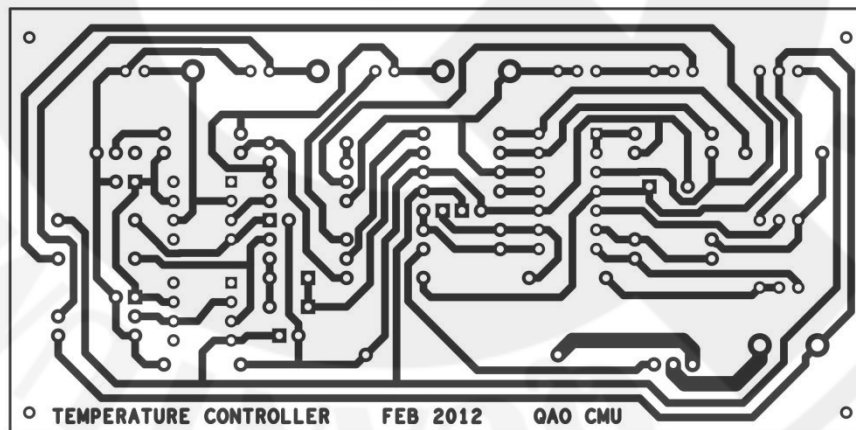


Figure B.5: PCB layout of a temperature controller circuit

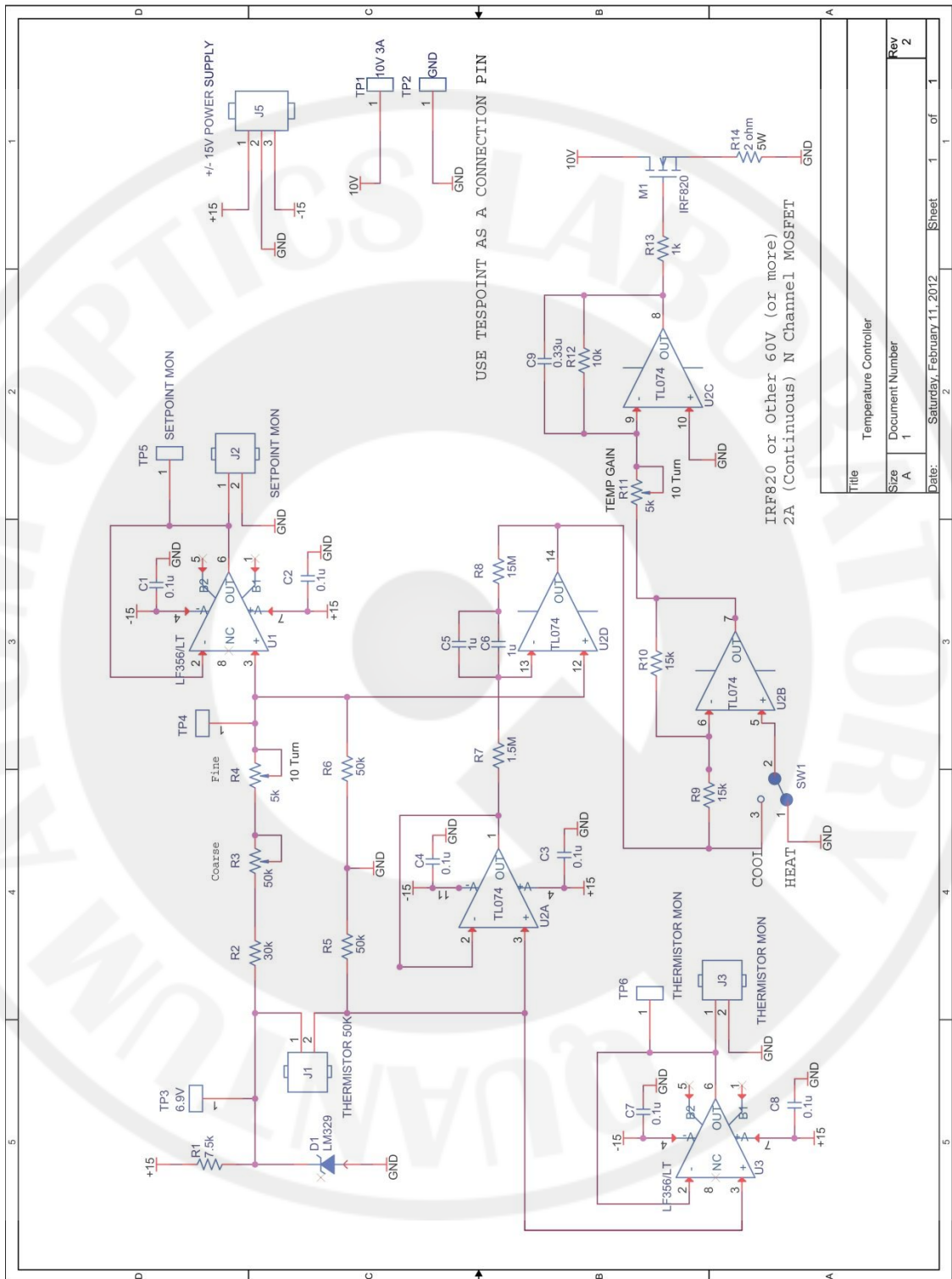


Figure B.6: Schematic diagram of a temperature controller circuit

Title	Temperature Controller
Size	A
Document Number	1
Rev	2
Date	Saturday, February 11, 2012
Sheet	1 of 1

### B.4 Triangular Wave Generator

A triangular wave generator is used to provide a voltage ramp to a servolock circuit. The circuit for the generator is easily obtained from several fundamental electronics books such as in [20]. An assembly top and a PCB layout are shown in Figure B.7 and Figure B.8. A schematic diagram of the circuit is shown in Figure B.9.

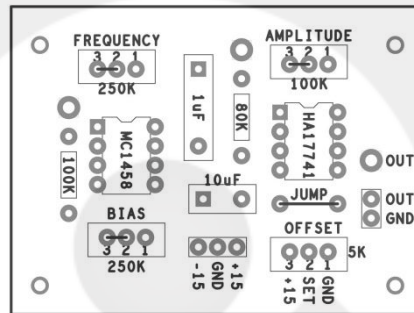


Figure B.7: PCB assembly top of a triangular wave generator circuit

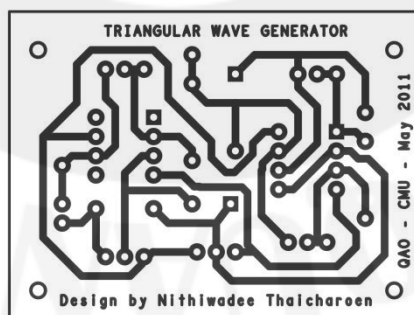
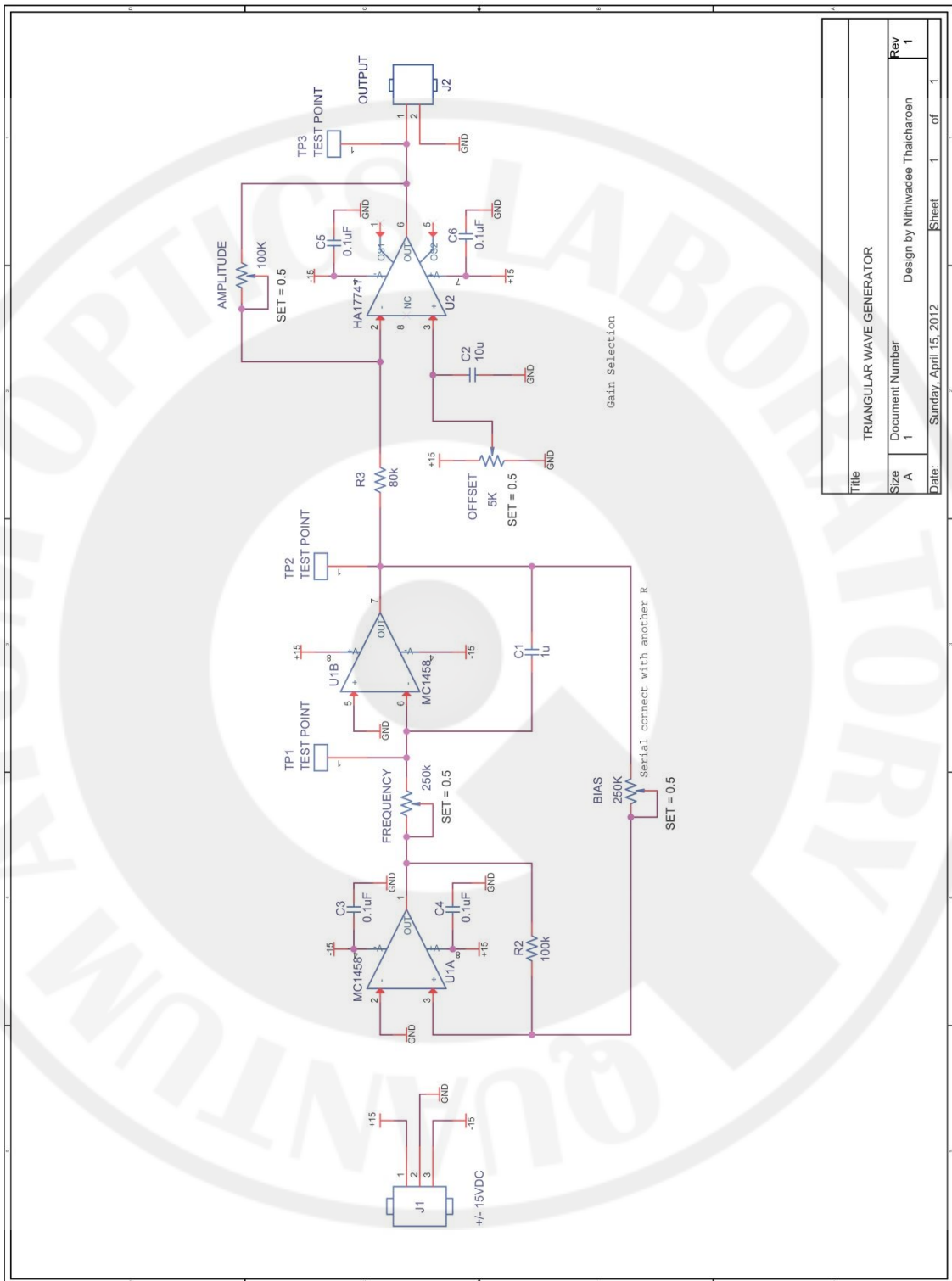


Figure B.8: PCB layout of a triangular wave generator circuit



Title	TRIANGULAR WAVE GENERATOR		
Size	Document Number	Design by	Rev
A	1	Nithiwadee Thacharoen	1
Date:	Sunday, April 15, 2012	Sheet	1 of 1

Figure B.9: Schematic diagram of a triangular wave generator circuit

## B.5 Servolock

The servolock was based on Wieman and JILA circuits. The input signals came from two photodiodes (SFH213) from OSRAM which received photons from SAS. When we scanned a piezo disc using a ramp from the triangular wave generator, the differential signal provided the dips that indicated each hyperfine transition of Rb atoms. We could lock the laser at a specific frequency by reducing the ramp and tuning a set point. An assembly top and a PCB layout are shown in Figure B.10 and Figure B.11. A schematic diagram of the circuit is shown in Figure B.12.

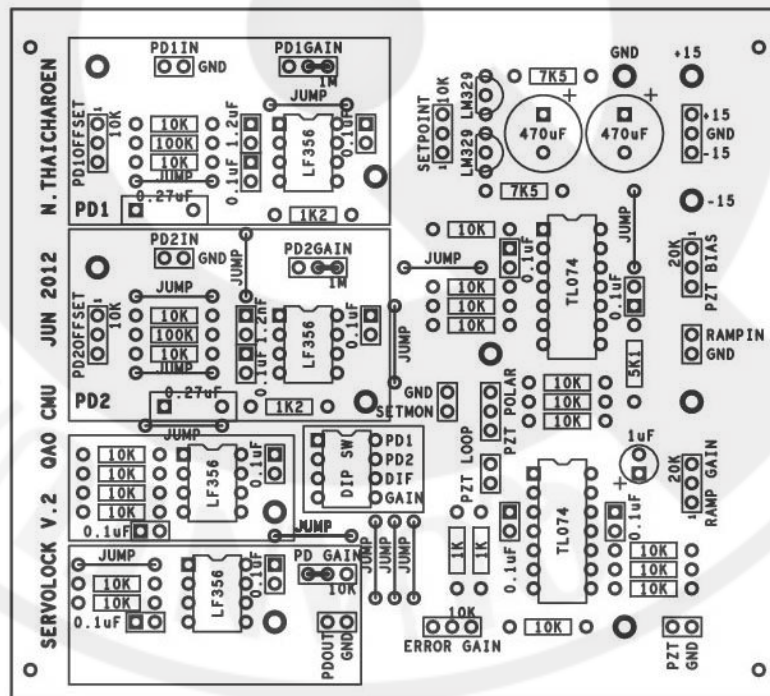


Figure B.10: PCB assembly top of a servolock circuit

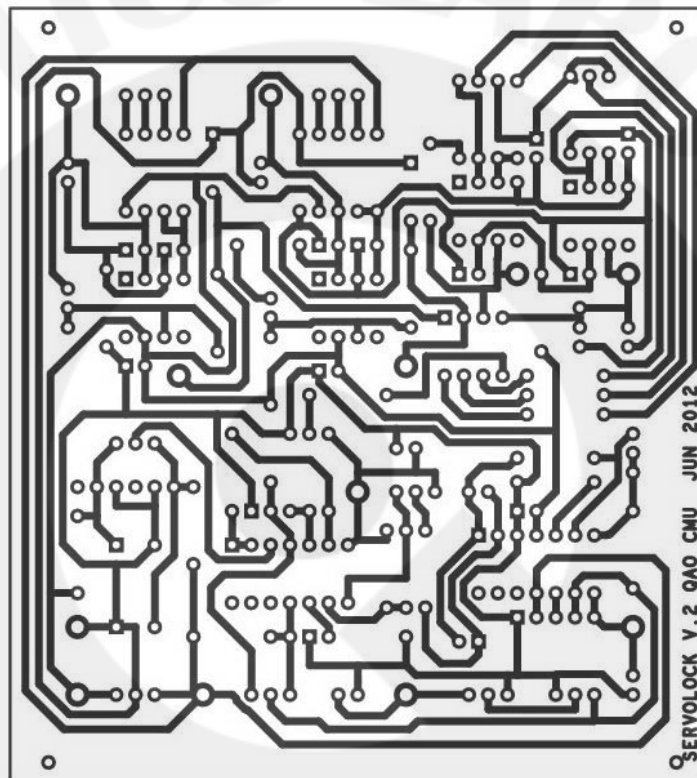


Figure B.11: PCB layout of a servolock circuit

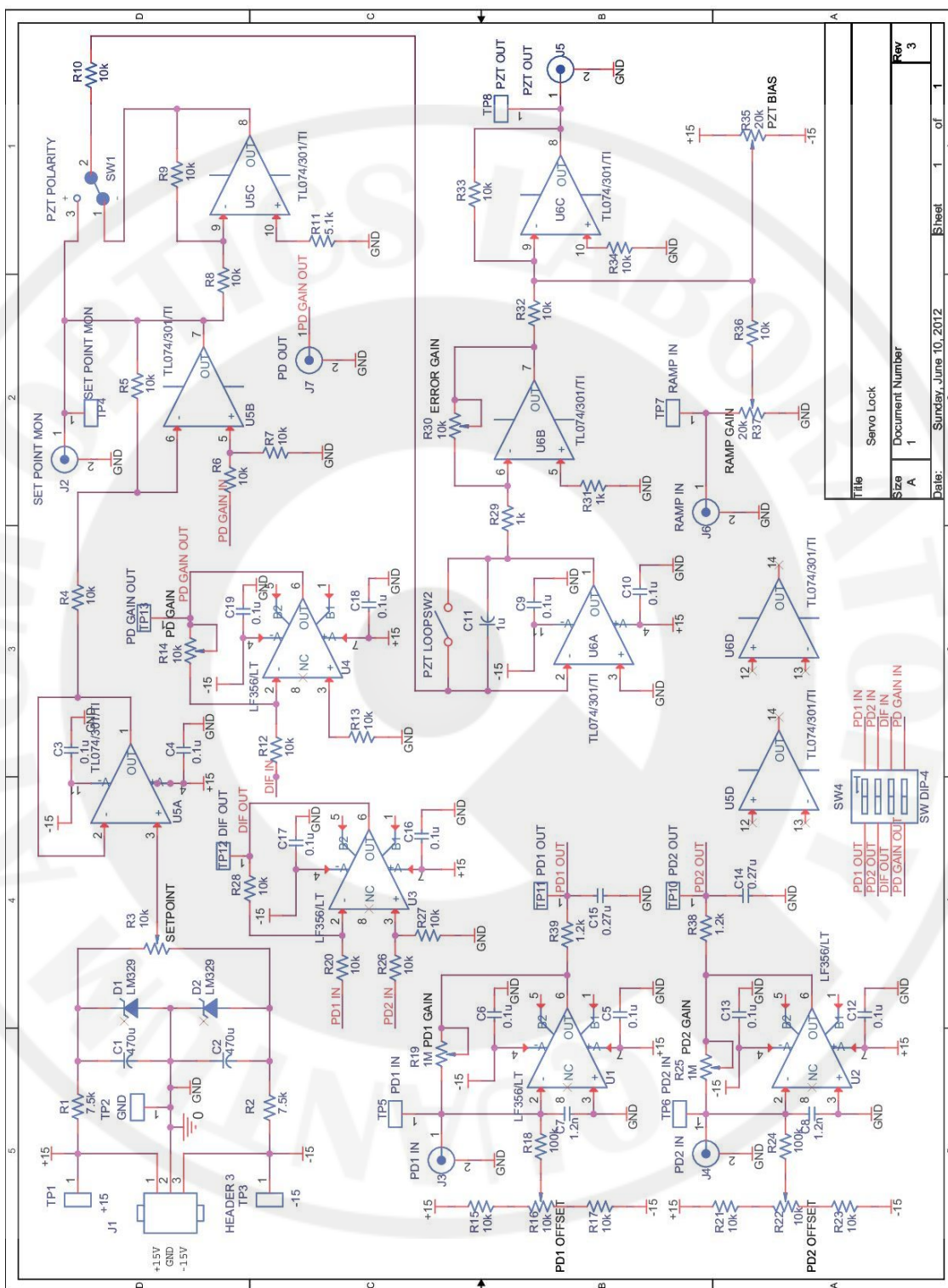


Figure B.12: Schematic diagram of a servolock circuit

## B.6 Fast Shutter Driver

The fast shutter driver was reproduced from Ref. [21]. This circuit was used to control the position of a pivot arm in a hard disk. The up and down directions of the pivot arm referred to open and close the shutter. Schematic diagrams of PCB and electrical circuit are shown, respectively.

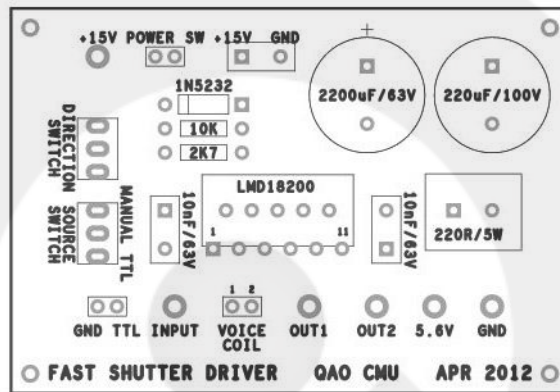


Figure B.13: PCB assembly top of a fast shutter driver circuit

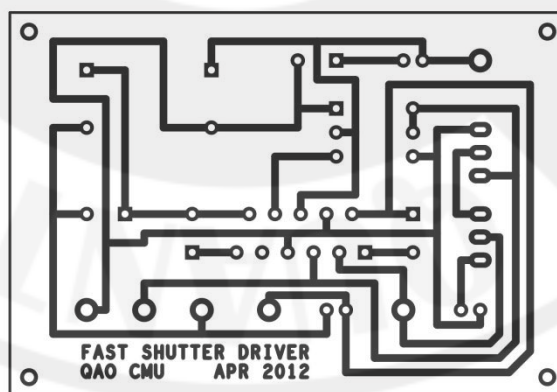
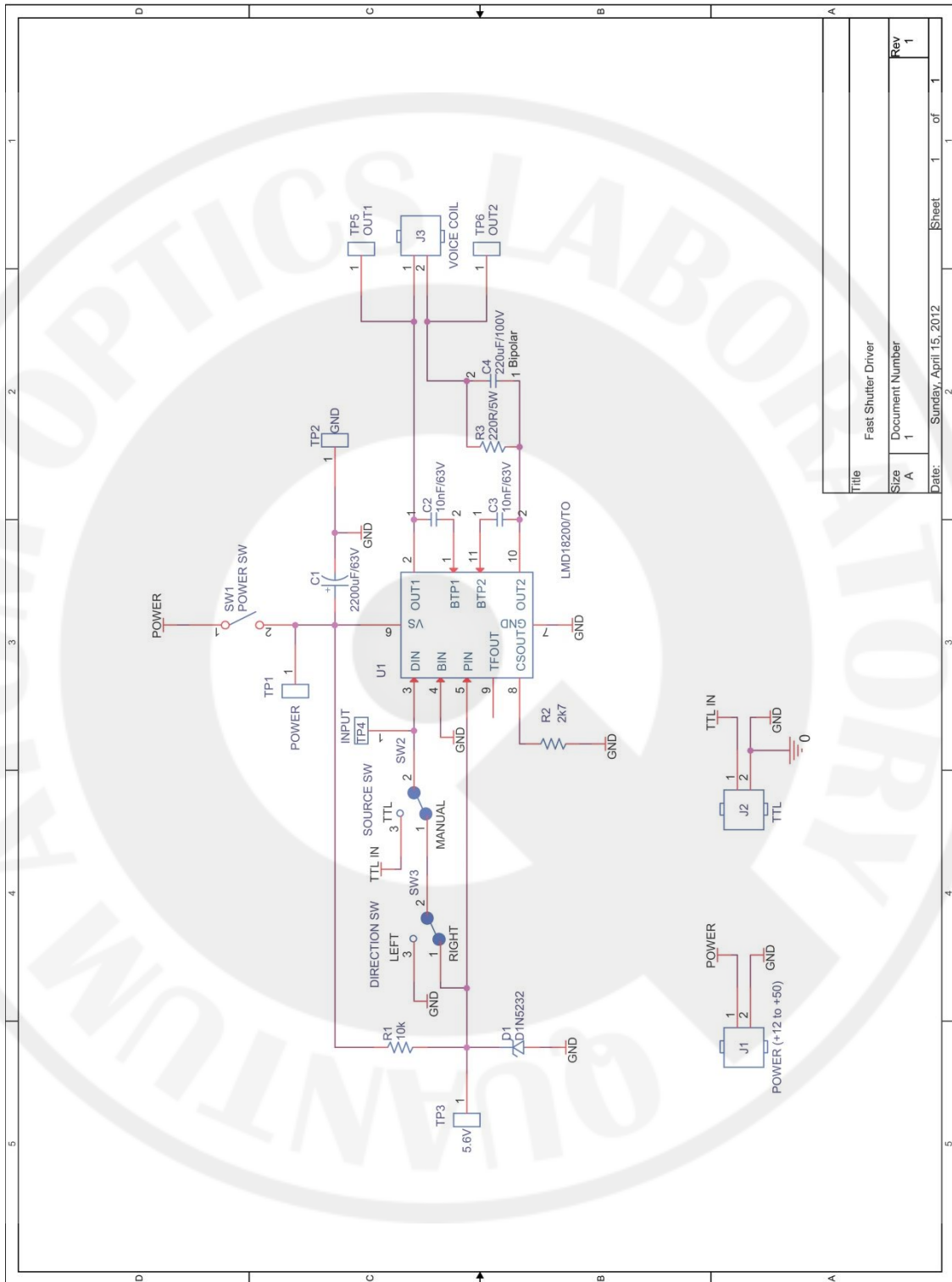


Figure B.14: PCB layout of a fast shutter driver circuit



Title		Fast Shutter Driver
Size	Document Number	A 1
Rev		1
Date:	Sunday, April 15, 2012	
Sheet	1	of 1

Figure B.15: Schematic diagram of a fast shutter driver circuit

## APPENDIX C

### MECHANICAL DRAWING

#### C.1 Laser Base Plate and Laser Box

A laser base-plate design is mostly reproduced from the optics group at University of Melbourne [22]. The plates are made of aluminium. The mechanical drawings of the laser base plates are shown in the figures from Figure C.1 to Figure C.6. The base plate in Figure C.1 was attached to a kinematic mount for a laser diode. The plate is attached to another base plate in Figure C.2 using four M4 plastic bolts to insulate electrical noises. The plate in Figure C.2 was then attached to an aluminium heat sink in Figure C.3 in order to dissipate heat away from the laser diode.

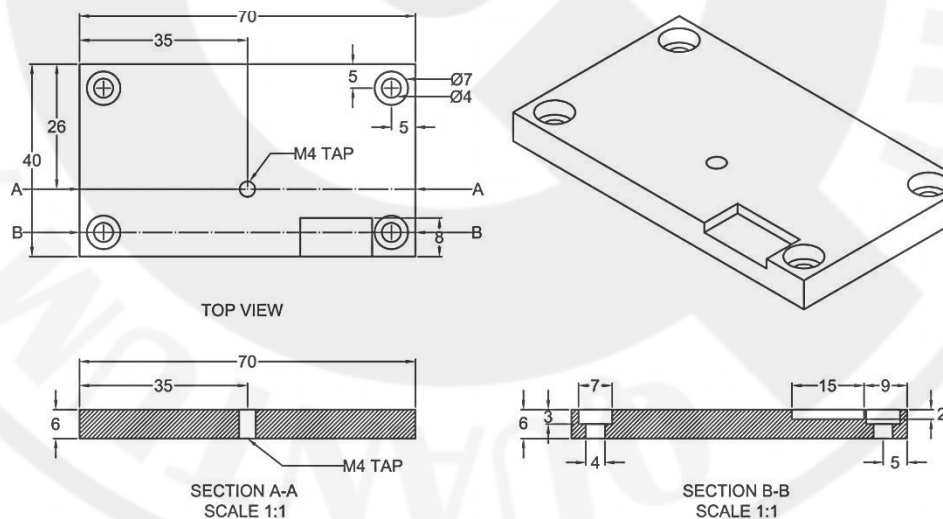


Figure C.1: A laser base plate which was improved from [22] by removing 8x15x2 mm<sup>3</sup> volume for convenience of a horizontal knob adjusting. The upper side was attached to a kinematic mount and the lower side a TEC and a plate shown in Figure C.2.

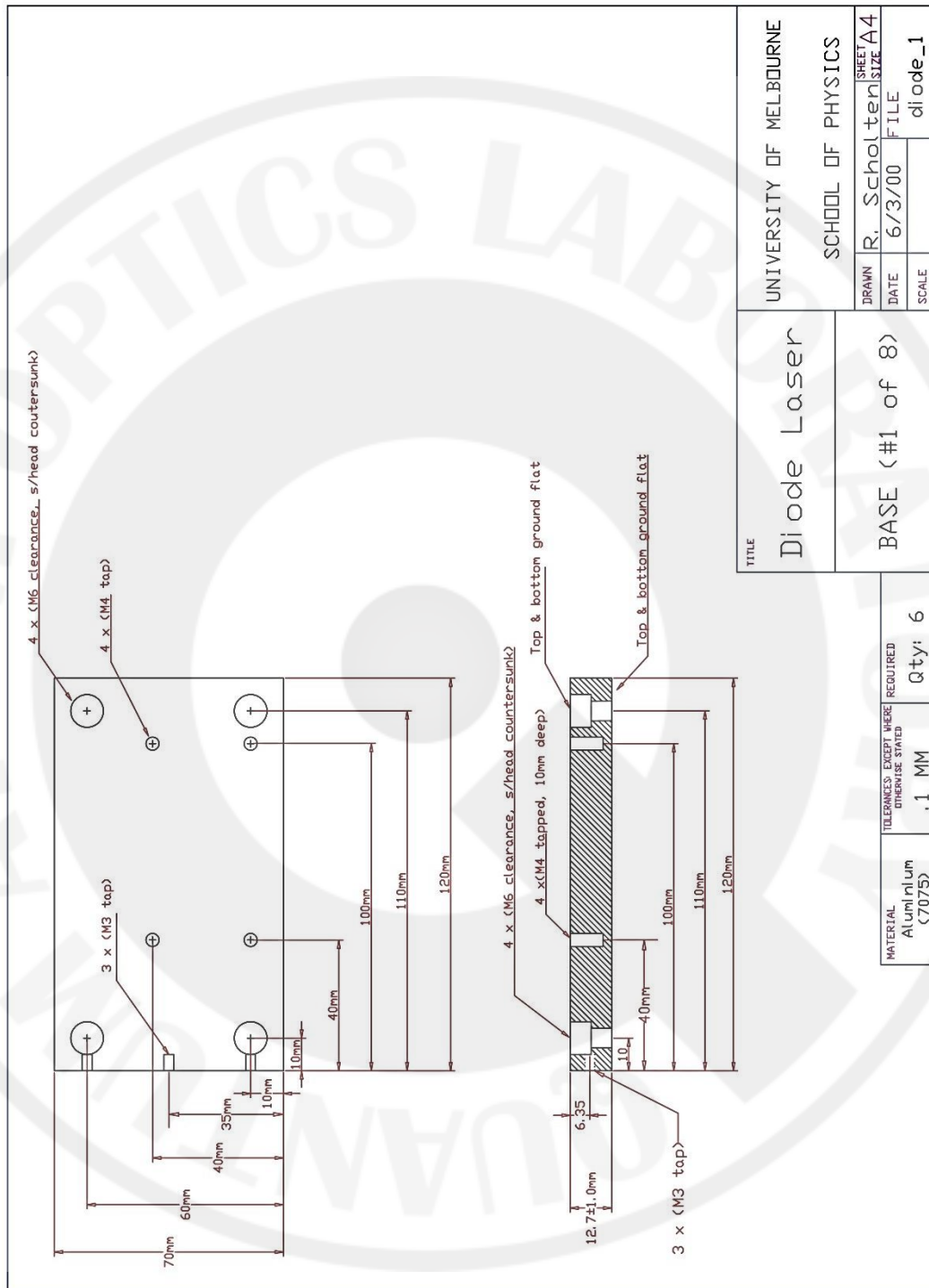


Figure C.2: A laser base plate design from [22]. The upper side was attached to a plate in Figure C.1 via four plastic bolts, with a TEC sandwiched in between both plates. The lower side was attached to an aluminium block in Figure C.3.

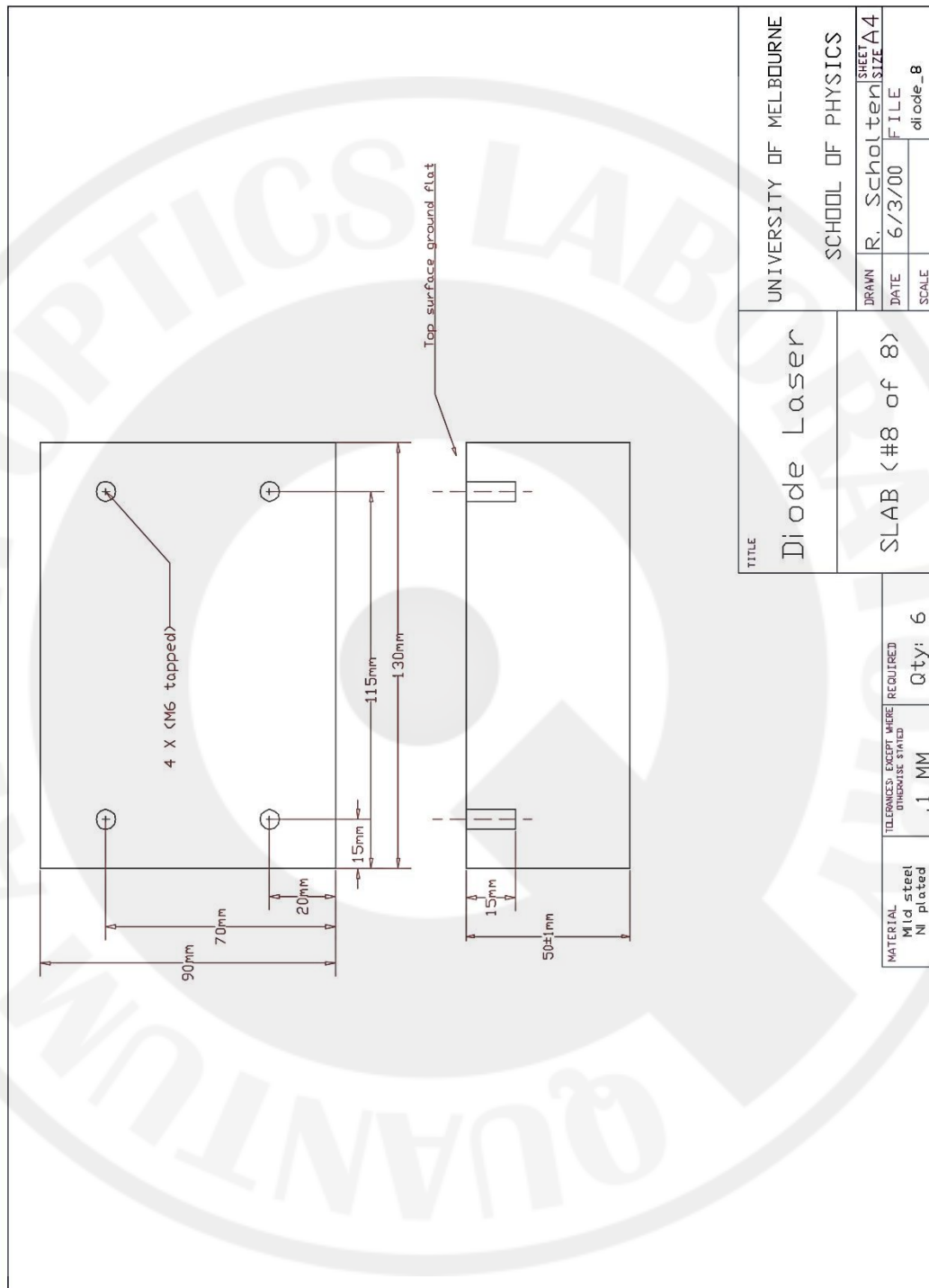


Figure C.3: The aluminium block used as a heat sink for stabilizing the laser temperature. The upper side was attached to the plate in Figure C.2 via four M4 aluminium bolts.

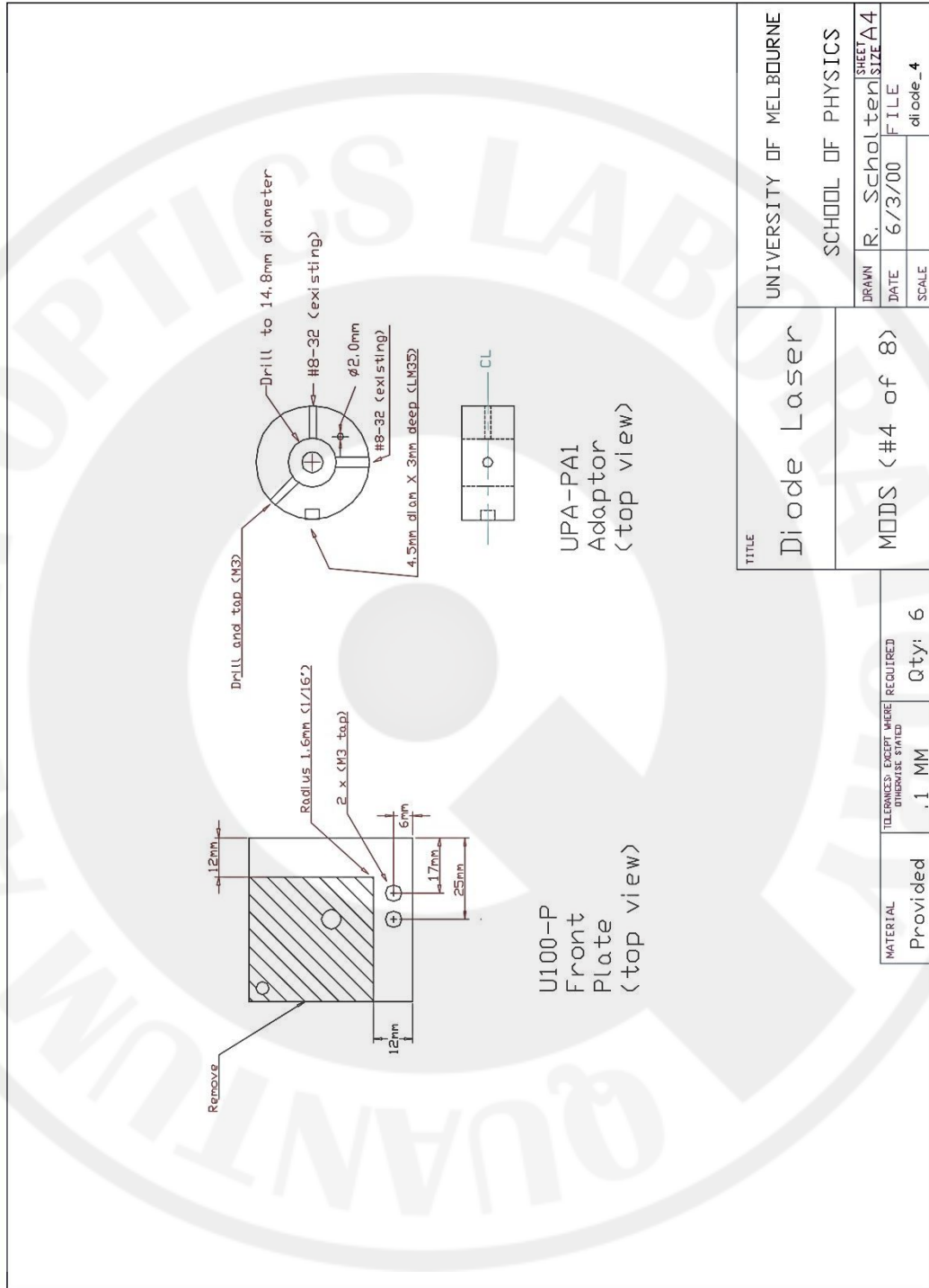


Figure C.4: The kinematic mount (U100-P) and its adapter (UPA-PA1) from Newport modified to mount the collimation tube. This mount was attached to the laser base in Figure C.1 using an M4 bolt.

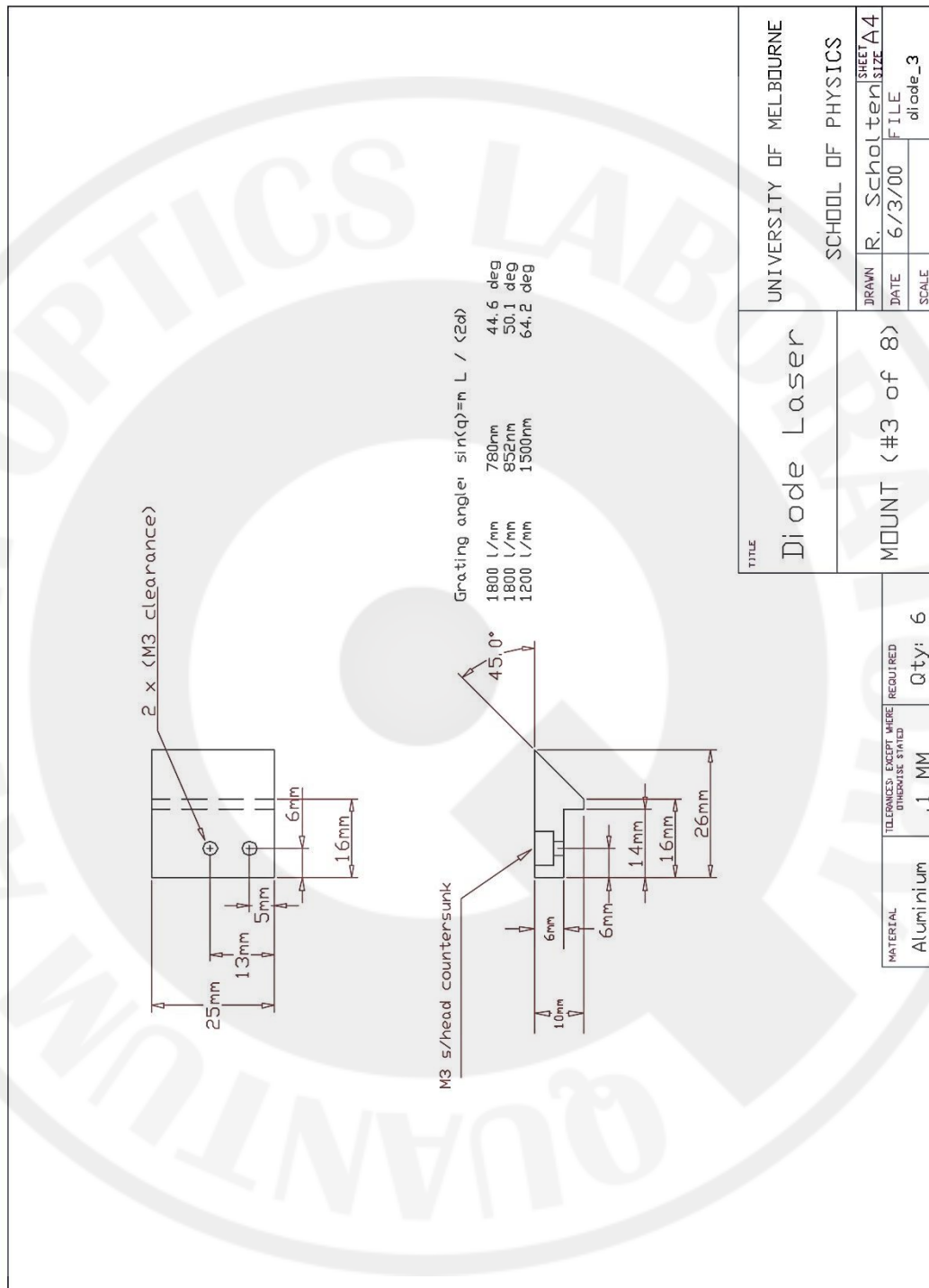


Figure C.5: An aluminium piece with a 45 degree cut. A diffraction grating was attached to the cut side using epoxy. Two M4 bolts joined this aluminium piece to a kinematic mount in Figure C.4.

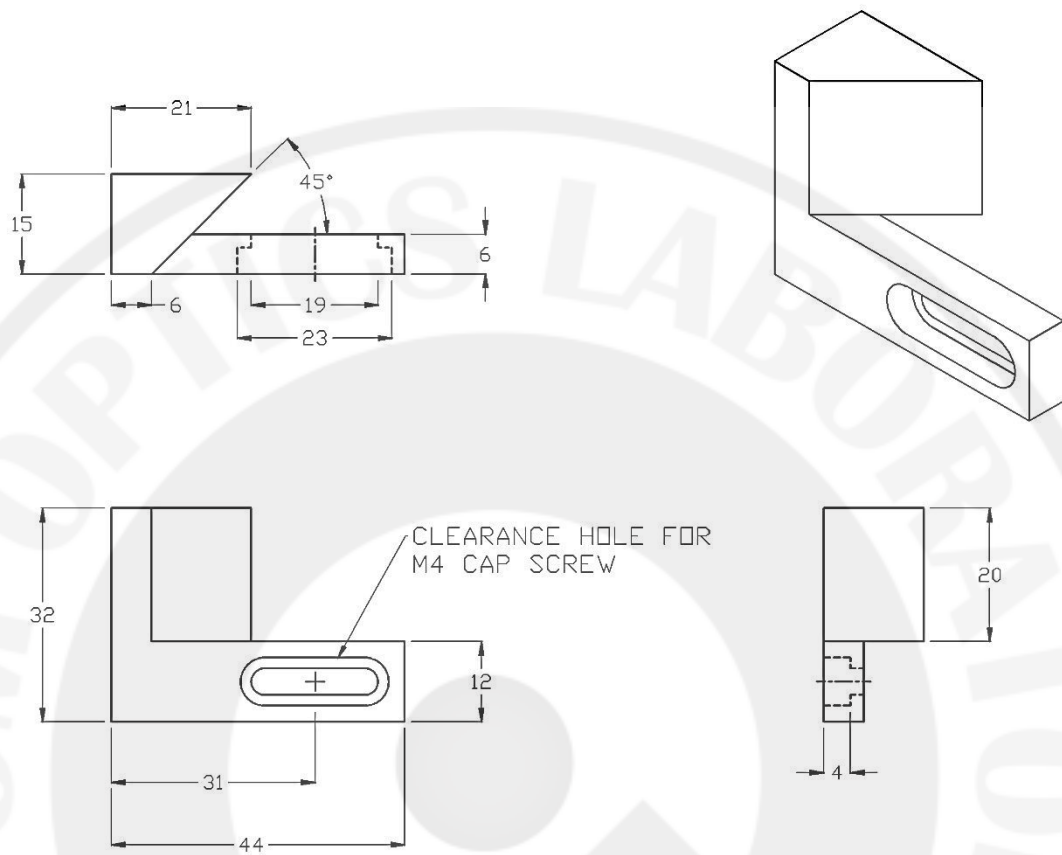


Figure C.6: A mirror mount providing a fix output laser direction. This mount was modified from [16] in order to join with a kinematic mount in Figure C.4.

### C.2 Vacuum Chamber

Mechanical drawings of the vacuum chamber are shown in the figures from Figure C.7 to Figure C.14. These drawings were designed by SLRI.

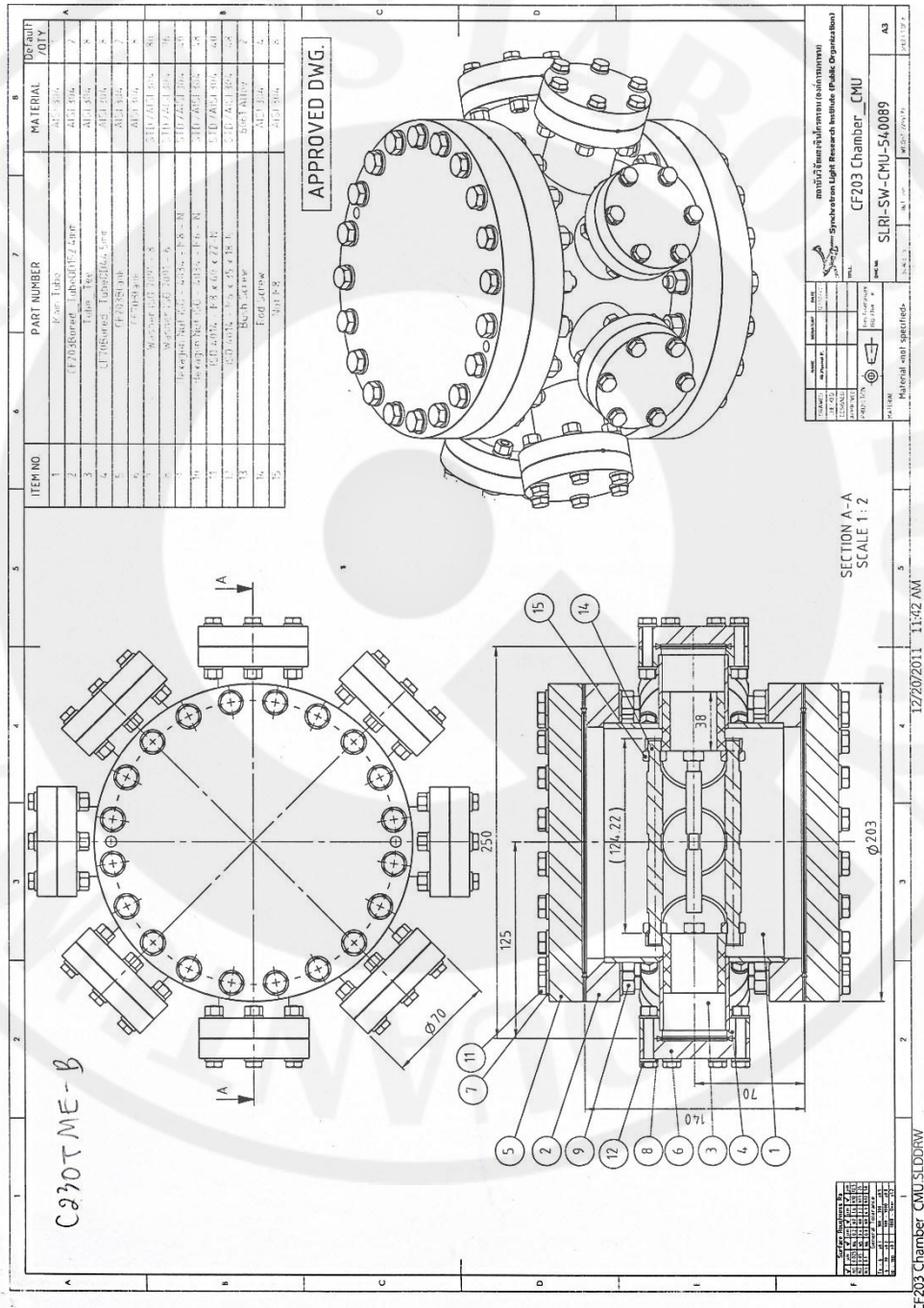


Figure C.7: Chamber outline showing all optical access through eight 2¾" side flanges and two 8" front flanges.

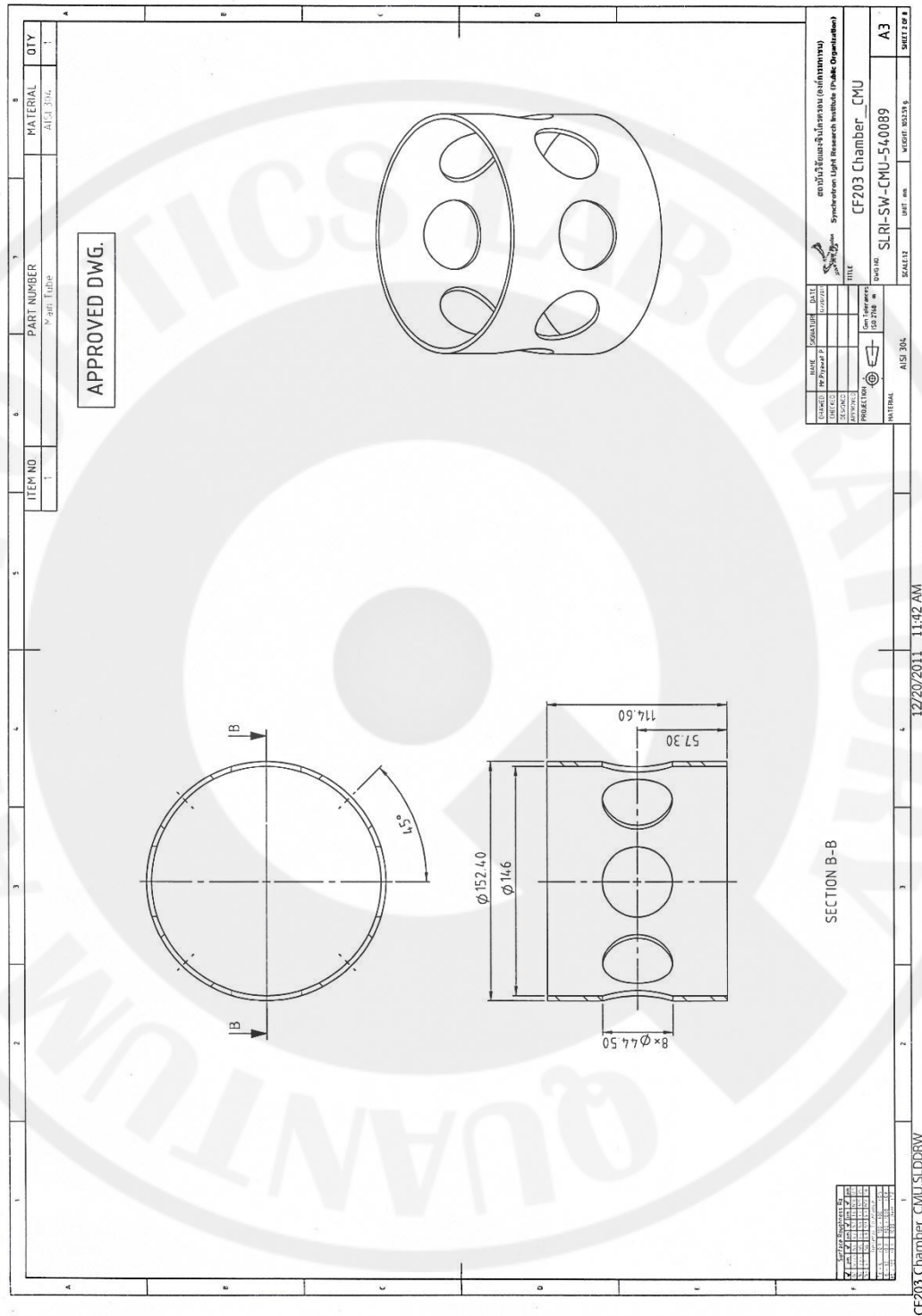


Figure C.8: Chamber body is the main body where all experimental events happen.

The chamber was tested to hold the pressure below  $10^{-8}$  Torr.

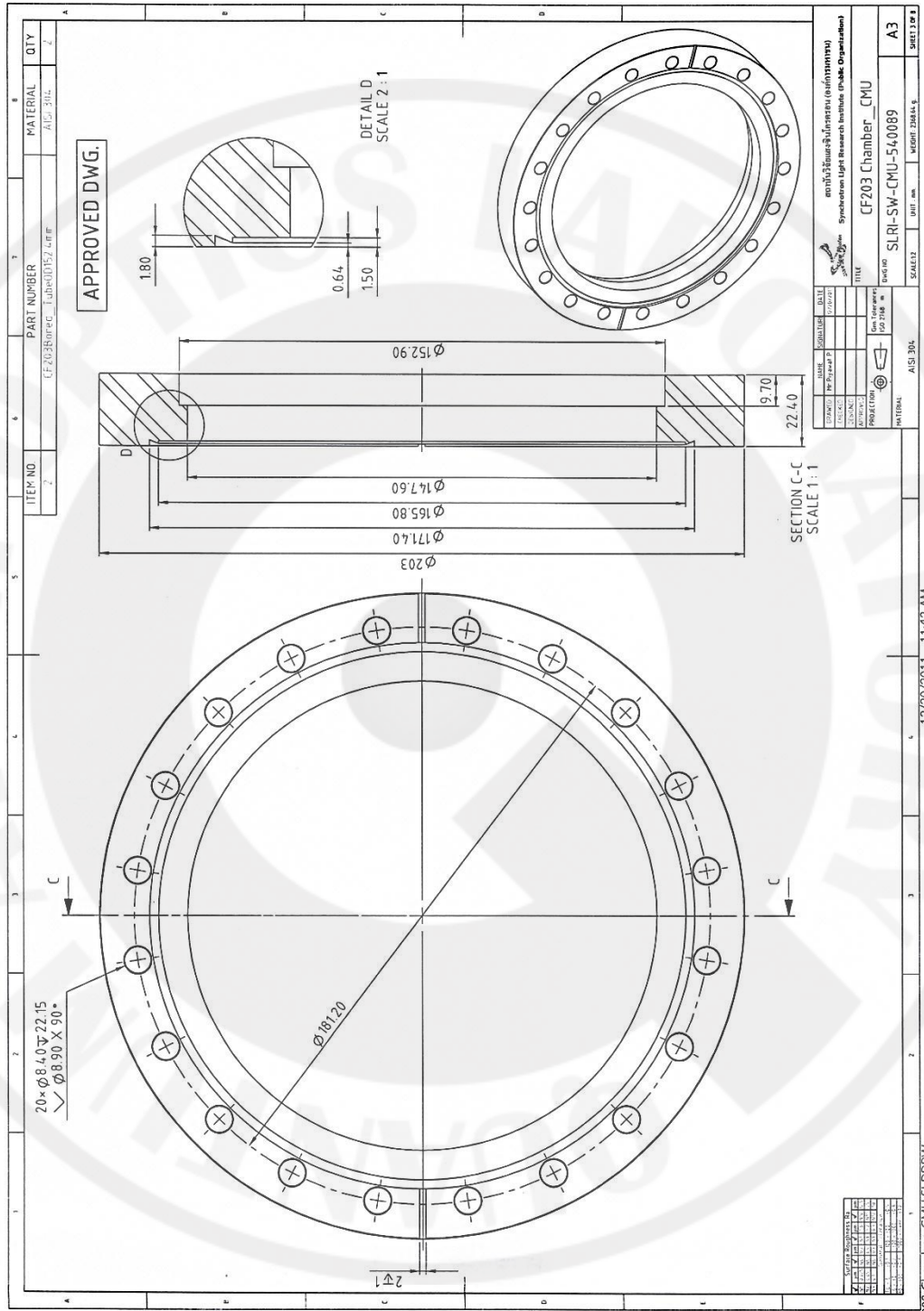


Figure C.9: 8" inner flange.

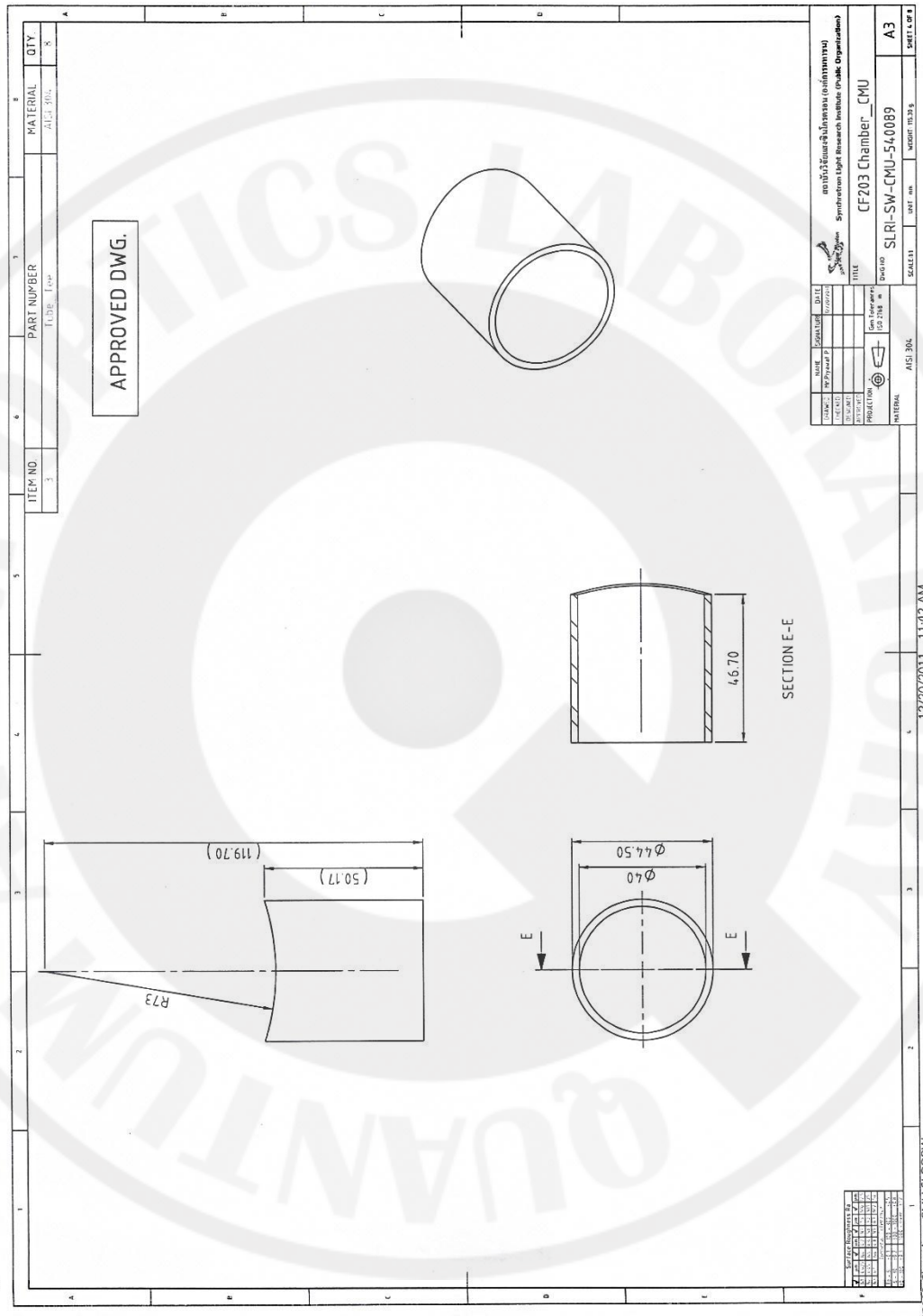


Figure C.10: Tube for 2 3/4 " flange.



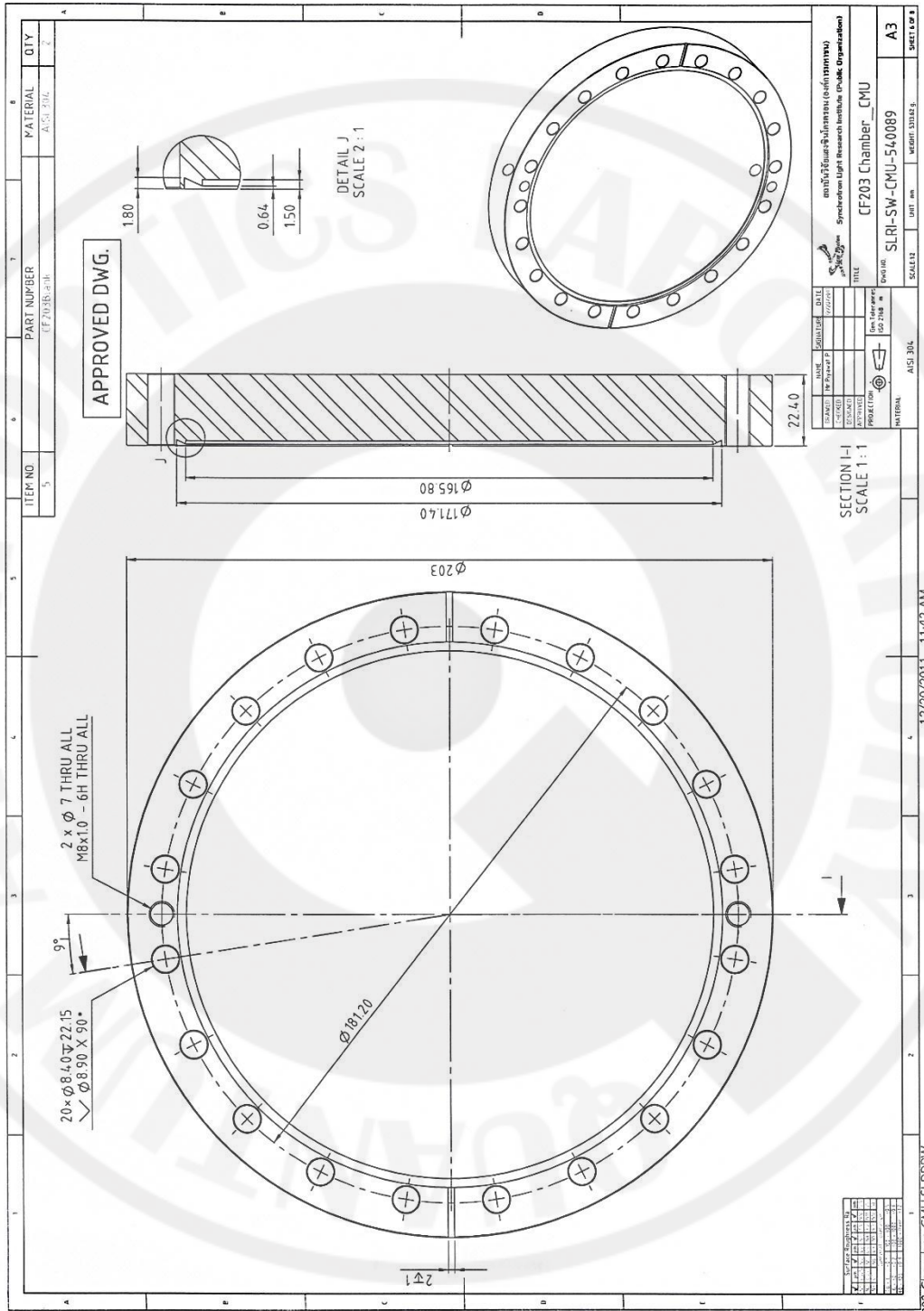


Figure C.12: 8"blank flange.

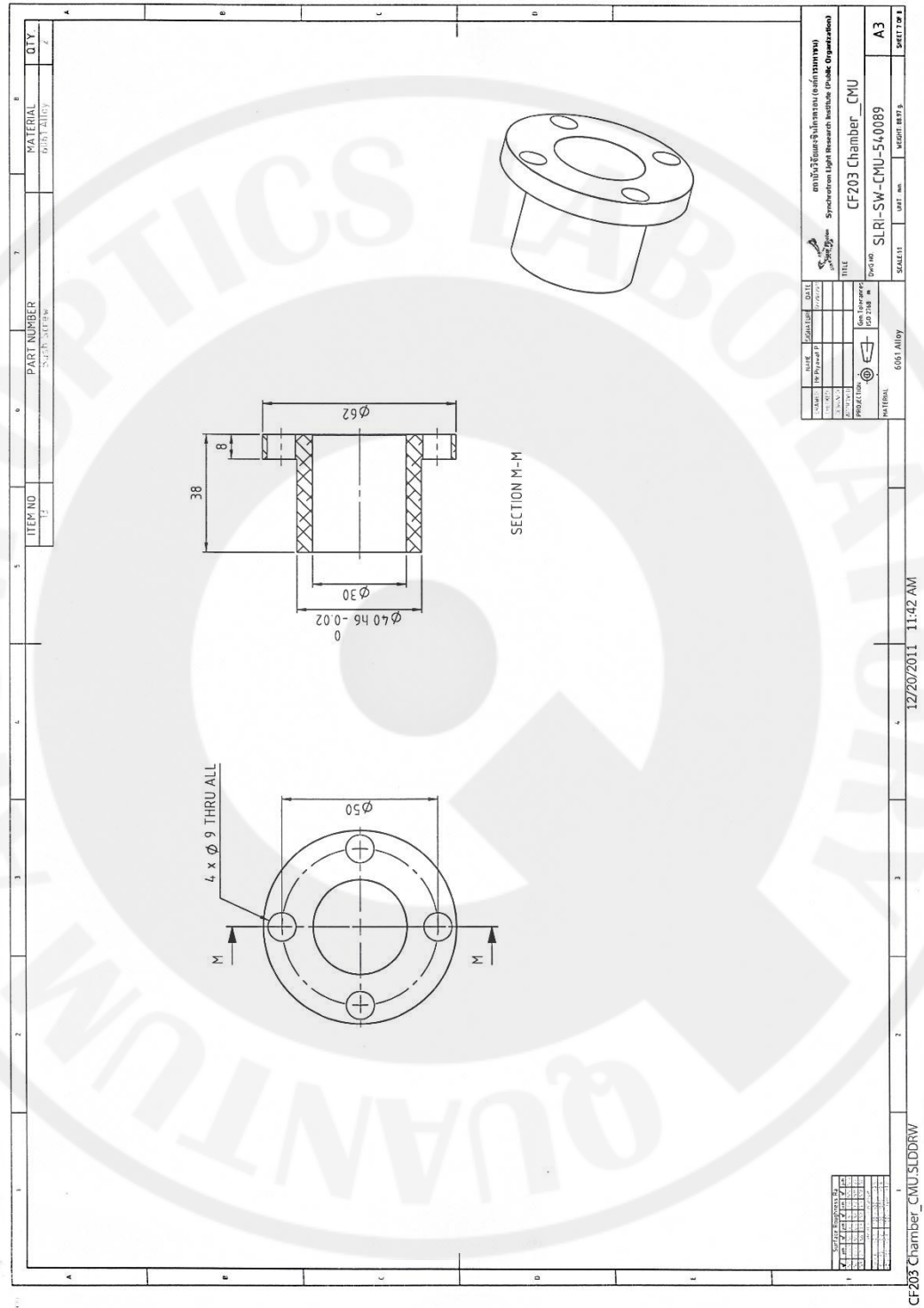


Figure C.13: Straight rods clasper used to fix four straight stainless steel rods (Figure C.14) in place.

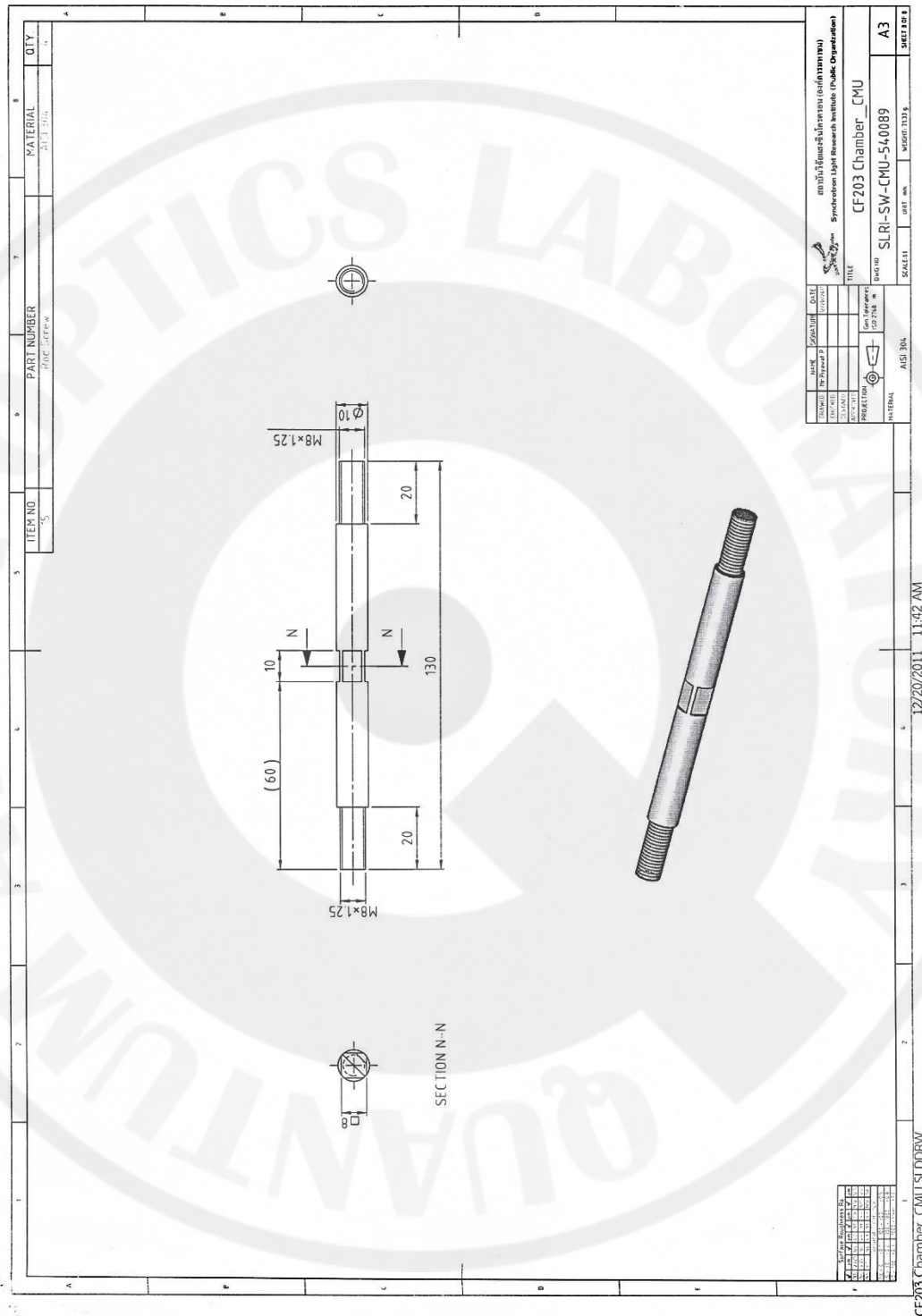


Figure C.14: A straight rod. The rod provides straight edge for positioning and mounting a high NA lens.

### C.3 High NA Lens Mount

The high NA lens used in this research is C240TME-B from Thorlabs. The mechanical drawing of this lens is shown in Figure C.15.

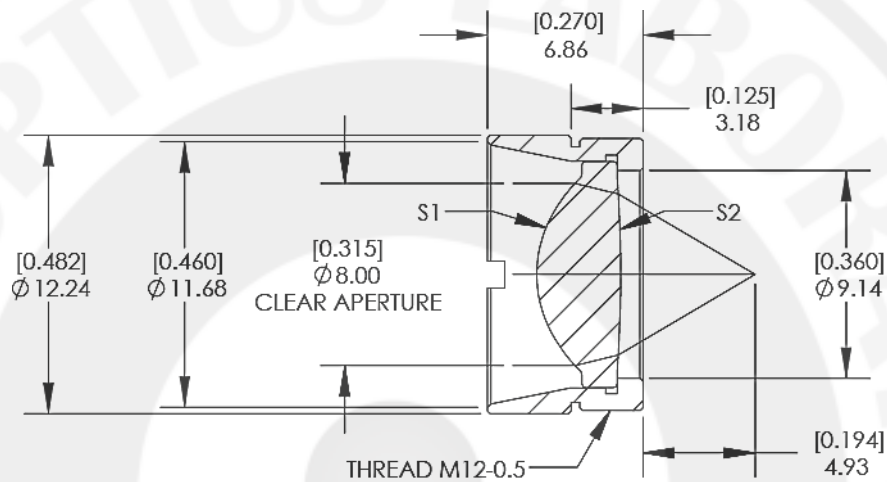


Figure C.15: The High NA lens from Thorlabs. The focal point is located at 4.95mm from the nearest side of a lens mount. This drawing can be obtained from Ref. [23].

This lens was clamped inside the chamber using a homemade high NA lens mount. The criteria for this mount ascertain that: (1) the focal point of this lens be located at the center of the chamber and (2) this mount must not block other laser beams. As a result, the lens mount contained merely two pieces of aluminium as shown in Figure C.16 and Figure C.17.

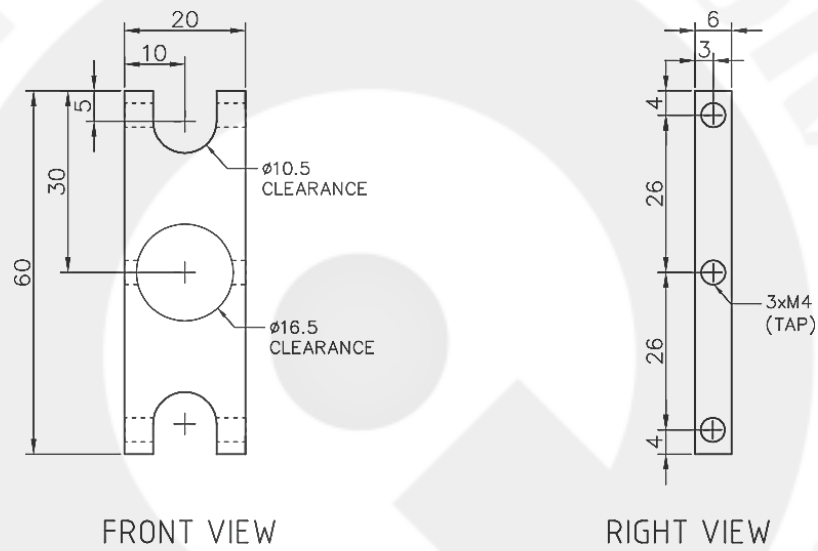


Figure C.16: The mechanical drawing of an aluminium base. The center hole was designed to hold and position an aluminium tube (Figure C.17) and two ends were clamped diagonally with two of the four straight rods (Figure C.14).

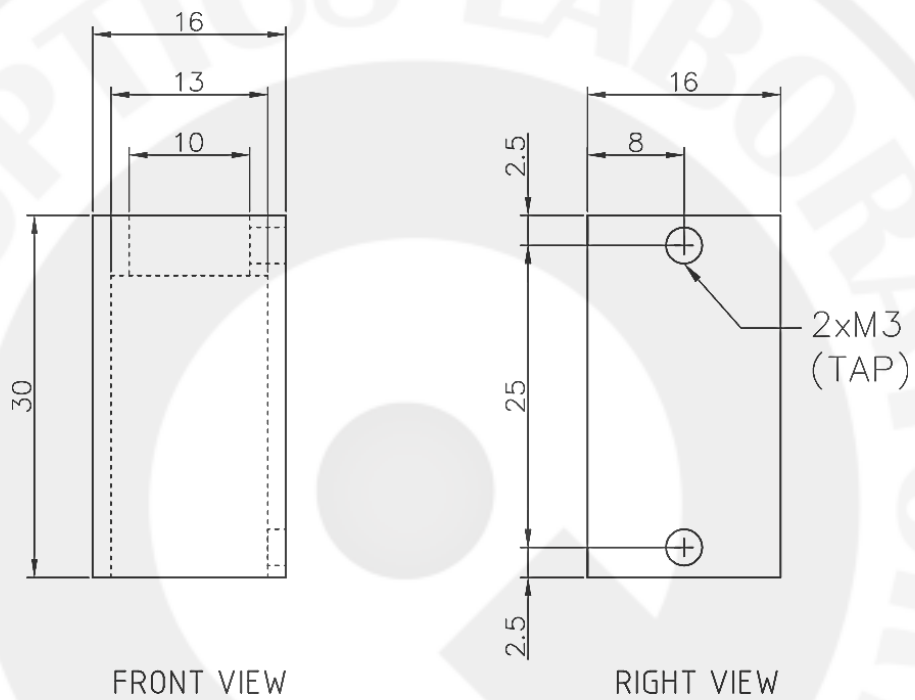


Figure C.17: The mechanical drawing of an aluminium tube for a high NA lens. The lower end was attached to an aluminium piece in Figure C.16. The high NA lens was mounted inside the tube at the top with respect to the alignment in the figure.

### C.4 MOT Lens Mount

Two lenses for the trapping beams are plano-convex lenses (PCX0302) from CASIX. They have the focal length of 50 mm and the diameter of 25.4mm. These lenses were clamped inside the chamber using two homemade lens mounts. Each lens mount contained three pieces of aluminium as shown in Figure C.18, Figure C.19 and Figure C.20.

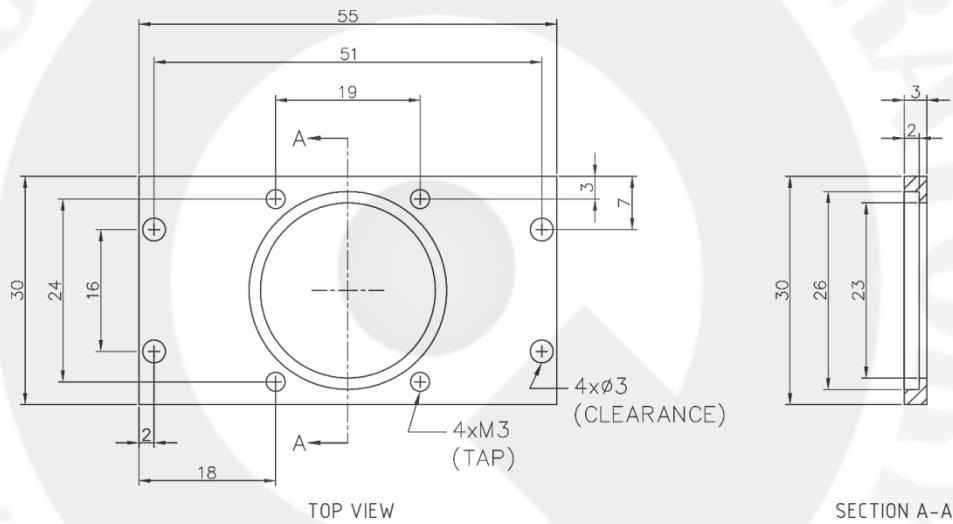


Figure C.18: An aluminium base for mounting the plano-convex lens. The lens was placed at the center of the base.

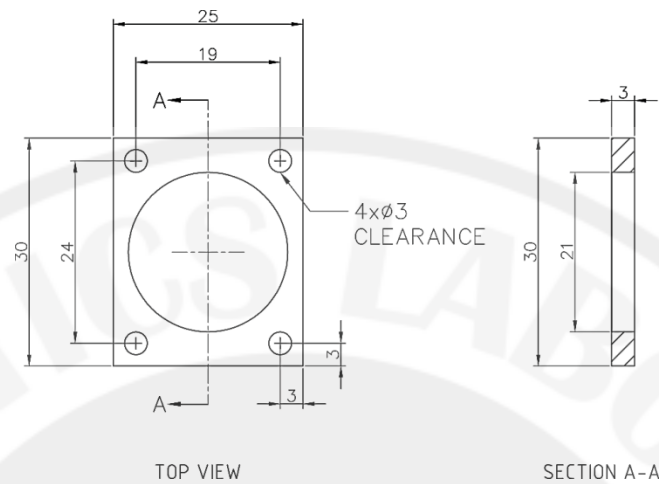


Figure C.19: An aluminium piece for locking lens to the aluminium base.

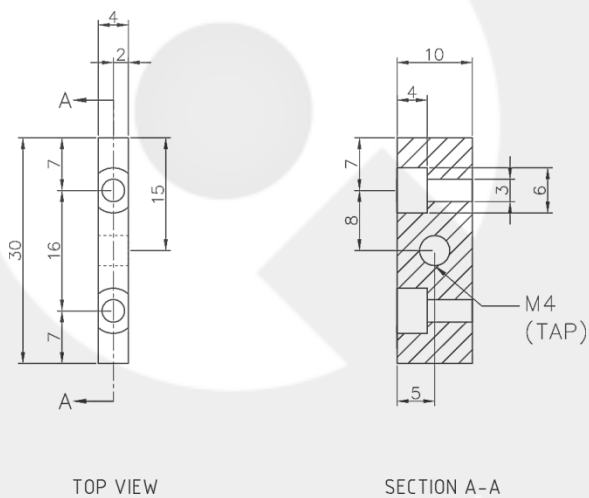


Figure C.20: An aluminium piece for clamping the aluminium base to the straight rods. The clamp exploits an M4 bolt pressing against the rod via a tapped hole in the right panel (side view). It is attached to the side of the base in Figure C.18 using two M4 bolts via two holes shown in the left panel (top view).

## APPENDIX D

### CALCULATION AND PROGRAMMING

#### D.1 Background Subtraction Program (MATLAB)

```
----- Background_Subtraction.m -----  
  
%% Background Subtraction Program  
%  
%% Input Image  
clear all, close all  
pic = imread ('D24-17_MOT.bmp');  
bg = imread ('D24-17_bg.bmp');  
%  
%% Background Subtraction  
sub = pic - bg;  
%  
%% Fast Furier Transform  
sub_f = fft2(sub);  
sub_f = fftshift(sub_f);  
figure(3);  
mesh(double(abs(sub_f)));  
sizef = 10;%  
%  
%% Manual 1'st order subtraction  
sub_f(1:(768/2)-sizef,:) = 0;  
sub_f((768/2)+sizef:768,:) = 0;  
sub_f(:,1:(1024/2)-sizef) = 0;  
sub_f(:,(1024/2)+sizef:1024) = 0;  
%  
%% Inverse FFT  
sub_if = ifft2(sub_f);  
figure(4); %%reduced  
mesh(double(abs(sub_if)));  
%  
%% Show Image  
figure(5);  
imagesc(abs(sub_if));  
xlabel('Pixel number','FontName','Times New Roman','FontSize',16);  
ylabel('Pixel number','FontName','Times New Roman','FontSize',16);  
set(gcf,'color','white');  
set(gca,'fontname','Times New Roman','FontSize',15); % gca=get  
current axes  
set(gca,'XTick',0:200:1000,'YTick',0:100:800); axis([400 600 400  
600]);  
axis equal;  
axis tight;  
%  
----- end -----
```

## D.2 Magnetic Field Gradient (MATLAB)

```

----- scp_magcoil.m -----

%% Magnetic Field Gradient Calculation
%
n = 102 ; % number of turns
nz = 34; % number of turns in the first row
I = 10; % input current in Ampere
%
R0 = 10*1e-2; % coil radius in meter
d0 = 5*1e-2; % half of distance between coils in meter
%
dwire = 2.1*1e-3; % wire diameter + space in meter
%
mu = 4*pi*1e-7; % permeability
%
dR = 0; % additional radius of coils
dd = 0; % additional distance between coils
%
length = 0; % length of coil
%
i = 0; %loop counter
sumgradB = 0;
gradB = 0;
d = d0;
R = R0;
%
while i<n
    j = 0; % first row counter
    dd = 0;
    while j < nz && i<n
        R = R0+dR;
        d = d0+dd;
        gradB=-(3*mu*I*R*R*d)/(R*R+d*d)^2.5;
        sumgradB = sumgradB +gradB;
        i = i+1;
        j = j+1;
        dd = dd+dwire;
        length = length + 2*pi*R;
    end
    dR = dR+dwire;
end
%
sumgradB*1e2 % magnetic field gradient in G/cm
length % length of coil

----- end -----

```

### D.3 Magnetic Field along Z Axis (MATLAB)

```

----- Magnetic_field_gradient.m -----

% Magnetic Field Gradient Calculation
clear all; close all;
%
n = 102 ;
nz = 34;
nR = ceil(n/nz);
%
mu = 4*pi*1e-7;
I = 10;
R0 = 10*1e-2;
d0 = 5*1e-2;
dwire = 2.1*1e-3;
%%
d = linspace(d0,d0 + ((nz-1)*dwire), nz);
R = linspace(R0,R0 + ((nR-1)*dwire), nR);
z = linspace(-0.15,0.15,100);
%
B0 = zeros(1,100);
B = zeros(1,100);
%
nnR=0;
nnd=0;
%
for nnR = 1:nR
    if nnR<nR
        for nnd = 1:nz
            B0=-(mu*I*(R(nnR)^2))/2*(1./(R(nnR).^2
+ (z+d(nnd)).^2).^1.5 - 1./(R(nnR)^2 + (z-d(nnd)).^2).^1.5)*1e4;
            B = B0 + B;
        end
    else
        for nnd = 1:(n-(nR-1)*nz)
            B0=-(mu*I*(R(nnR)^2))/2*(1./(R(nnR)^2
+ (z+d(nnd)).^2).^1.5 - 1./(R(nnR)^2 + (z-d(nnd)).^2).^1.5)*1e4;
            B = B0 + B;
        end
    end
end
%
plot(z*100,B,'r','LineWidth',2);
grid on;
axis([100*[-0.15 0.15] -60 60]);
xlabel('Position (cm)','FontName','Times New Roman','FontSize',16);
ylabel('Magnetic field (Gauss)','FontName','Times New Roman','FontSize',16);
set(gcf,'color','white');
set(gca,'fontname','Times New Roman','FontSize',15);
%
----- end -----

```

#### D.4 Approximate Magnetic Field Line (MATHEMATICA)

This program was modified from Ref. [24].

```
----- Anti-Helmholtz Coils.nb -----

(*Anti - HelmholtzCoils*)
n = 102; (*Number of turns*)
k = 15; (*Current*)
R = 105 × 10-3; (*Radius of coil (mm)*)
d = 100 × 10-3; (*half of distance between coils (mm)*)
ContourPlot[ $\frac{nk\pi R^2 \text{Abs}[x]}{(R^2 + x^2 + (z - d)^2)^{3/2}} \left(1 + \frac{15R^2 x^2}{8(R^2 + x^2 + (z - d)^2)^2}\right) - \frac{nk\pi R^2 \text{Abs}[x]}{(R^2 + x^2 + (z + d)^2)^{3/2}}$ 
×  $\left(1 + \frac{15R^2 x^2}{8(R^2 + x^2 + (z + d)^2)^2}\right)$ , {z, -13 × 10-2, 13 × 10-2}, {x, -13 × 10-2, 13 × 10-2}
, ContourShading → None, AxesLabel → {x, z}, ContourStyle → Thick]

----- end -----
```

**CURRICULUM VITAE**

<b>Name</b>	Ms. Nithiwadee Thaicharoen
<b>Date of Birth</b>	December 26 <sup>th</sup> , 1987
<b>Education</b>	
2006-2010	B.S. (Physics), First Class Honor with Gold Medal Prize Department of Physics and Materials Science Faculty of Science, Chiang Mai University, Thailand Cumulative GPA 3.98/4.00
2003-2006	The Prince Royal's College, Chiang Mai, Thailand Cumulative GPA 3.98/4.00
<b>Scholarship</b>	
2006-2012	Development and Promotion of Science and Technology Talent Project (DPST) of the Institute for the Promotion of Teaching Science and Technology (IPST), Ministry of Science and Technology
<b>Research Grant</b>	
2005-2012	Junior Science Talent Projects (JSTP) of the National Science and Technology Development Agency (NSTDA)

## Experience

- 2010-2012 Quantum Atom Optics Laboratory, Chiang Mai University, Thailand
- 2011 School and Workshop on New Trends in Quantum Dynamics and Entanglement, International Centre for Theoretical Physics (ICTP), Trieste, Italy
- 2010 The 60th Nobel Laureate Meetings at Lindau, Germany
- Candidate of Thailand for the Nobel Laureate Meetings in interdisciplinary fields (physiology or medicine, physics and chemistry) at Lindau, Germany

## Presentation

- 2012 “The First Magneto-optical Trap in Thailand and Beyond”  
The First ASEAN plus Three Graduate Research Congress (AGRC), Chiang Mai, Thailand
- 2012 "Light Assisted Collisions of Cold Rubidium-85 Atoms in an Optical Dipole Trap"  
Siam Physics Congress 2012 (SPC2012), Phra nakhon Si Ayutthaya, Thailand
- 2012 "Loading of 85-Rubidium Atoms in an Optical Dipole Trap"  
The 7th Conference on Science and Technology for Youths, Bangkok, Thailand